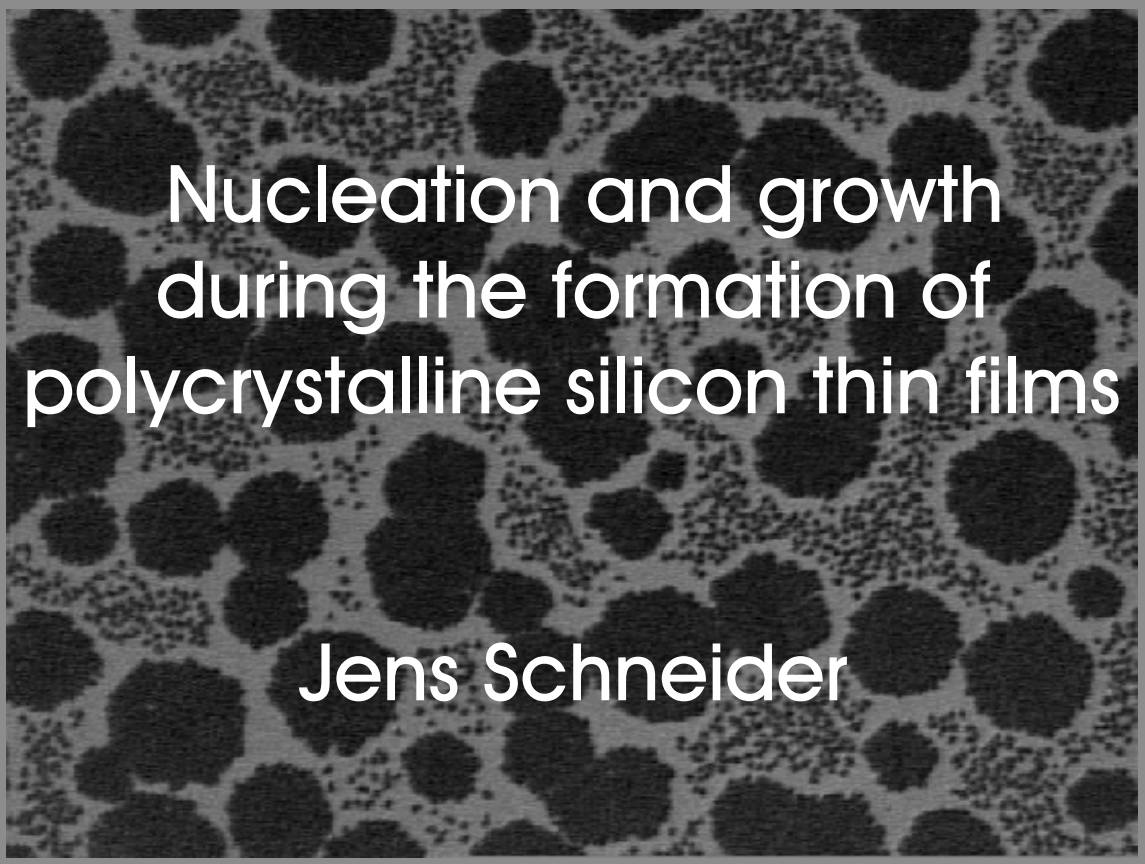

# Nucleation and growth during the formation of polycrystalline silicon thin films

Jens Schneider

# Nucleation and growth during the formation of polycrystalline silicon thin films

vorgelegt von
Diplom-Ingenieur
Jens Michael Schneider
aus Calw

von der Fakultät IV - Elektrotechnik und Informatik
der Technischen Universität Berlin
zur Erlangung des akademischen Grades

Doktor der Ingenieurwissenschaften
- Dr. ing. -

genehmigte Dissertation

Promotionsausschuss:

| | |
|---|---|
| Vorsitzender: | Prof. Dr. H. Reichl |
| Gutachter: | Prof. Dr. C. Boit |
| Gutachter: | Prof. Dr. W. Fuhs |

Tag der wissenschaftlichen Aussprache: 30. August 2005

Berlin 2006
D 83

"Our ignorance is not so vast as our failure to use what we know."

Marion King Hubbert

# Abstract

Polycrystalline Silicon (poly-Si) thin films on foreign substrates are interesting for large area electronic devices like displays, sensors and solar cells. Such films can be formed by the aluminum-induced layer exchange (ALILE) process. In the ALILE process aluminum, amorphous silicon (a-Si) bi-layers exchange their positions with a concurrent crystallization of the silicon during a simple annealing step below the eutectic temperature of the Al/Si system ($T_{eu} = 577\,°\text{C}$). The resulting poly-Si layer is large grained which promises high carrier mobilities and exhibits a preferential, crystallographic $(100)$ orientation which facilitates low-temperature, epitaxial thickening.

Within this thesis glass/Al/a-Si layer stacks are investigated in-situ during the ALILE process with an optical microscope. The role of a thin interlayer between the Al and a-Si is studied. While nucleation in isothermal annealing experiments is caused by supersaturation of silicon in the aluminum layer additional nucleation can be enforced by supercooling the sample during annealing. The use of temperature profiles during annealing reveals the mechanism of the ALILE process.

The process is discussed on the basis of thermodynamic consideration and elucidated within the Al/Si phase diagram. The definition of Si concentration limits in the Al demonstrates that the large grains in the resulting poly-Si film are caused by a characteristic self-limiting suppression of nucleation during the layer exchange process. When the Si concentration is above the saturation concentration but below a critical concentration existing grains grow but additional nucleation is suppressed. From the thermodynamic considerations on nucleation and growth a model is derived explaining the origin of the preferential orientation.

Both experimental and theoretical results obtained in this thesis allow to develop recipes for an optimized polycrystalline silicon layer formation. Poly-crystalline silicon thin-film solar cells based on the seed layer concept have the potential to achieve high efficiencies at very low costs which make them suitable candidates for the medium-term future solar cell technology.

# Zusammenfassung

Dünne Schichten aus polykristalline Silizium auf Fremdsubstraten sind für großflächige, elektronische Anwendungen wie Displays, Sensoren und Solarmodulen von starkem Interesse. Im aluminium-induzierten Schichtaustauschprozess wird ein Glas/ Aluminium/ amorphes-Silizium Schichtstapel durch einen einfachen Temperschritt in einen Glas/ polykristallines Silizium/ Aluminum(+Silizium) Schichtstapel überführt. Damit können polykristalline Siliziumschichten mit kristallinen Wachstumsbereichen von bis zu $100\,\mu\mathrm{m}$ Durchmesser hergestellt werden. Die großen Wachstumsbereiche werden durch eine selbstlimitierende Nukleation erreicht. Die Schichten zeichnen sich durch eine $(100)$ Vorzugsorientierung aus. Diese Vorzugsorientierung macht die poly-Si Schichten besonders interessant für epitaktische Verdickung bei niedrigen Temperaturen.

Mittels optischer Mikroskopie wurde der aluminium-induzierte Schichtaustauschprozess in-situ untersucht. Dabei wurden neben dem Einfluss der Tempertemperatur auch der Einflusss einer dünnen Schicht zwischen der ursprünglichen Aluminium- und amorphen Silizium-Schicht untersucht. Die Proben wurden durch DC Magnetron Sputtern hergestellt. Als Zwischenschicht wurde Aluminiumoxid verwendet. Die Oxidschicht wurde durch natürliche und thermische Oxidation hergestellt. Alternativ wurde per Sputterdeposition auch eine Molybdenschicht als Zwischenschicht untersucht. Zur Strukturuntersuchung der resultierenden Schichten wurden Transmission Electron Microscopy (TEM) und Electron Backscatter Diffraction (EBSD) eingestzt.

Im aluminium-induzierten Schichtaustauschprozess haben die verschiedenen Prozessparameter meist sowohl positive als auch negative Einflüsse. Hohe Tempertemperaturen reduzieren die Prozesszeit. Wohingegen niedrige Temperaturen die Korngröße erhöhen und der Anteil der $(100)$-Vorzugsorientierung vergrößern. Dicke Oxidzwischenschichten führen zu großen Körner. Dünne Oxidschichten hingegen bewirken kurze Prozesszeiten und erhöhen den Anteil der $(100)$-Vorzugsorientierung. Um möglichst viele positive Eigenschaften in dem Prozess zu vereinen,

wurde die Temperatur während des Prozesses geändert. Die Tempertemperatur kann erhöht werden wenn die Nukleations unterdrückt ist ohne das neue Körner entstehen. Dadurch kann die Prozesszeit verkürzt werden, ohne die Korngröße zu verringern.

Die Nukleation im aluminium-induzierten Schichtaustauschprozess wird bei isothermischer Temperung durch Übersättigung des Aluminiums mit Silizium hervorgerufen. Durch Abkühlen während der Temperung kann zusätzlich Nukleation durch Unterkühlung erzwungen werden, auch wenn die Nukleation bereits unterdrückt ist. Gebiete ohne neue Nukleation um die bestehenden Körner werden dabei sichtbar. Dies ist ein direkter Nachweis des Modells bei dem die Nukleationsunterdrückung durch Silizium-Verarmungszonen im Aluminium hervorgerufen wird.

Im Aluminium-Silizium-Phasendiagramm werden die Ergebnisse vor einem Thermodynamischen Hintergrund diskutiert. Die Definition dreier wichtiger Si Konzentrationen im Aluminium gestattet es, den Mechanismus der selbstlimitierten Nukleationsunterdrückung zu verstehen. Sowohl die Nukleations- als auch die Wachstumsrate werden von der Si Konzentration bestimmt. Unterhalb eines kritischen Werts ist die Nukleation unterdrückt, aber die bestehenden Körner wachsen weiter.

Thermodynamische Überlegungen zeigen, dass die $(100)$-Vorzugsorientierung bereits durch bevorzugte Nukleation hervorgerufen wird. Detailierte Berechnung zur bevorzugten Nukleation von Clustern an der Aluminium-Zwischenschicht-Grenzfläche können sowohl die Temperatur- als auch die Zwischenschichtabhängigkeit der $(100)$-Vorzugsorientierung erklären.

Um optimierte polykristalline Siliziumschichten herzustellen, sollten:

- dünne, natürliche Oxidschichten verwendet werden, die den Anteil der $(100)$-Vorzugsorientierung erhöhen.
- niedrige Anfangstemperaturen gewählt werden, die große Körner erzeugen und ebenfalls den Anteil der $(100)$-Vorzugsorientierung vergrössern.

- Temperatureprofile mit hoher Endtemperatur gewählt werden, die die Prozesszeit minimieren, ohne dabei die Orientierung zu ändern oder neue Keime zu erzeugen.

Mit diesem Verfahren können optimale polykristallinen Silizium Schichten mit dem aluminium-induzierten Schichtaustauschprozess hergestellt werden, die gut für nachfolgende epitaktische Verdickung geeignet sind. Polykristalline Siliziumdünnschichtsolarzellen, die mit diesem Konzept hergestellt werden versprechen hohe Wirkungsgrade bei niedrigen Kosten und sind somit Kandidaten für eine neue Solarzellengeneration der mittelfristigen Zukunft.

# Contents

# 1 Introduction

'Solar power is hot', is the conclusion of equity investment analysts from Credit Lyonnais Securities Asia (CLSA) in July 2004 [1]. In this report CLSA advises its clients to 'become familiar with' and 'keep a watch for' an upcoming market with total revenues predicted to rise from $7\,bn\,\mathrm{US\$}$ in 2004 to $30\,bn\,\mathrm{US\$}$ in 2010. A growth rate of above $30\,\%$ is expected up to and beyond this point. The key challenge in photovoltaic (PV) is the reduction of the price per kWh solar generated energy. Price reduction can be achieved by either introducing new technologies or increasing production. Learning curves indicate that doubling the cumulative production of PV modules leads to a price reduction by $20\,\%$. Following this learning curve together with the assumption of a continuous growth rate of $30\,\%$ in the upcoming years (the growth rate in 2004 has been $67\,\%$ [2]) and a price of $7\,\mathrm{US\$/\,W_p}$ in 2004, the psychologically important margin of $1\,\mathrm{US\$/\,W_p}$ will be reached before 2030 at a cumulative production of about $400\,G\mathrm{W_p}$ with total revenues of $400\,bn\,\mathrm{US\$}$. While the electricity production cost for current PV systems in Germany is about $50\,\mathrm{Ct./kWh}$, decreasing the module cost to $1\,\mathrm{US\$/\,W_p}$ will get PV within the margin of economical competitiveness with conventional energy sources. At this point PV will contribute a large share to world's energy supply. Reaching this goal depends highly on the possibility to adhere to the learning curve without reaching cost limits which restrict further cost reduction. Therefore solar power is one of the most interesting technologies for the 21st century for both investors and researchers.

Today's PV market is dominated by solar cells based on mono- and polycrystalline silicon wafers. The corresponding process technologies have been developed together with the microelectronics industry. However an essential difference between solar cells and microelectronics lies in scalability. While transistors get cheaper and faster when getting smaller, solar cells cannot decrease in size because large areas are required in order to harvest the sunlight. Increasing the

number of devices per area has no positive effect in photovoltaics. Instead the efficiency of the device has to be increased which is naturally attempted in all solar cell concepts but is limited to $30\,\%$ for an energy gap of $1.1\,\mathrm{eV}$ as pointed out by W. Shockley and H.J. Queisser [3]. M. Green summarized ideas on how to overcome this theoretical limit with so called *third generation solar cells* [4]. The more promising approach on a short to medium term for solar cells to reduce material consumption is the reduction of the thickness of the cells. Thin film concepts are considered *second generation photovoltaics* [5]. The thickness of the wafer based cells is limited by the mechanical stability during wafer handling. Transferring the mechanical stability issue to inexpensive substrates like glass enables the use of much thinner films. Besides PV applications thin films are also attractive for large-area electronic devices like displays and sensors. The homogeneous deposition of thin films on glass substrates on very large scale has already been developed by the glass industry for various applications like mirrors, toned glass etc. Thin film deposition using these technologies permits to save material cost. Additionally, in wafer based modules the solar cells have to be interconnected with extra connection strips. Assembly of connection strips is labor-intensive and sensitive to failure. The advantage of large-area devices on foreign substrates like glass is that interconnections can be realized by monolithic integration of solar cells. This leads to totally new concepts for solar module design offering a high potential to reduce cost limits in PV.

One main challenge when using inexpensive substrates like glass is the limitation in process temperatures. Typical glasses have strain points at about $600\,°\mathrm{C}$. That means all process steps must be below this margin. Si wafers can be handled at much higher temperatures because of the high melting point of Si at $1414\,°\mathrm{C}$. In order to realize thin film technologies at low temperatures different material systems have been investigated. Compound semiconductors like copper indium diselenide (CIS) and cadmium telluride (CdTe) are promising candidates. Silicon is particularly attractive due to its abundance and non-toxicity. Hydrogenated amorphous silicon (a-Si:H) thin films deposited by plasma enhanced chemical va-

por deposition (PECVD) achieved partial success. At present it is the only thin film technology which has overcome the barrier to mass production. But it has not been able to replace wafer based technologies so far and has market share below $10\,\%$. For low-power applications (e.g. watches and calculators) amorphous silicon solar cells are established as dominant technology. They suffer from lower efficiencies due to their poorer electronic properties compared to crystalline wafer material and degradation know as Staebler-Wronski-effect [6]. Consequently the fabrication of silicon thin-films with improved electronic properties has attracted researchers interest. Microcrystalline silicon ($\mu$c-Si-H) can be deposited at temperatures below $200\,$°C. Solar cell efficiencies of above $10\,\%$ are obtained [7]. On $\mu$c-Si:H/a-Si:H tandem solar cell modules of sizes up to $450 \times 910\,\mathrm{mm}^{-2}$ remarkable initial efficiencies of $13.5\,\%$ were obtained recently [7]. Even though these results are quite impressive it is believed that fine-crystalline silicon structures are limited in their perspertive compared to poly-crystalline Si wafer material. In order to minimize recombination at grain boundaries a large grain size is desirable. Ideally a large grained silicon thin film should be formed on a foreign inexpensive substrate, like glass. Large grained can be defined as laterally larger than the layer thickness. In this case the efficiency is limited by the recombination at the front and back contacts. This is hoped to yield efficiencies comparable with silicon wafers at much lower cost. Due to the softening point of glasses at around $600\,$°C the silicon thin films have to be formed at low temperatures.

Due to the high melting point of silicon, crystallization of amorphous silicon at temperatures below the glass softening point is a solid phase reaction. Solid phase crystallization (SPC) has been extensively studied [8] and is addressed in detail in the chapter 'State of the art'. It was found that metals in contact with amorphous silicon reduce crystallization time and temperature. Also, the resulting Si grain size can be increased. Unfortunately metal impurities in the resulting crystalline silicon can lead to very high doping levels (e.g. in case of Al). Due to the resulting high recombination rates crystalline silicon from metal induced crystallization (MIC) is not suitable for absorber layers. But due to the large grain sizes such

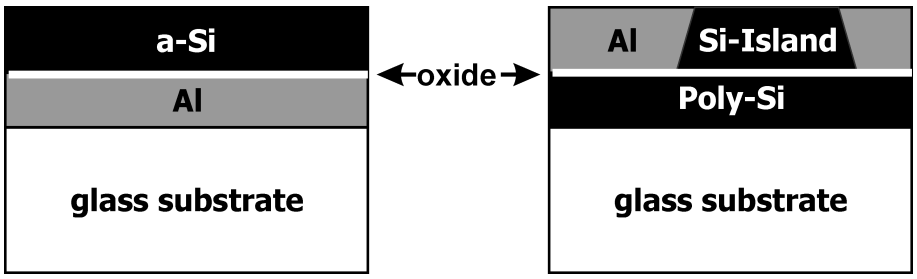


**Figure 1.1:** Schematic ALILE process. The layer stack before (left) and after (right) the layer exchange are shown. The oxide interface layer remains in position during the process.

layers can be used as templates for subsequent epitaxial thickening at low temperatures. To do so a continuous smooth layer of crystallized silicon is needed.

In 1998 O. Nast et al. [9] reported on a process which is now known as aluminum-induced layer exchange process (ALILE). In this process an aluminum and amorphous silicon bi-layer on a glass substrate exchange their position with a concurrent crystallization of the silicon. The resulting polycrystalline silicon layer is smooth, continuous and features large grains ($> 10\,\mu\mathrm{m}$) with a preferential $(100)$ orientation. Thus ALILE layers are eligible as a template (seed layer) for subsequent low temperature epitaxy.

The aluminum-induced layer exchange process (ALILE) is shown schematically in Fig. 1.1. The initial glass/Al/oxide/a-Si layer stack (left side) is transformed into a glass/poly-Si/oxide/Al(+Si) layer stack (right side). The initial a-Si needs to be slightly thicker than the initial Al layer in order to form a continuous poly-Si layer. The Si excess remains in the final Al layer and forms c-Si islands. The interlayer between the initial Al and a-Si layer plays a crucial role in the process. Usually a native Al oxide layer is formed on top of the Al prior to a-Si deposition. This oxide layer remains in position and separates top and bottom layer throughout the layer exchange process.

The ALILE process is the topic of this work. In order to optimize the poly-Si seed layers formed in the ALILE process a profound understanding of the driving forces and mechanisms in the process is required. The role of the initial aluminum amor-

phous silicon interface layer is examined and compared to the influence of the annealing temperature. Limits of the resulting nucleation density and grain size are investigated and the origin of a self-limited nucleation suppression within the ALILE process is elucidated. The influence of the interlayer and the annealing temperature on the resulting orientation of the film is studied. The possibilities of non-isothermal annealing to optimize the process results are tested. The obtained results are discussed against the background of thermodynamics and existing models. A possible explanation for the self-limited suppression of nucleation and the formation of the preferential $(100)$ orientation is suggested. And a route to an optimized poly-Si film made by the ALILE process is proposed.

The thesis is divided into following chapters:

**Chapter 2: 'State of the art'** links this thesis within the context of existing research. An overview is given introducing the history of research on crystallization in general and the background of solid phase crystallization, metal-induced crystallization and the aluminum-induced layer exchange process in particular.

**Chapter 3: 'Experimental'** lists the sample preparation parameters. Oxidation and annealing processes are depicted. The characterization methods are explained including important evaluation methods.

**Chapter 4: 'Results'** shows the influence of the two main parameters under investigation within this thesis. A thin membrane between aluminum and silicon is crucial for the layer exchange process. Here the influence of altering this membrane is investigated. Naturally, the annealing temperature determines the process characteristics strongly. Non isothermal annealing is investigated for improving the process and revealing the mechanism behind the layer exchange.

**Chapter 5: 'Discussion'** elucidates the findings of chapter 4. The parameters influence on nucleation and growth of the Si grains is discussed. A model is suggested which explains the origin of the self-limited nucleation suppression and the preferential $(100)$ orientation.

**Chapter 6: 'Conclusion'** summarizes the most important results and closes with

an outlook on future perspectives of the ALILE process.

# 2 State of the art

This chapter gives a general overview on the theoretical and technological background of metal-induced crystallization and aluminum-induced layer exchange process in particular. Based on the kinetics of phase formation, related processes are investigated for more than 200 years. Already in 1724 G. Fahrenheit performed experiments with undercooling water at low temperatures. A summary of the basics of phase formation and transformation was published by M. Volmer in 1939 [10]. In the early 1970s amorphous semiconductors and their recrystallization behavior became of interest in microelectronics due to the amorphization caused by ion implantation in crystalline silicon for doping purposes and silicon on insulator devices. The driving force of a crystallization process is the reduction of the Gibbs energy when the amorphous silicon transforms into crystalline silicon. The theory of the kinetics of phase change is briefly introduced in section 2.1. Experimental and theoretical results from solid phase crystallization (SPC) applicable to the topic of this work are summarized in section 2.2. A descriptions of metal-induced crystallization (MIC) follows in section 2.3. Finally, an overview of research activities on the aluminum-induced layer exchange (ALILE) process in other groups is given in section 2.4. Currently existing models of the ALILE process from other authors are presented, which allow the classification of the models developed within this thesis (chapter 5). An overview of activities involving ALILE seed layers is given in section 2.5.

## 2.1 Kinetics of phase change

In general, the term 'phase change' includes different transformations: firstly the transition between the states of aggregation, e.g. condensation (gas-liquid) or solidification (liquid-solid), secondly changes of composition in multi-component

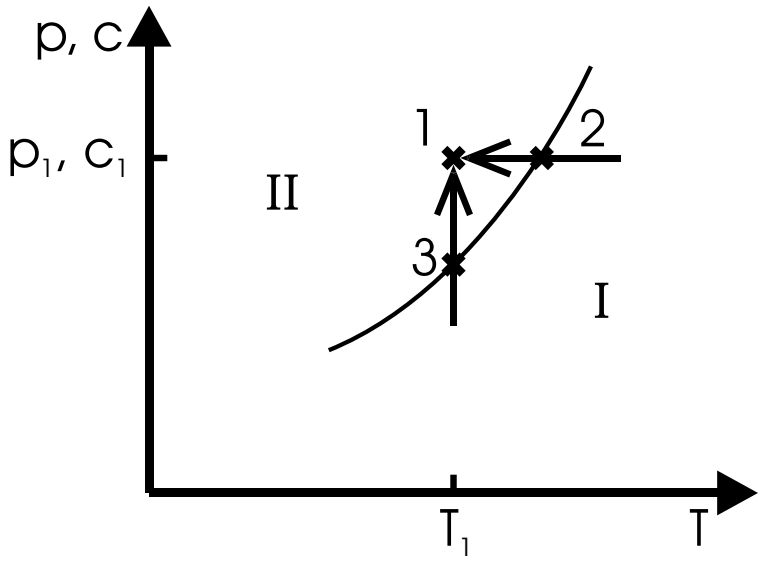


**Figure 2.1:** Phase diagram redrawn from [10]. The line in the p-T diagram (pressure, temperature) gives the coexistence line for phases I and II. In multi-component systems the concentration $c$ is plotted instead of the pressure $p$. Point '1' can be reached by crossing the coexistence line at point '2' by decreasing the temperature at constant pressure $p_1$ (or concentration $c_1$) which is referred to as 'supercooling'. Or by crossing the coexistence line at point '3' by increasing the pressure or concentration at constant temperature $T_1$ which is referred to as 'supersaturation'.

systems, e.g. formation of alloys and thirdly transition between different crystallographic orderings.

Fig. 2.1 illustrates the general principle of phase transformation. Here, the existence of two phases (I and II) in a pressure-temperature diagram (p-T). The straight line denotes the coexistence of the two phases. Along this line both phases are in thermodynamic equilibrium and coexist, e.g. ice floats on water without further freezing or melting. In multi-component systems the concentration $c$ instead of the pressure can be plotted. Upon passing the coexistence line the phase change does not take place immediately but at a certain rate. This rate is determined by the kinetics of phase change. Reaching '1' via '2' , i.e. by decreasing the temperature at constant pressure $p_1$, the process is called *supercooling*; reaching '1' via '3', i.e. by increasing pressure or concentration at constant temperature $T_1$, the pro-

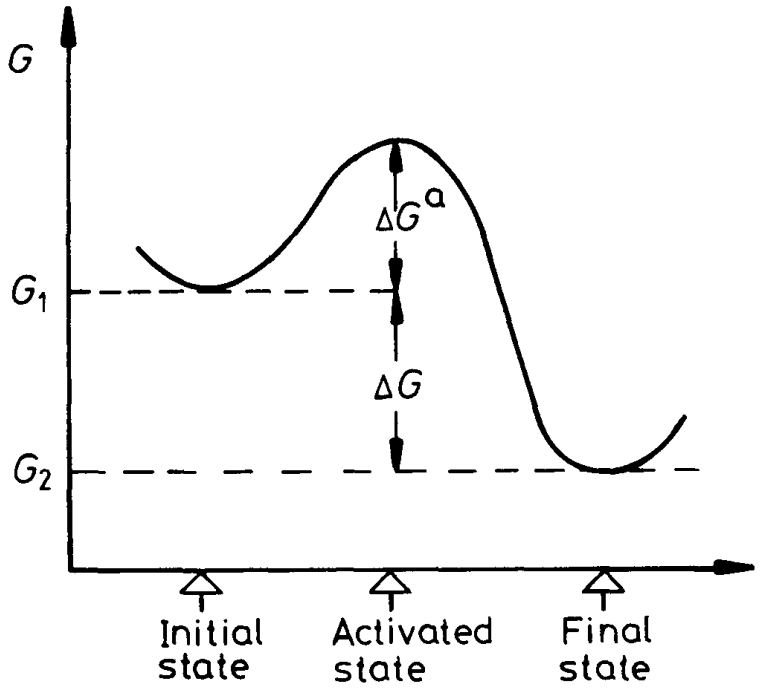


**Figure 2.2:** Gibbs energy $G$ along a reaction path from a metastable, initial state $G_1$ into a stable, final state $G_2$ via an activated state. $\Delta G^a$ is the activation energy and $\Delta G$ is the driving force [11].

cess is called *supersaturation*. The kinetics at point '1' are not affected by the path of reaching '1', i.e. the rate of the phase change will be the same in point '1' wether it was reached by supercooling or supersaturation. Increasing supersaturation or supercooling increases the rate of the phase change.

In general, the thermodynamic driving force for a process is the minimization of the Gibbs energy $G$ of the entire system. Many processes are inhibited by an activation barrier. Such systems need to be supersaturated (or supercooled) in order to overcome the activation energy. In case of the amorphous to crystalline phase transition, the activation barrier is associated with the breaking and rearranging of the covalent bonds of the atoms. In Fig. 2.2 the Gibbs energy $G$ is shown versus a reaction coordinate. The initial state with the Gibbs energy $G_1$ has to pass an activated state with an activation energy $\Delta G^a$ before the final state at the lowest Gibbs energy $G_2 = G_1 - \Delta G$ can be reached. $\Delta G$ is the driving force of the entire process. The process is thermally activated and the rate of transition $j(T)$ from

the metastable, initial state to the stable, final state is given by:

$$j(T) \quad \propto \quad exp\left(-\frac{\Delta G^a}{kT}\right), \tag{2.1}$$

where $k$ is the Boltzmann constant and $T$ the temperature. The activation energy is a barrier for the process which has to be overcome prior to the onset of the phase change.

For the description of the kinetics of phase changes a detailed look on the interface between the participating phases is essential. Forming a new thermodynamically favorable, e.g. a crystalline phase, the Gibbs energy is reduced per atom transferred from phase I (amorphous) to phase II (crystalline). But at the same time an interface between both phases has to be formed. The formation of this interface requires energy and thus increases the Gibbs energy of the system. While the Gibbs energy reduction per atom due to the phase transition is proportional to the number of atoms in the new phase, i.e. the volume, the interface energy is proportional to the surface area of the new phase. The volume is can be expressed as the number of atoms $i$ in the cluster. The number of atoms at the surface must be calculated depending on the shape of the cluster. Spinella et al. used a simple approach with a spherical cluster [12]. The Gibbs energy $\Delta G_i$ for a cluster of size $i$ is the sum of the negative volume term (Gibbs energy reduction) and the positive surface term (Gibbs energy increase) and can be written as:

$$\Delta G_i \quad = \quad -\Delta g_v i + \sigma O_i. \tag{2.2}$$

Here, $\Delta g_v$ is the Gibbs energy reduction per atom and $\sigma$ is the specific surface energy. In Fig. 2.3 the Gibbs energy as a function of the number of atoms in the cluster is shown. The resulting Gibbs energy of the new phase is shown as solid line. In case of very small clusters the Gibbs energy increases when the radius is increased. The formation of the surface requires more energy than obtained

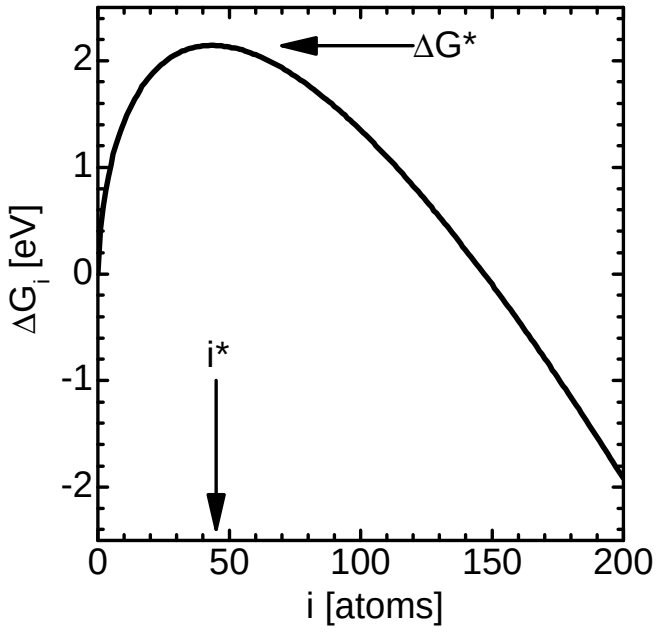


**Figure 2.3:** Gibbs energy $\Delta G_i$ versus number of atoms in the cluster $i$. The Gibbs energy decreases due to formation of a new volume but needs to build a new surface (increase of $\Delta G_i$). The resulting Gibbs energy exhibits a maximum at a critical cluster size $i^*$ associated to the activation energy $\Delta G^*$ [12].

by forming the stable volume. When the critical cluster size $i^*$ is exceeded the volume term dominates and the cluster is stabilized. The activation energy $\Delta G^*$ of the process can be associated with the critical cluster size $i^*$. For a spherical cluster Spinella et al. obtained:

$$i^* = \frac{32}{3}\pi\frac{\sigma^3}{\Delta g_V^3}, \tag{2.3}$$

$$\Delta G^* = \frac{16}{3}\pi\frac{\sigma^3}{\Delta g_V^2}, \tag{2.4}$$

thus, both, critical cluster size $i^*$ and activation energy $\Delta G^*$ depend on the ratio of the specific surface energy $\sigma$ and the Gibbs energy reduction $\Delta g_V$ by transition of an atom.

Around 1940 the so-called KJMA-model (Kolmogorov, Johnson, Mehl, Avrami) was formulated which is used to describe theoretically the kinetics of phase change.

The model assumes the existence of *germ nuclei* which become *growth nuclei* at a certain *nucleation rate*. The phase transition takes place at a certain *growth rate*. Additionally, the model considers the geometrical limitations for the growing grains by either surfaces of the system or neighboring grains. From the KJMA-model a characteristic functional equation is derived. This functional equation became known later as the Kolmogorov-Johnson-Mehl-Avrami equation, because of the contributions of all four authors (A.E. Kolmogorov [13], W.A. Johnson and R.F. Mehl [14] and M. Avrami [15, 16, 17]). In general the time dependent fraction of the new phase $R_C(t)$ within the volume under investigation can be written as:

$$R_C\,(t) \;\; = \;\; 1 - exp\,(-At^m)\,. \tag{2.5}$$

$A$ is a nucleation- and growth rate-dependent constant and $m$ characterizes the experimental conditions and dimension of the growing nuclei. Besides the fact that nucleation rate and radius growth rate of the nuclei are assumed to be constant, the most important assumption made in the KJMA equation is the existence of germ nuclei. In terms of minimization of the Gibbs energy *germ nuclei* can be understood as follows. The formation energy of a surface can be strongly reduced by already existing surfaces. A reduction of this surface energy is accompanied by a reduction of both, critical radius and activation energy to form a nucleus. This effect can be very strong. Thus homogenous and heterogeneous nucleation are distinguished, without and with already existing surfaces, respectively. The most probable heterogeneous nucleation sites correspond to the *germ nuclei* of the KJMA-model.

In Fig. 2.4 $R_C$ is plotted versus time $t$. Here, $R_C = 0$ corresponds to the initial phase before the process starts and $R_C = 1$ denotes the transformation of the entire volume. After the first nucleation the new phase fraction $R_C$ increases superlinearly because new *growth nuclei* are formed and the transformed volume increases with larger grains due to the constant radius growth velocity. The slope

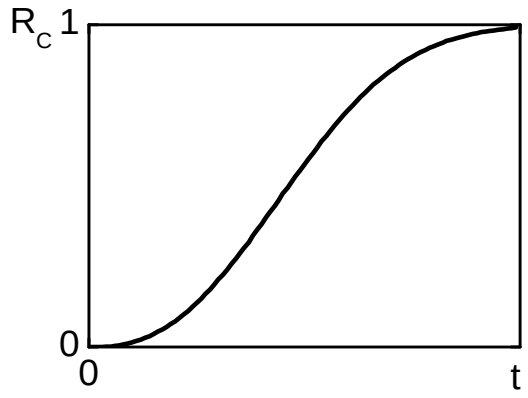


**Figure 2.4:** Diagram of the Kolmogorov-Johnson-Mehl-Avrami equation. The fraction $R_C$ of the new phase is plotted as a function of time $t$.

of $R_C$ decreases when nucleation ends, and neighboring *growth nuclei* collide and thus limit further growth. The KJMA model [18] and the theory of nucleation and growth during phase separation are still under discussion [19]. New simulation methods allow the modeling of more and more complex systems and enable comparison with results obtained by the analytic formula.

## 2.2 Solid Phase Crystallization (SPC)

Solid phase crystallization has been investigated since the early 1970s. Doping by ion implantation (introduced in 1966 [20]) caused damage to the crystal lattice in semiconductors. Therefore recrystallization processes were required which took place at low temperature in order to prevent diffusion of the implanted species. In order to investigate the recrystallization process crystalline silicon wafers were implanted with silicon atoms such that a surface layer of the wafer was amorphized. This was also referred to as solid phase epitaxy (SPE) because the reordering was found to start from the still crystalline phase of the wafer with the same orientation [1]. Of particular interest was the dependence of the crystallization behavior on

[1]Note: **Solid phase crystallization (SPC)** where the crystalline phase grows epitaxially on a **Si wafer** substrate is referred to as **Solid phase epitaxy (SPE)**. **Crystallization** of layers previously

the substrate orientation [21]. In this study a series of wafers cut with a $5°$ angular increment were amorphized in the way described above. The regrowth rate during annealing was determined by backscatter measurements. The regrowth rate was found to depend strongly on the substrate orientation. The regrowth rate as a function of the tilt angle of the surface normal to $\langle 100 \rangle$ orientation is shown in Fig. 2.5. The experimental data is fitted by a solid line. The regrowth rate on $\langle 100 \rangle$ orientated substrates was found to be 25 times higher than on $\langle 111 \rangle$ orientated substrates. For the model calculation the regrowth was assumed to be in $\langle 100 \rangle$ direction only. By tilting the $\langle 100 \rangle$ direction the growth is slower and is proportional to $\sin(54.17° - \alpha)$ where $\alpha$ is the tilt angle from $\langle 100 \rangle$ to $\langle 111 \rangle$ direction. This function is plotted as fit in Fig. 2.5 (dashed line).

The influence of dopants (P, B, As) [22] and impurities (C, N, O and noble gases) [23] (up to $0.5\,\mathrm{at.\%}$) on the recrystallization process was investigated by the same group. The regrowth rate was found to increase with the concentration of dopants and decrease with the concentration of impurities by up to one order of magnitude. In 1985 Pai et al. [24] used B and Ge to independently dope and stress amorphized layers prior to recrystallization. While B does both dope and stress the silicon, Ge only stresses the amorphized film. It was found that doping has a stronger effect on the recrystallization rate than stress. This led to the conclusion that an enhancement of the regrowth rate is an electronic effect of the participating dopants rather than stress effects caused by the implanted ions.

In 1979 Köster published a review on 'crystallization and decomposition of amorphous semiconductors' [25] stressing the importance of nucleation and growth rate. Both depend on the silicon transport from the amorphous to the crystalline phase and the change in Gibbs energy per atom during crystallization. While the crystallization of various semiconductors has been investigated the overview within this thesis focusses on SPC of amorphous silicon (a-Si).

In 1987 Iverson and Reif [26] pointed out that the thermal recrystallization of

amorphized by **ion-implantation** is referred to as **recrystallization** as opposed to crystallization of deposited amorphous Si layers.

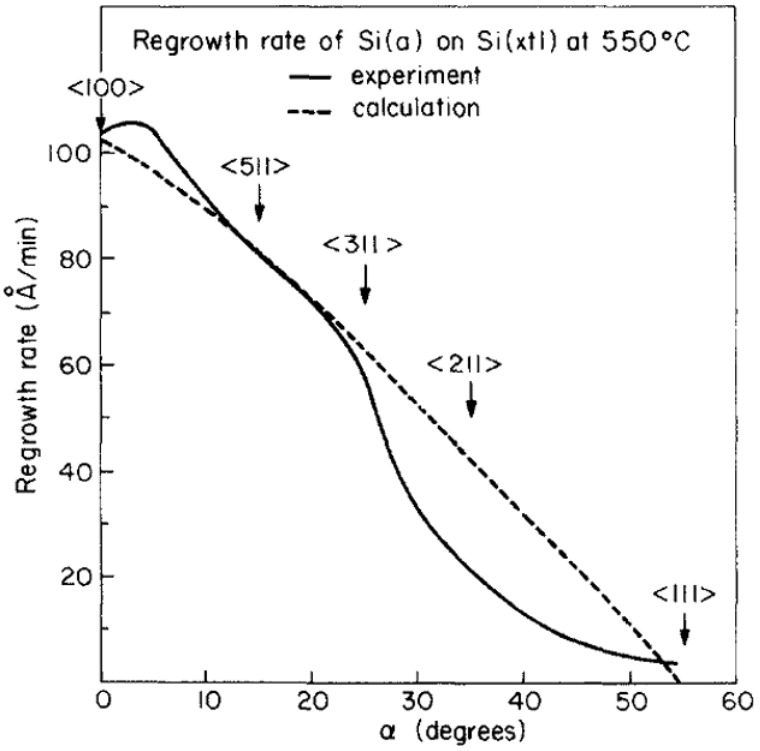


**Figure 2.5:** Orientation dependent solid phase epitaxy results from [21]. The regrowth rate is shown as a function of the tilt angle of the substrate to the $(100)$ direction. The experimental results fit reasonably with simple calculations made. The regrowth rate is $25\times$ faster for $\langle 100 \rangle$ than for $\langle 111 \rangle$.

amorphous silicon is inhibited by several activation barriers. Annealing of amorphized films on $SiO_2$ covered substrates at various temperatures and determination of the crystalline fraction and number of grains from TEM analysis allowed to determine different activation energies for solid phase crystallization (SPC). The most important ones are the activation energy for Si self-diffusion in amorphous silicon ($2.8eV$) and for the nucleation ($5.1eV$). The driving force for nucleation $\Delta G = 0.124eV/atom$ was determined by Donovan et al. by calorimetric studies [27]. This is in good agreement with other literature values and was verified by Spinella et al. [12] in 1998. Spinella stressed the role of atom jump rates to and from the clusters. At the critical radius, equivalent to the critical cluster size, both jump rates are equal. On this basis calculations were performed on the formation of critical clusters during solid phase crystallization of amorphous silicon. The

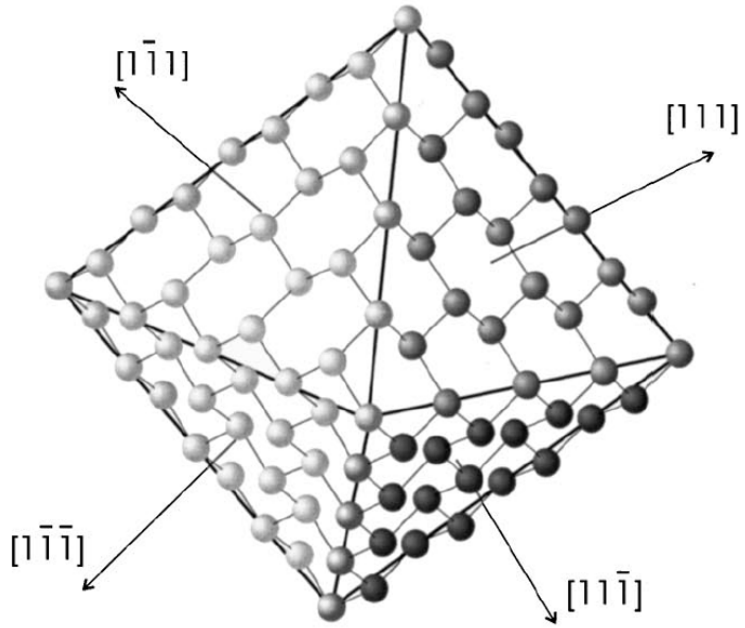


**Figure 2.6:** Sketch showing the octahedron/double pyramid formation in silicon crystallization. Spinella et al. [12] suggest that the critical clusters in solid phase crystallization Si crystallites embedded in the a-Si matrix assume the shape of a double pyramid with 111 faces, <110> ledges and <100> tips.

critical cluster size was estimated to about 45 atoms during the crystallization of spherical clusters. In order to reduce the total surface energy the surfaces of lowest energy are formed. Fig. 2.6 illustrates the case for silicon. As can be seen Si forms an octahedron (double pyramid) with $(111)$ surfaces. The $(111)$ surfaces are stabilized and growth takes place along the $(110)$ ledges of the pyramid covering the $(111)$ surfaces layer by layer. This consideration is used for modeling later (chapter 5).

In the early 1980s, research on silicon on insulator (SOI) technology for MOSFETS led to an increased interest in solid phase crystallization. At the end of this decade the application of thin film transistors (TFT) in displays and sensors led to the first solid phase crystallization experiments on foreign substrates, like glass. In the early 1990, Sanyo investigated the possible use of SPC for solar cells. Even though promising results where obtained with a laboratory cell efficiency of $\eta = 9.2\,\%$ on an area of $1\,\mathrm{cm}^2$ [8] further efforts were quitted for reasons unknown. In

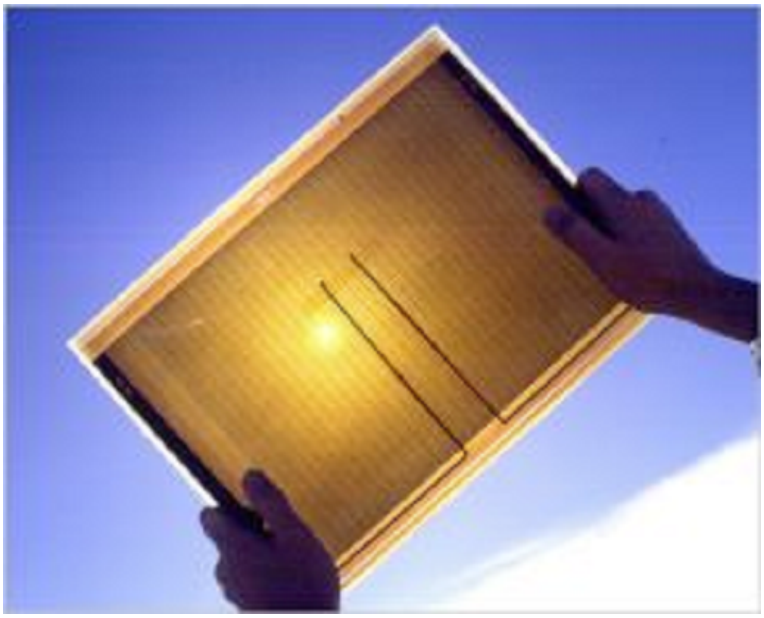

**Figure 2.7:** Crystalline silicon thin film module made by SPC (source: http://www.pacificsolar.com.au)

January 2004 *CSG Solar AG* (formerly *Pacific Solar Ltd.*) set the cornerstone for a new factory in Thalheim, Saxony-Anhalt. CSG is the abbreviation for crystalline silicon on glass. It is the first company attempting to produce solar cells made by solid phase crystallization (SPC) on an industrial scale. Prototypes produced by *Pacific Solar* (Fig. 2.7) have reached a module efficiency of above $8\,\%$ on an area of $96\,\mathrm{cm}^2$ [28]. It is believed that a module efficiency of about $10\,\%$ can be reached at very low cost. These efficiencies are still below the tandem solar cells efficiencies described above [7]. Besides the efficiency and the fabrication cost of a module the yield is a very crucial parameter which determines success or failure of the thin film technologies because of the large areas processed at a time.

## 2.3 Metal-Induced Crystallization (MIC)

At about the same time SPC was investigated for the first time, contact metallization in integrated circuits was found to dissolve silicon. This process was found to be enhanced in case of heated metal-silicon contacts [29].

Combining this effect of metals on semiconductors and the idea of solid phase crystallization it was found that metals in contact with amorphous silicon strongly reduce the crystallization time and temperature. Two microscopic models were suggested explaining the observed effect. Hiraki [30, 31] deposited monolayers of gold on amorphous silicon. He found that only upon depositing four monolayers or more crystallization was enhanced. He concluded that some type of bulk metal must be formed. The bulk is needed because a free electron gas needs to be formed. The wave function of the free electron gas extends into the amorphous silicon screening the covalent Si bonds. The screened bonds are weakened and thus crystallization is faster. Tu [32] suggested an interstitial model for near-noble transition metals. Such metals lack one electron to achieve noble gas configuration. If such a metal atom would be inserted in an interstitial position of the Si lattice an electron from the covalent bonds surrounding this atom would be transferred to the metal. This weakens the bonds around it, enhancing crystallization.

In 1972 S.R. Herd [33] compared the influence of different metals on the crystallization temperature of amorphous silicon and germanium. Metals forming silicides (Ni, Pd, Cu) are distinguished from eutectic metal-silicon systems (Al, Au, Ag).

Ni in contact with Si forms a $NiSi_2$ phase. The chemical potential for Ni is lower at the $NiSi_2$/a-Si interface than at the $NiSi_2$/c-Si, thus Ni diffuses to the a-Si side. At the same time Si diffuses in the opposite direction. This makes the silicide phase move through the a-Si silicon and leaves crystalline silicon behind. Depending on the growth parameters the silicide phase either moves anisotropically leading to *needle-like* crystallites or isotropically leading to *disk-like* grains [34]. MIC allows to grow large and disk-like grains. Fig. 2.8(a) shows a micrograph of disk-like Si grains from a Pt-induced crystallization process with annual ring-like structures [35]. The Si grains exhibit a grain size of up to 500 $\mu$m. The ring structures correspond to interruptions in the annealing process. Fib. 2.8(b) shows a micrographs in the case for Ni-induced crystallization of a-Si [36]. The grain size is about 50 $\mu$m. Again rings were found due to interruptions during the annealing, but this

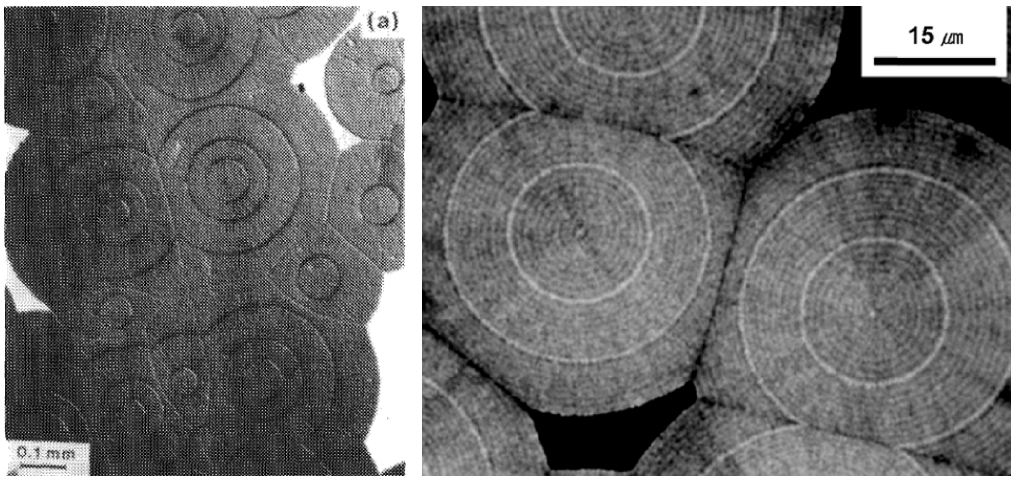


(a) (b)

**Figure 2.8:** Scanning electron micrographs of annual ring like growth in Pt-induced crystallization of a-Si (a) [35] and in Ni-induced crystallization (b) [36]. The ring structures appear due to an interruption of the annealing process.

time additional rings also appeared which could not be explained.

Sohn et al. [37] investigated the crystallography of disk-like grains grown in a Ni-induced crystallization process enhanced by an electric field applied by two metal bars on the sample. This is called field-enhanced silicide-mediated crystallization (FE-SMC) and was first introduced by Jang et al. [38]. Sohn et al. showed by Electron Back Scatter Diffraction (EBSD) and selective area diffraction (SAD) that the obtained grains were monocrystalline. The grains each have a single orientation, but their orientation is not the same as that of neighboring grains.

The orientation dependence of the surface energy can lead to preferential growth of the silicide within the a-Si layer. Hayzelden et al. [39] suggested the formation of $NiSi_2$ double pyramids (Fig. 2.9) with $(111)$ crystal faces as the lowest energy configuration, which corresponds to the suggestion made by Spinella et al. in SPC of a-Si (Fig. 2.6). Fig. 2.9 shows a sketch of the a-Si film with three possible alignments of a double pyramid. Depending on the alignment of the double pyramids in the a-Si layer different preferential orientations are obtained. The alignments correspond to different crystal orientations of the double pyramid normal to the surface of the a-Si film. From left to right: $(100)$, $(110)$ and $(111)$ orientation. If

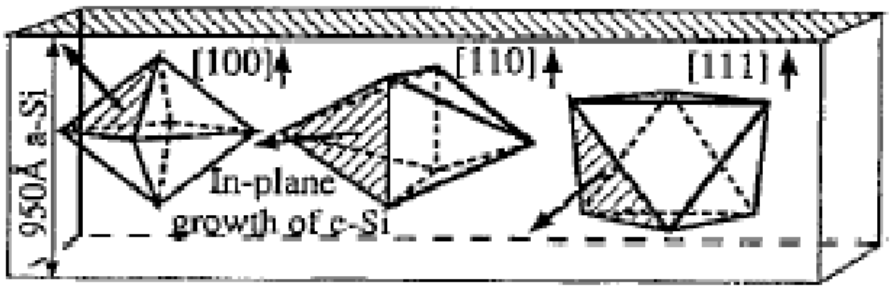


**Figure 2.9:** Hayzelden's double pyramid alignment within a-Si thin films for Ni-induced crystallization [39]. Depending on the alignment the double pyramid is confined differently within the a-Si film. In case of the pyramid orientated in $(110)$ direction relative to the surface normal (middle) four $(111)$ planes grow parallel to the substrate leading to the fastest growth.

the double pyramid is aligned with the $(110)$ orientation normal to the layer, four $(111)$ planes lie in the main lateral growth direction. Because the growth direction is in the $(111)$ direction, this leads to the $(110)$ orientation as the fastest growth and preferential orientation.

The metal-induced crystallization of amorphous silicon in eutectic forming metal-silicon systems differs from the silicide forming metals. Both phases in the eutectic system remain separated throughout the process. They can only dissolve a certain concentration of the other species. The Al/Si phase diagram is shown in Fig. 2.10. The horizontal line at $850\,\mathrm{K}$ ($577\,°\mathrm{C}$) together with the intersecting liquidus lines at a Si content of $12.2\,\%$ are characteristics of an eutectic system. The intersection point is the eutectic point with the corresponding eutectic temperature. The eutectic forming MIC process was separated into three major steps by Ottaviani et al. [40]: (i) the dissociation of Si atoms from the amorphous phase into the metal, (ii) the diffusion of silicon atoms through the metal, and (iii) the crystallization of the dissolved Si by either nucleation of new cluster or agglomeration on existing crystallites. These authors suggested that energetically, the driving force of the process is the higher Gibbs energy of the amorphous phase compared with that of the crystalline phase. Furthermore, it was suggested that the metal induced crystallization is faster due to the kinetically fast reaction path where the metal

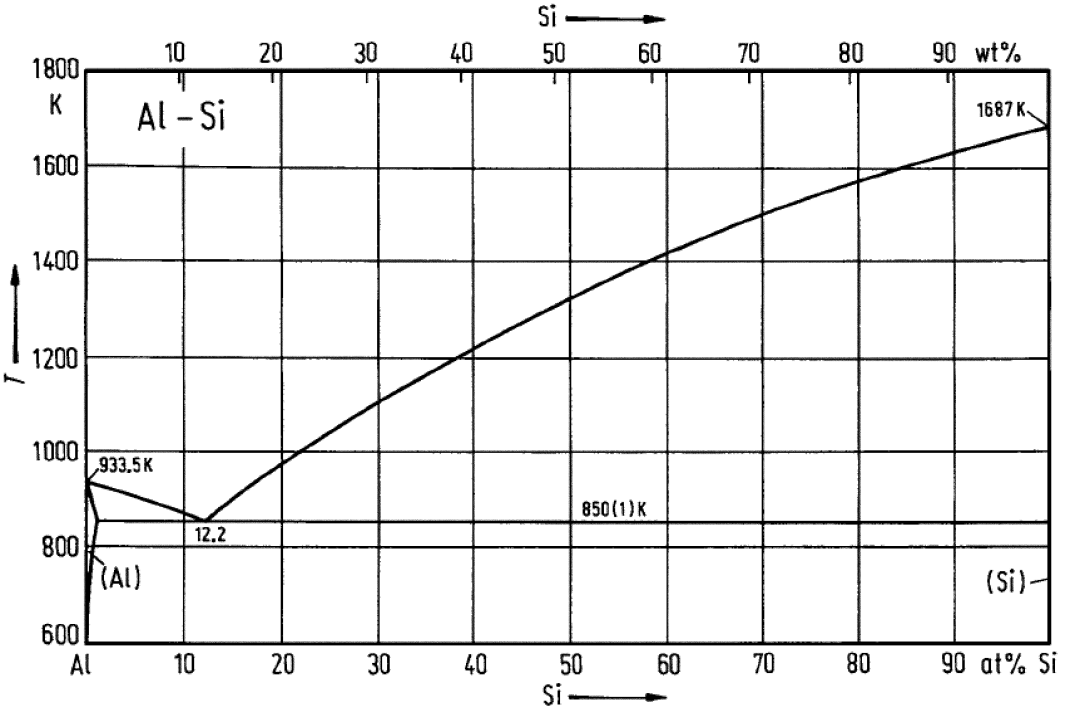


**Figure 2.10:** Al/Si phase diagram. The temperature versus the Si content in the Al is shown. The Al and Si attempt to reach the equilibrium state by mixing corresponding to the lines indicated in the phase diagram at the each temperature. The equilibrium lines separate the different phases. The Al/Si system is a eutectic system. The eutectic temperature is at $577\,°C$ and the eutectic point is at a silicon concentration of $12.2\,\%$.

serves as a solvent medium for the amorphous material.

Konno and Sinclair have conducted ex and in-situ cross-sectional transmission electron microscopy studies on Al/a-Si multilayers [41, 42]. They found that silicon nuclei are formed within the Al layer. This supports the three step model of dissociation, diffusion and nucleation.

The differences in crystallization mechanism also lead to a difference in applications. Silicide forming metals (Ni) are mostly used in so-called metal-induced lateral crystallization (MILC) processes. The metal crystallizes the amorphous silicon laterally in the region of interest (ROI), e.g. the channel of a TFT. Thus, the silicide next to the ROI can be ignored and remains there. Non-silicide forming metals like Al function merely as catalysts. The metal and silicon are dissolved up to the solubility limit. The metal phase can easily be removed. Additionally, Ni creates deep

level acceptor levels at $230meV$ above the valence band and at $350meV$ below the conduction band in crystalline silicon, while Al is a shallow acceptor only $67meV$ above the valence band [43]. Thus Ni enhances carrier recombination and thus strongly decreases the minority carrier lifetime. In photovoltaic applications the photogenerated minorities make minority carrier life time crucial for good solar cells. Thus Al is favored over Ni in PV applications.

## 2.4 Aluminum-Induced Layer Exchange (ALILE)

In order to obtain a continuous poly-Si layer on large area substrates without any metal remainders a special case of aluminum-induced crystallization (AIC) has been developed. This specific process is referred to as aluminum-induced layer exchange process (ALILE). In 1976 aluminum-induced crystallization was used in a type of layer exchange process by R.L. Boatright and J.O. McCaldin [44]. Fig. 2.11 shows their experiment schematically. In Fig. 2.11(a) an initial stage of the experiment is shown which was published by J.O. Best and J.O. McCaldin one year earlier [45]. A hole was made by photolithographic means in a Si oxide layer covering a silicon wafer. After deposition of Al on top of the oxide covered wafer and annealing at $550\,°C$ for $5..25\,\mathrm{min}$, the Al dissolved the Si beneath the hole. Boatright et al. evaporated amorphous silicon onto the Al layer (Fig. 2.11(b)) and annealed the specimen again at $475..525\,°C$ for another $10..20\,\mathrm{min}$. It was found that the hole is refilled with silicon (Fig. 2.11(c)). Thus an amorphous layer on top of the Al fills a hole at the bottom of the Al.

Majni and Ottaviani investigated the growth kinetics in solid phase epitaxy (SPE) by deposition of Al/a-Si double layers on differently orientated Si wafers [46, 47, 48] and actually mentioned for the first time: 'the Si and Al exchange position' [49]. Tsaur et al. [50] used a-Si SPE through an Al layer to form highly p-doped emitters on n-doped c-Si wafers. The separated Al layer was removed and the resulting solar cells reached an efficiency of $10.4\,\%$.

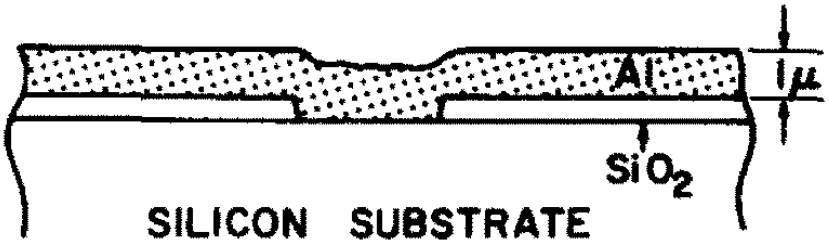


(a)

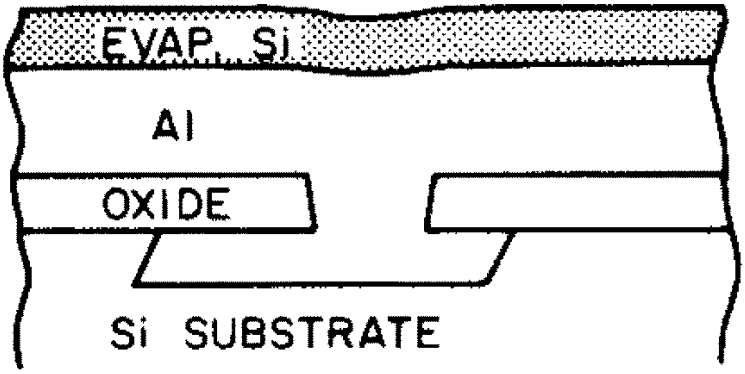


(b)

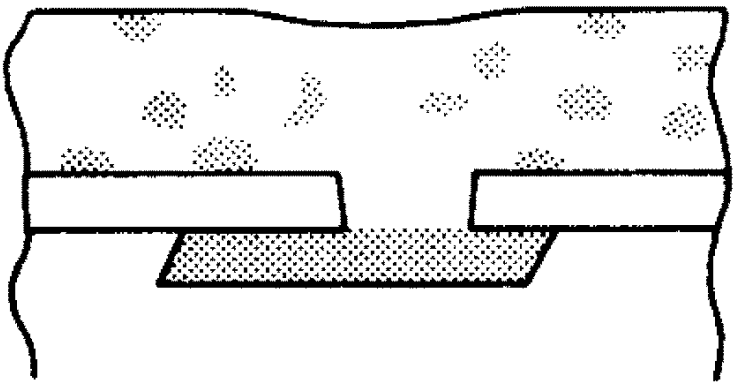

(c)

**Figure 2.11:** First observation of a layer exchange type phenomenon: (a) Al evaporated on a thermal Si oxide with hole on top of a Si wafer [45]. Upon annealing at $550\,°C$ for $5..25\,\mathrm{min}$ Al dissolves the Si beneath the hole. (b) Evaporating amorphous Si on this structure and (c) heating the sample again at $475..525\,°C$ for another $10..20\,\mathrm{min}$ lead to refilling of the hole with Si [44].

Many years later in 1998 L. Koschier et al. suggested the use of such a layer exchange as back surface field formation in solar cells [51]. O. Nast et al. transferred the idea of a layer exchange on wafers to form a polycrystalline silicon (poly-Si) layer on glass [9].

O. Nast et al. found that a glass/Al/a-Si stack can be transformed in a glass/poly-Si/Al(+Si) stack in an annealing step below the eutectic temperature of the Al/Si-system. In Fig. 2.12 Focused Ion Beam (FIB) images are shown of the cross section of this layer stack [52]. Micrograph (a) shows the initial Al/Si layer stack and (b) after $5\,\mathrm{min}$ annealing at $500\,°\mathrm{C}$. A small crystalline silicon cluster was formed in the Al layer. This cluster grows until it is vertically confined within the Al layer. (c) shows the specimen after $10\,\mathrm{min}$ annealing. The grain continues its growth in lateral direction only. The last micrograph (d) shows the sample after $60\,\mathrm{min}$ annealing. Now, the entire layer is exchanged and a continuous poly-Si layer is formed on the glass substrate. O. Nast called this process aluminum-induced layer exchange process (ALILE) [53]. The interface between the initial Al and a-Si layer is essential for the layer exchange. An oxide layer is needed on top of the Al layer for the process. The oxide can be formed by simple exposure of the Al to ambient air. This oxide layer functions as a permeable membrane separating the top and bottom layer throughout the process [54]. Additionally the oxide layer is a diffusion barrier controlling the diffusion of silicon into the aluminum and vice versa. A silicon excess is found to be needed in order to replace the complete Al layer by poly-Si.

O. Nast developed a model for the ALILE process dividing the overall process into four steps as sketched in Fig. 2.13. Step 1 involves the interaction of amorphous silicon with the Al and the dissociation of the amorphous phase across the oxidized Al/Si interface. Once Si is dissolved in the metal, the Si atoms diffuse within the Al layer (step 2). The Si nucleates within the Al layer (step 3). The nuclei become grains and grains grow by incorporation of further Si atoms until the entire Al is replaced (step 4).

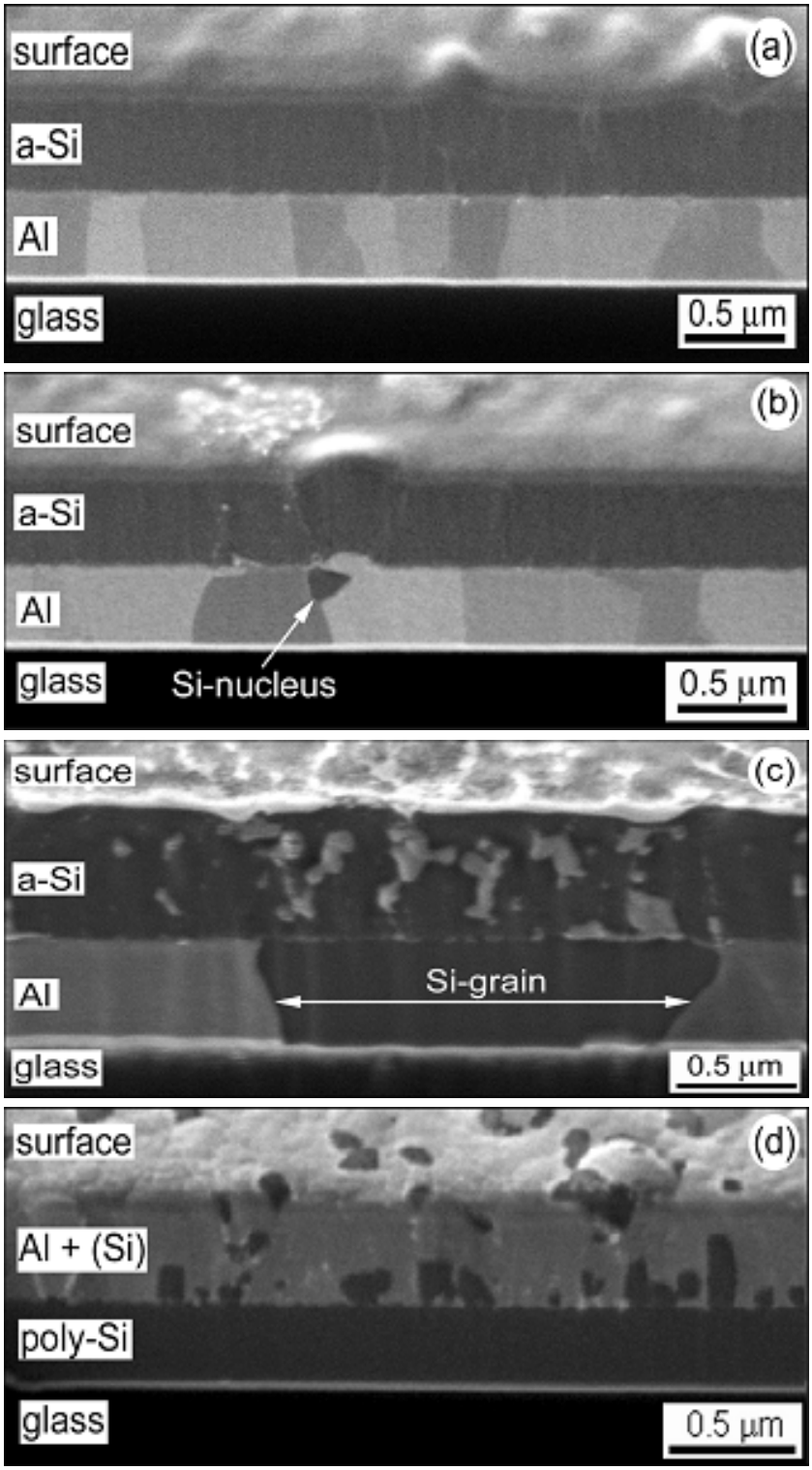


**Figure 2.12:** FIB images of the ALILE process. (a) Initial stack; (b) Annealing at $500\,°C$ for $5\,\mathrm{min}$: nucleus formation; (c) $10\,\mathrm{min}$ annealing: confinement of the growing grain within the Al layer, (d) $60\,\mathrm{min}$ annealing: continuous layer formation [52].

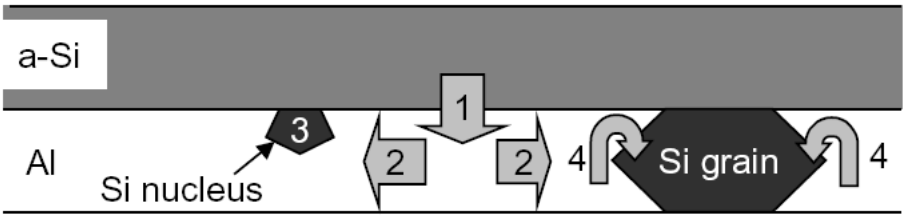


**Figure 2.13:** ALILE growth model suggested by O. Nast [53]. Step 1: Si dissolution and transport into the Al layer. Step 2: Si diffusion in the Al layer. Step 3: Si nucleation. Step 4: growth of Si grain.

This model was extended by P. Widenborg et al. [55]. They considered also the process in the top layer (Fig. 2.14). While process steps 1, 2 and 3 correspond to the steps suggested by O. Nast, here step 4 describes the diffusion of Al into the top layer. Al is displaced by Si grains and forced to diffuse into the a-Si top layer (step 4a). The a-Si crystallizes in presence of the Al and small Si crystallites form in the Al top layer. The Al in this mixed phase dissolves further a-Si and grows (step 4b) competing with the Si growth in the bottom layer in this model. While the poly-Si in the bottom layer grows supplied by step 5, silicon is also crystallized in the top layer. Small nanocrystalline Si (nc-Si) crystallites will agglomerate at the more compact central Si islands, even when the actual layer exchange is completed (step 6)

The formation of a stable c-Si phase within the Al in the top layer can be thought of as formation of idealized 'double cylinder' shaped Al/c-Si-clusters in top view. A sketch of such a 'double cylinder' embedded in the a-Si matrix is shown in Fig. 2.15(a). Fig. 2.15(b) shows several of these 'double cylinders' corresponding to the optical micrograph in Fig. 2.15(c) [56] obtained at the top layer.

The driving force of the entire process was assumed by O. Nast to be the chemical potential difference between the amorphous and crystalline phase (Fig. 2.16). It is proposed that the Al layer is in equilibrium with both the amorphous and the crystalline silicon phase at the interfaces. Then the difference of the chemical potentials leads to silicon diffusion within the aluminum from the a-Si/Al interface to the Al/c-Si interface.

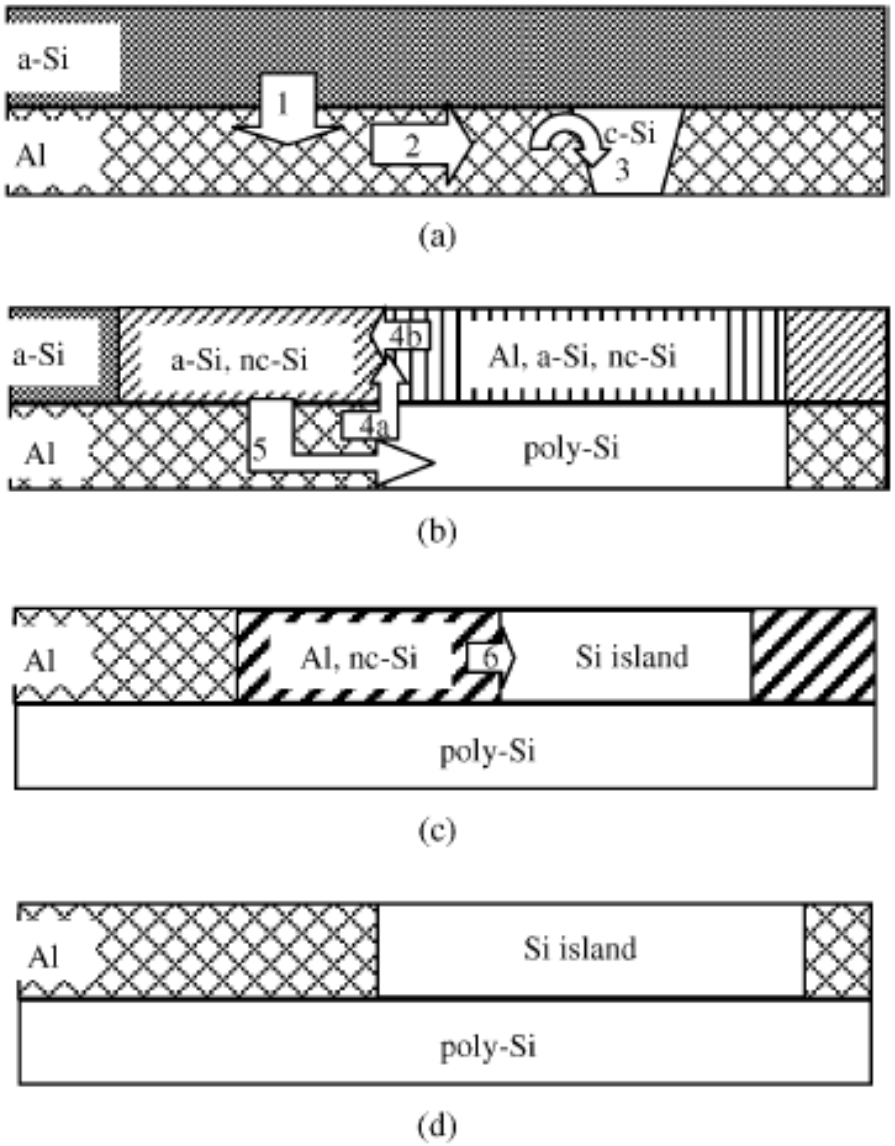


**Figure 2.14:** ALILE growth model by P. Widenborg et al. [55]. The process in the top layer is also taken into account. Formation of Si islands in top layer was found to compete with the crystallization process in the bottom layer. For details see text.

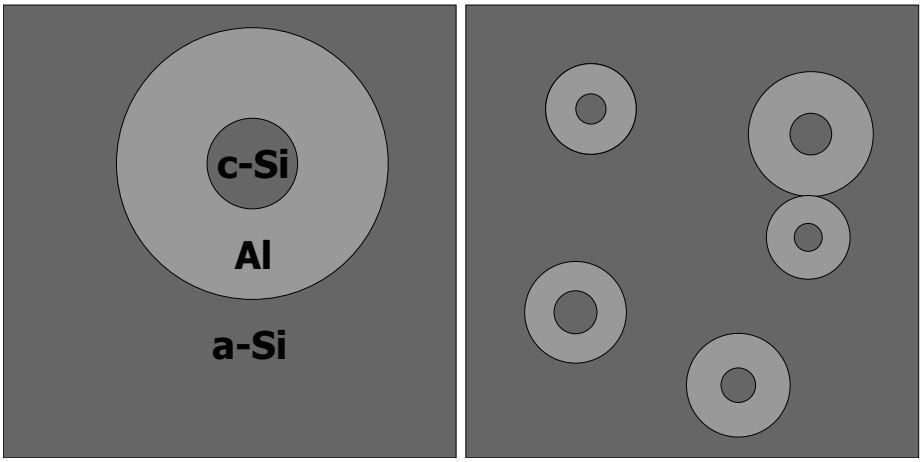


(a) (b)

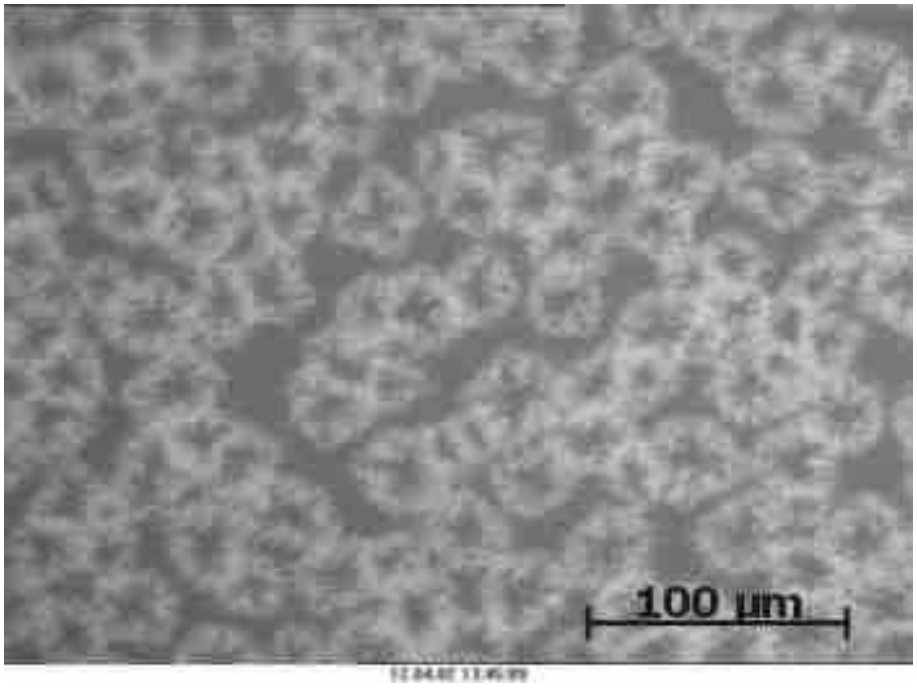


(c)

**Figure 2.15:** 'Double cylinder'-shaped Al/c-Si clusters in the top layer in top view. (a) Single 'double cylinder'. (b) Multiple 'double cylinders'. (c) Optical micrograph of 'double cylinders' [56].

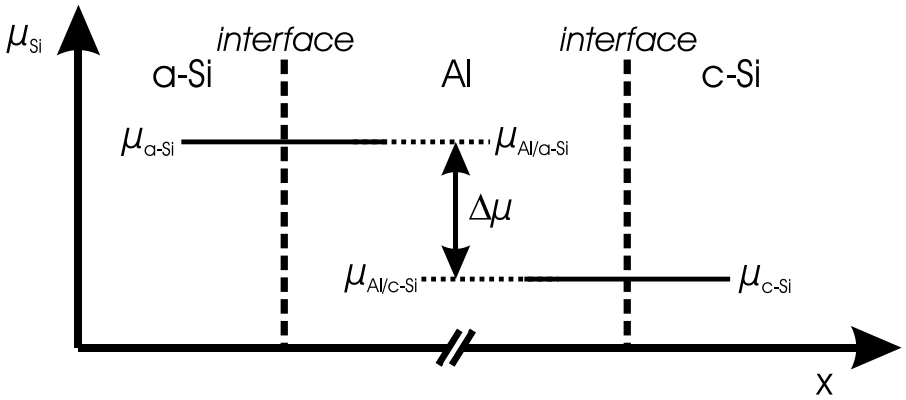


**Figure 2.16:** Chemical potential $\mu_{Si}$ versus distance $x$. On the left is the a-Si phase, on the right is the c-Si phase. Both are assumed to be in equilibrium with the Al. Thus the difference $\Delta\mu$ of the chemical potential of the a-Si $\mu_{a-Si}$ and the c-Si $\mu_{c-Si}$ drives the diffusion of Si within the Al layer. The overall driving force of the ALILE process is the Gibbs energy reduction from amorphous to crystalline silicon [53].

A key feature of the ALILE process is the suppression of nucleation by existing grains and the resulting large grain size of above $10\,\mu\mathrm{m}$. Silicon diffusion towards growing grains leads to the formation of concentration gradients [52]. Fig. 2.17 shows in a schematic diagram the silicon concentration profiles between two neighboring grains. The silicon concentration within the grains, the density of silicon, is $c_g$. The growing silicon grain decreases the silicon concentration just in front of the grain to $c_i$. Far away from the grain the Si concentration is $c_n$, the concentration at which nucleation is likely to occur. Around the grains is a region with a lowered concentration, referred to as depletion regions. The width of the depletion region is $d$. While new nucleation is possible in the supersaturated region between the depletion regions, it is suppressed once the depletion regions overlap. At a distance of $2d$ no further nucleation is possible.

## 2.5 Current research involving ALILE layers

A possible solar cell concept involving ALILE seed layers is shown schematically in Fig. 2.18 [57]: (a) After deposition of the initial Al and a-Si layer (b) the poly-

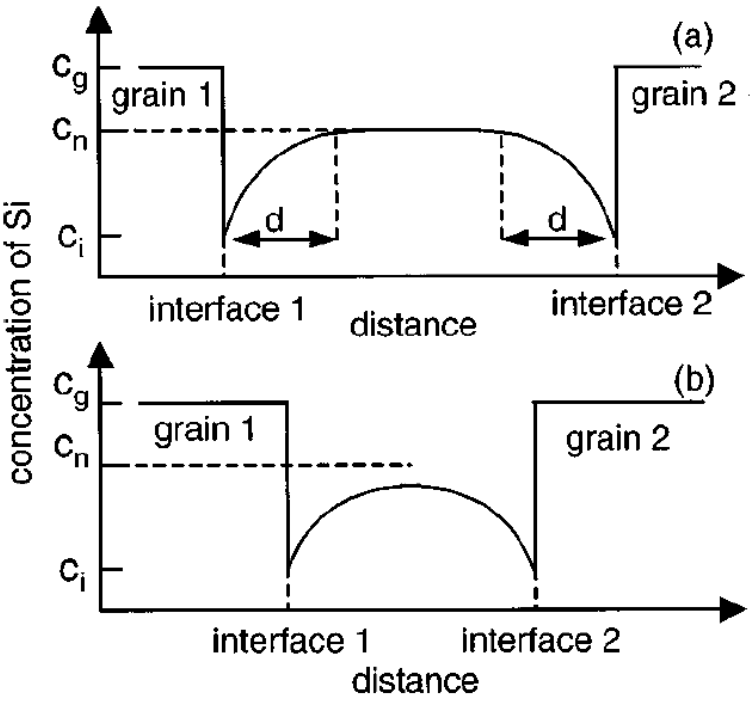


**Figure 2.17:** Si concentration profile around growing grains. The Si concentration within the grains is $c_g$. Right in front of the grain it is $c_i$. Far away from the grains is the nucleation concentration $c_n$. Si is depleted in the concentration profiles on a distance $d$. (a) If neighboring grains are further then $2\,d$ apart nucleation is still possible. (b) Once the grains are closer than $2\,d$ nucleation is suppressed. [52].

Si layer is formed by the ALILE process. (c) On the top of the poly-Si film an Al layer with silicon inclusion is formed which has to be removed. (d) The poly-Si layer is subsequently thickened by low-temperature epitaxy forming a $p$-doped absorber. Finally, a low temperature, $n^+$-emitter is deposited. This can either be done epitaxially by changing the dopant or by deposition of an amorphous silicon emitter. In the latter case a transparent conducting oxide (TCO) layer is needed to enhance the lateral conductivity of the emitter. A mesa structure has to be etched in order to define the solar cell area and contact the absorber layer.

Historically, the University of New South Wales (UNSW) in Sydney and the Hahn-Meitner-Institut Berlin (HMI) were both involved in ALILE research due to O. Nast preparing his dissertation in both facilities. In order to produce a smooth, epi-ready surface on the ALILE layer a wet chemical lift-off process for the Si islands

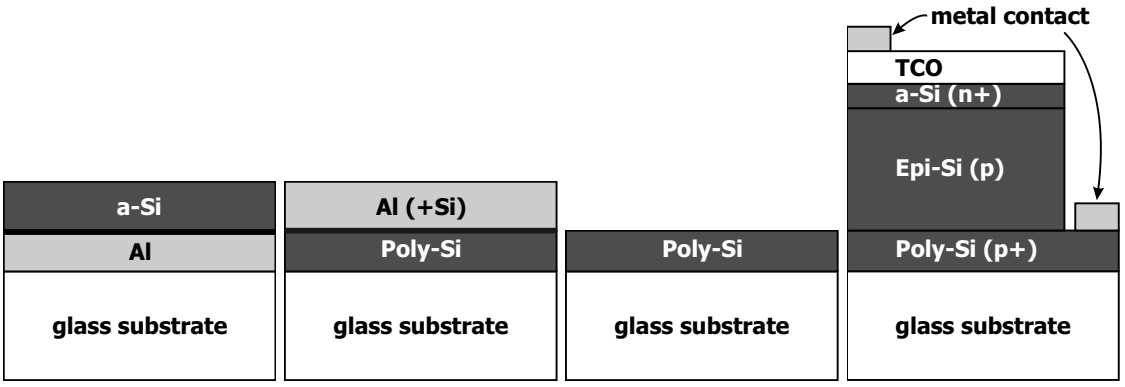


**Figure 2.18:** Schematic illustration of the formation of a Si thin film solar cell on glass. (a) The layers of the initial stack; (b) exchange position by annealing at about $500\,°C$; (c) the top layer has to be removed in order to uncover the poly-Si layer; (d) After $p$-absorber formation by low-temperature epitaxy a low temperature $n^+$-emitter, e.g. a thin a-Si layer, forms the p-n-junction. The cell is cover by a transparent conductive oxide layer (TCO) which enhances the lateral conductivity. The cell is finished by forming a mesa structure and front and back contacts.

within the Al layer has been developed at the UNSW. Thereafter ALILE seed layers were successfully thickened epitaxially for the first time by ion assisted deposition (IAD) [58]. In the last two years different cell concepts have been developed involving IAD and SPE from a-Si layers deposited on the seed layer [59].

The Hahn-Meitner-Institute is coordinating a EU-Project called 'METEOR' (ENK5-CT-2001-00543) dealing with the above described solar cell concept [60]. The members of this project are the Interuniversity Microelectronics Center (IMEC) in Leuven, Belgium, the Vienna University of Technology (TUW) and the Catholic University Leuven (KUL). The project includes a high and a low temperature approach.

At IMEC the high temperature route is followed which offers a faster path to successful solar cell fabrication than the low temperature approach. ALILE seed layers on ceramics substrates are studied. It was found that smoothening the ceramic substrates by applying a flowable oxide (FOx) is beneficial. Epitaxially thickened with high temperature atmospheric pressure chemical vapor deposition (APCVD),

IMEC has achieved solar cell efficiencies of up to $4.5\,\%$ [61]. The influence of rapid thermal annealing (RTA) and hydrogen passivation of defects in the absorber layers is examined at IMEC in order to improve the solar cell parameters [62].

HMI focusses on the low temperature route which promises an even higher potential in cost reduction than the high temperature approach. The ALILE seed layers are prepared on glass substrates limiting all process temperature to below $600\,$°C. It was shown that small amounts of oxygen present during Al deposition decrease the layer exchange process time, but upon further increasing the oxygen amount has the opposite effect occurs [63]. Samples are thickened epitaxially using electron cyclotron resonance chemical vapor deposition (ECRCVD) [64]. Characterization of defects in low temperature epitaxy is very important and done at HMI by defect etching, electron spin resonance (ESR) and photoluminescence (PL) [65].

Both approaches are supported by electron microscopic characterization methods like transmission eleoctron microscopy (TEM), high resolution TEM (HRTEM) and electron energy loss spectroscopy (EELS) at TUW [66]. At KUL the use of other metals, e.g. Sb, for alternative crystallization concepts are studied in order to obtain n-doped poly-Si.

Besides the activities at the UNSW and within the METEOR project, many other institutions started research in ALILE related research during the last couple of years. At Samsung in South Korea, it was found that the formation of the preferential orientation depends upon the annealing temperature; the lower the annealing temperature, the higher the preferential $(100)$ orientation [67].

Toyota explored the use of SPC of a-Si on ALILE seed layers for solar cell applications [68]. Some simulations were done to extrapolated the future goals for solar cells involving ALILE seed layers which claimed that efficiencies of about $13\,\%$ could be achieved when various solar cell parameters are improved [69]. Unfortunately, no time frame for these considerations is given.

Slaoui et al. [70] in Strasbourg, France have investigated the influence of the structure of the silicon precursor on the layer exchange process. They found that

nanocrystalline Si (nc-Si) yields the smoothed surface of the resulting film. Using high temperature CVD they achieved epi-layers on top of ALILE seed layers with grain sizes up to $60\,\mu\mathrm{m}$. The grain sizes were determined by defect etching of the grain boundaries [71].

At the London South Bank University, low temperature epitaxy using ECRCVD on an inverse ALILE seed layer structures is studied [72, 73]. The structural quality of the films is analyzed using electron back scatter diffraction (EBSD) and X-ray diffraction (XRD) analysis.

The Academy of Science in Sofia, Bulgaria conducts experiments with different Al, Si layer sequences are conducted [74]. Also, the influence of different annealing atmospheres on the layer exchange process has been explored indicating that the use of hydrogen in the annealing atmosphere leads to improved strutural properties of the resulting poly-Si film [75].

At the Technical University München the use of the ALILE process for crystallization of amorphous SiGe is investigated. Here, it was found that ALILE is suitable for crystallizing binary amorphous material without segregating different phases [76]. The optical and electrical properties of the resulting poly-crystalline films were found to be comparable with high quality crystalline SiGe films [77].

In the USA many groups (NREL [78, 79], Caltech [80], University of Berkeley, University of Arkansas and University of Arizona) have recently started working on thin film c-Si devices either making direct use of the poly-Si layer formed by ALILE or using similar thin film seed layer concepts.

At the Hahn-Meitner-Institut (HMI), where this work has been done, a group of researchers is dealing with solar cell concepts based on the ALILE process. As mentioned before the poly-Si layers exhibits not only large grains but also a preferential $(100)$ orientation [81]. Due to the high hole density ($2 \times 10^{18}\,\mathrm{cm}^{-3}$ [82]) ALILE poly-Si layers are not suitable as absorber layers. But both the large grain size and the preferential $(100)$ orientation make ALILE layers eligible as templates (seed layers) for low temperature ($< 600\,$°C) epitaxial growth of an absorber layer. At

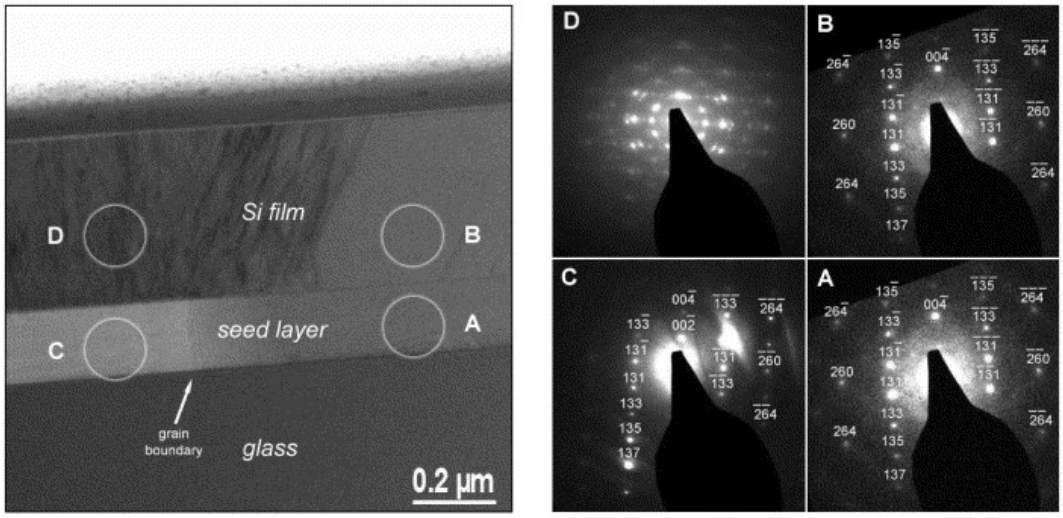


**Figure 2.19:** TEM cross section (left) and diffraction patterns (right) of a film deposited on a ALILE seed layer on glass. The circles mark the positions for the selected area aperture for electron diffraction. The diffraction images are aligned with respect to the neighboring TEM image. Position A is aligned in $(100)$ direction normal to the substrate and position C is tilted by $7.8°$. Epitaxy was successful on A but not on C.

the Hahn-Meitner-Institut the main method used for low-temperature epitaxy has been electron cyclotron resonance chemical vapor deposition (ECRCVD) [83]. Rau et al. showed that the ALILE seed layer could be thickened by ECRCVD to above $2\,\mu\mathrm{m}$ on grains with an orientation close to $(100)$ [64]. In Fig. 2.19 a TEM cross section and the corresponding diffraction patterns of the glass/seed layer/epitaxial layer stack are shown. The grain on the right side is epitaxially thickened, whereas the one on the left caused finecrystalline growth. It was found by diffraction analysis that the right grain is $(100)$ orientated, but the left grain's $(100)$ direction is tilted by $7.8°$ with respect to the surface normal. This demonstrates the significance of the preferential $(100)$-orientation for low temperature epitaxy.

Another low-temperature epitaxial technology used at HMI is the pulsed sputter deposition system [84]. Fig. 2.20 shows a transmission optical micrograph of an epitaxial film ($1700\,\mathrm{nm}$) grown on top of an ALILE layer by pulsed sputter deposition. Clearly different areas can be distinguished. The bright areas were verified to correspond to epitaxial growth. The dark areas are expected to correspond to

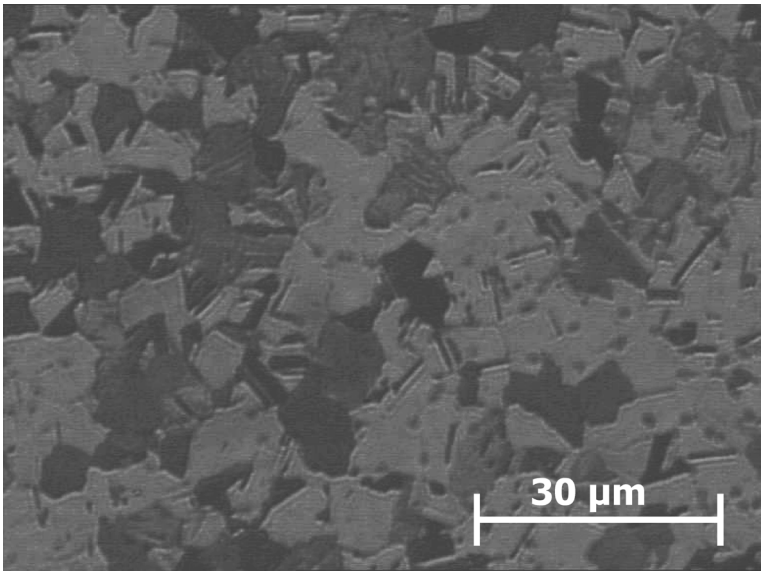


**Figure 2.20:** Transmission optical micrograph of an ALILE layer thickened by pulsed sputter epitaxy by about 1700 nm.

fine crystalline growth [2]. Thus the growth still has to be improved a lot, but first results are promising.

First solar cells were processed during the course of this thesis at HMI. The resulting current-voltage (IU) curve (Fig. 2.21(a)). An open circuit voltage of $V_{OC} = 254\,\mathrm{mV}$, a short circuit current of $J_{SC} = 6.7\,\mathrm{mA/cm^{-2}}$ and a fill factor of $FF = 0.35$ result in an efficiency of $\eta = 0.55\,\%$. The internal quantum efficiency curve (Fig. 2.21(b)) of the best cell so far is shown. The best quantum efficiency is about $26\,\%$ at $450\,\mathrm{nm}$. It is evident, that there is still a lot of work to do. All cell parameters offer chances of improvement. The diode itself does not show a good rectifying characteristic. Series and parallel resistances have to be improved. The cell layout needs to be modified. Finally, light trapping has to be incorporated in order to absorb more photons in the layer.

This thesis is embedded in the activities at HMI. The main focus is to understand the mechanism of nucleation and growth in the aluminum-induced layer exchange process. This should lead to an understanding and thus improvement of the self-

[2] This fast, non-destructive method of analyzing Si thin film using an transmission optical microscope was suggested by Straub et al. [85].

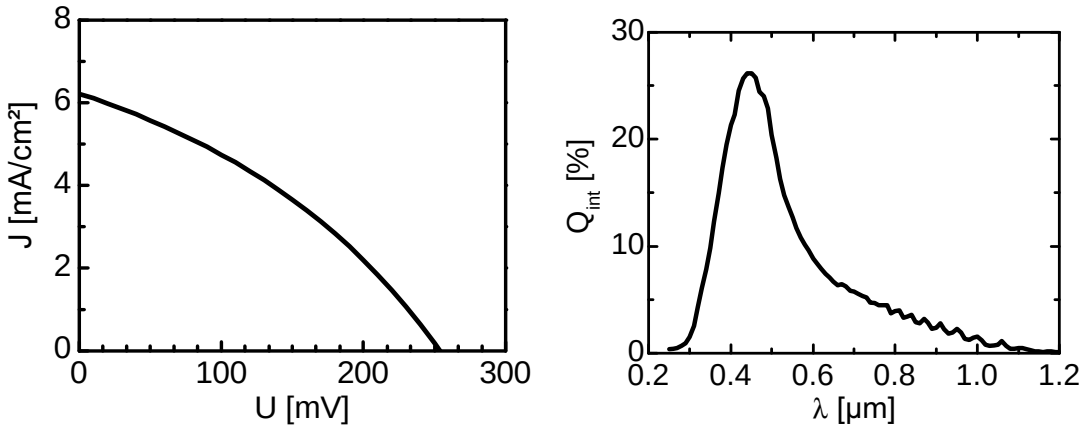


(a) (b)

**Figure 2.21:** Current-voltage curve (a) and internal quantum efficiency for one of the first solar cells processed at HMI.

limited nucleation suppression. The goal is to achieve large grained layer with grain sizes much larger than the final film thickness of about $2\mu\mathrm{m}$. In order to improve the results of the subsequent low-temperature epitaxy the fraction of $(100)$ orientated grains is to be increased.

Within this chapter the history of the aluminum-induced layer exchange process and its origins is extensively summarized. And an overview on the current work of several research groups is given. The embedding of this thesis within HMI is elucidated.

# 3 Experimental

This thesis is focussed on the investigation of the influence of the Al/a-Si interface and the annealing temperature on the layer exchange process. Therefore, it was part of this work to optimize the setup of an optical microscope with a heating stage in order to do in-situ investigations on the nucleation and growth in the ALILE process. In the first part of this chapter the sample preparation is described in detail. The second part of this chapter describes the setup of the in-situ optical microscopy, the evaluation methods of the obtained images, and additional characterization methods.

## 3.1 Sample preparation

The substrates and their cleaning procedure is described in section 3.1.1. All samples investigated within this thesis were deposited by DC magnetron sputtering. Both Al and a-Si for the ALILE process (as well as an additional Mo layer) were deposited in a four target sputtering tool (see section 3.1.2). The role of the Mo layer is described in section 4.1.2. The oxide interface layer was formed by different oxidation methods as described in section 3.1.3. The layer stacks have been annealed either within a furnace or the heating stage of an optical microscope (section 3.1.4). After the layer exchange the Al(+Si) top layer has to be removed in order to uncover the poly-Si layer. Chemical mechanical polishing was used to produce a smooth, epi-ready surface as described in section 3.1.5 [56]. The last step is of importance because the poly-Si layer is used as template for epitaxial thickening in order to form the absorber layer of the thin film solar cell.

### 3.1.1 Substrates

Corning glass 1737F substrates were used, which are Na free. The strain point of this glass lies at 666 °C. The glass substrates were cleaned by a reduced RCA cleaning, which is usually used for Si wafers. The glasses were initially cleaned in a $Piranha$ etch ($H_2SO_4 : H_2O_2 = 3 : 1$) at $T = 120$ °C for $20\,\mathrm{min}$ to remove organic contaminations. After rinsing in deionized (DI) water the samples were cleaned by a $Kern1$ etchant ($NH_4OH : H_2O_2 : H_2O = 1 : 4 : 20$) at $T = 70$ °C for $10\,\mathrm{min}$ to remove complex forming particles. Finally the samples were rinsed in DI-water again and dried.

Square $1'' \times 1''$ samples with a thickness of $0.7\,\mathrm{mm}$ and round $3''$ substrates with a thickness of $1.1\,\mathrm{mm}$ were used. The thin samples can be cut in small pieces easily and were mainly used for annealing in the optical microscope. However, only the large samples can be processed in the polisher. Thus, large samples were used for further epitaxy and cell processing.

### 3.1.2 Layer deposition

If not otherwise stated samples were deposited with following standard process parameters. The base pressure in the sputter chamber was $7.0 \cdot 10^{-7}\,\mathrm{mbar}$. Before igniting the plasma an argon working pressure of $6.5 \cdot 10^{-3}\,\mathrm{mbar}$ was adjusted. The sputter power was $500\,\mathrm{W}$. The deposition rates were $160\,\mathrm{nm/min}$ and $66\,\mathrm{nm/min}$ with layer thicknesses of $300\,\mathrm{nm}$ and $375\,\mathrm{nm}$ for Al and a-Si, respectively. All samples were deposited at room temperature.

### 3.1.3 Oxidation

The general difference between aluminum-induced crystallization (AIC) and the aluminum-induced layer exchange (ALILE) is the insertion of a permeable membrane between the initial Al and a-Si layers for the ALILE process. This membrane

does not participate in the layer exchange process and therefore remains in position throughout the annealing process separating top and bottom layer. A suitable membrane is aluminum oxide. Thus the initial aluminum layer needs to be oxidized prior to a-Si deposition in order to obtain continuous poly-Si films [54]. Al oxide layers are formed rapidly upon exposure to an oxygen containing atmosphere such as ambient air. Like in the case of silicon the oxidation of aluminum is self-limited meaning that the oxide layer prevents further oxidation. Thus upon reaching a certain oxide thickness, no further oxidation takes place. Whereas native silicon oxides reach thicknesses of $2 - 3\,\mathrm{nm}$ [86, 87], native aluminum oxides are in the range of $1 - 2\,\mathrm{nm}$.

Within this thesis very thin and very thick oxide layers have been used to test the limits of the interlayer influence. The investigation of the extreme cases allows to elucidate the role of the oxide layer. Usually the samples are oxidized by exposure to ambient air for $2\,\mathrm{h}$. Within this thesis additional oxidation methods were used: An argon/oxygen gas mixture ($40sccm/9sccm$) in the deposition chamber was used at low pressure ($6.5 \cdot 10^{-3}\,\mathrm{mbar}$) for $1\,\mathrm{min}$ to $120\,\mathrm{min}$ to form an ultra thin oxide layer. Thick oxide layers were formed by thermal oxidation in oxygen atmosphere in a furnace at $400\,°\mathrm{C}$ to $560\,°\mathrm{C}$ for $1.5\,\mathrm{h}$. Typically the transfer from deposition chamber to the oxidation furnace and back took a total of $30\,\mathrm{min}$. This lead to overall exposure time to oxygen atmosphere of $2\,\mathrm{h}$. The resulting oxide layer thicknesses are describe in section 4.1.

### 3.1.4 Annealing

Two different annealing methods were used, a furnace with $N_2$ atmosphere and a heating stage (Instec, Inc., HCS 601) installed at an optical microscope. The setup of this heating stage is schematically shown in Fig. 3.1. The samples are placed face down onto a heating block. The chamber is kept under a constant nitrogen flow of $20sccm$ in order to obtain an inert atmosphere to avoid atmospheric influence on the layer exchange process. The housing of the heating stage is water

cooled.

A large temperature gradient exists within the heating stage. The housing is at room temperature whereas the inside of the heating block reaches temperatures close to $600\,°C$. In order to determine the sample temperature a Pt100 thermal resistor was glued between two glass substrates with a two component ceramics glue. This stack was placed on the heater and the measurements of the internal platinum resistance temperature detector (RTD) $T_{set}$ was compared to the values obtained by the Pt100 $T_{real}$. The result for the temperature calibration is shown in Fig. 3.2. The linear fit is:

$$T_{real} = 0.854 \cdot T_{set} + 24.36\,°C. \tag{3.1}$$

It is expected that the temperature in the ALILE layer stack is not above the set

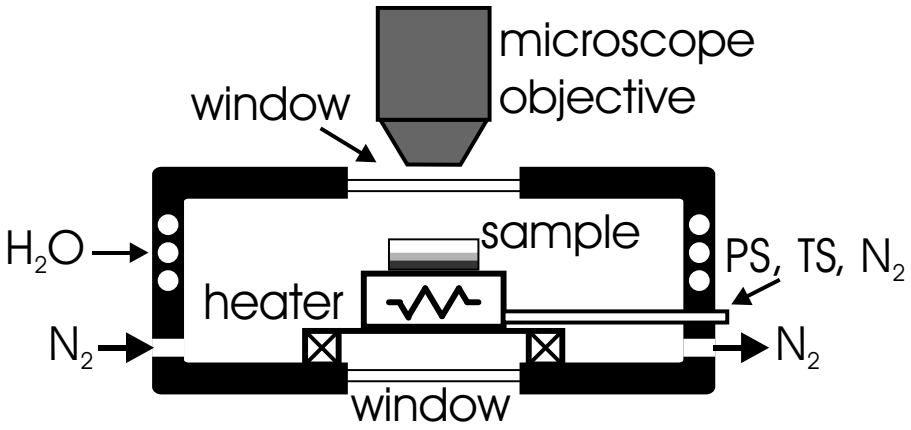


**Figure 3.1:** Scheme of the heating stage HCS 601 installed in the optical microscope. The housing is water-cooled and a constant nitrogen flow is supplied to the chamber in order to obtain a defined atmosphere. Usually the sample is placed face down on the heater. The heater is a silver block with a heating element, a thermo couple and nitrogen cooling tube inside. These are connected via an isolated tube to the power supply (PS), the temperature sensor (TS) and liquid or gaseous nitrogen supply. The sample can be observed in the optical microscope through a glass window. A window at the backside of the heating stage in combination with a central hole in the heater allows also to use the transmission mode of the microscope.

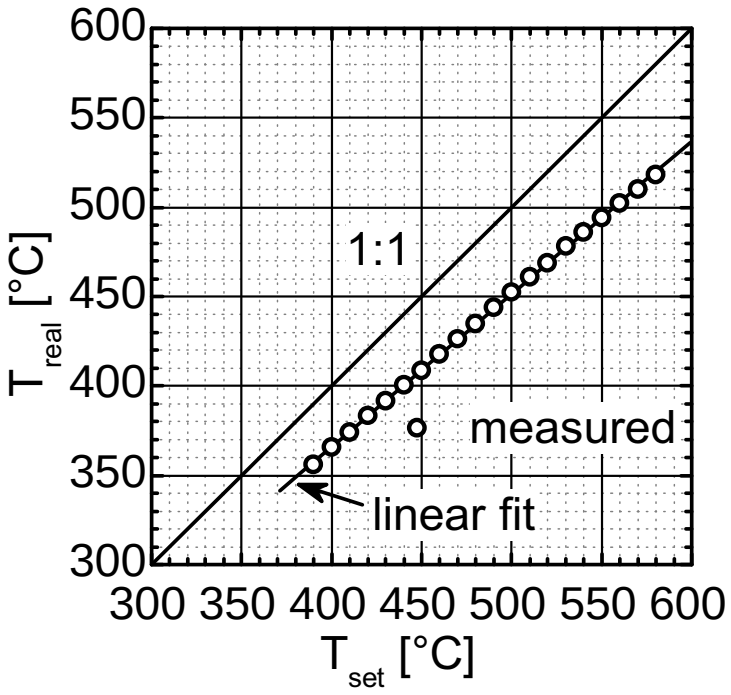


**Figure 3.2:** Temperature calibration: real temperature $T_{real}$ as a function of the set value $T_{set}$. (linear fit: $T_{real} = 0.854 \cdot T_{set} + 24.36\,°C$). As guide to the eye the $T_{real} : T_{set} = 1 : 1$ line is shown as well.

value $T_{set}$ and not below the real temperature $T_{real}$. The temperature values given within this thesis are the set values $T_{set}$.

The task of the temperature controller is to adjust the annealing temperature as fast as possible to the desired value without any overshooting. In Fig. 3.3 the resulting temperature profile is shown for heating from RT to $450\,°C$. Within $3\,\mathrm{min}$ the temperature difference is below $5\,°C$ and within $5\,\mathrm{min}$ the temperature difference is below $1\,°C$. The temperature stays stable within $\pm 0.5\,\mathrm{K}$ of the set temperature.

### 3.1.5 Chemical Mechanical Polishing

The top Al(+Si) layer has to be removed for certain characterization methods and the subsequent epitaxial thickening. As suggested earlier [56] this can be done by chemical mechanical polishing (CMP). In the CMP process the wafer is put into a

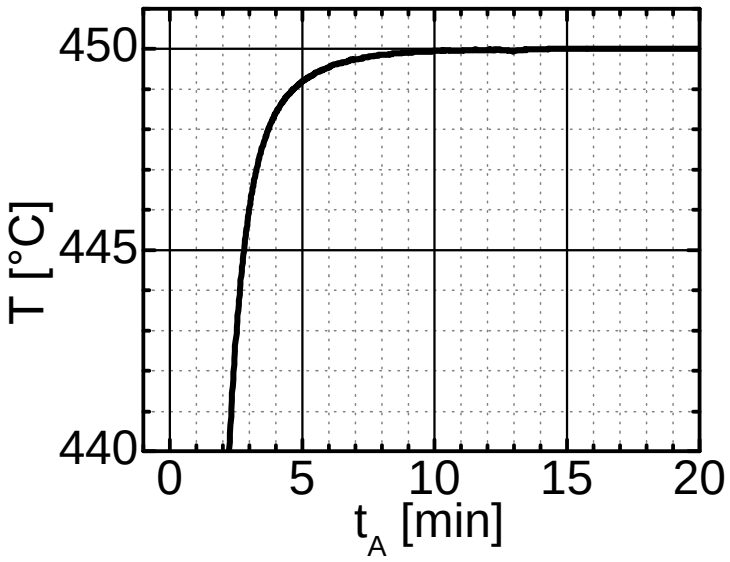


**Figure 3.3:** Temperature $T_{set}$ versus annealing time $t_A$ when the temperature is at RT and set to $450\,$°C at $0\,\mathrm{min}$. Within $3\,\mathrm{min}$ and $5\,\mathrm{min}$ the temperature is within $5\,\mathrm{K}$ and $1\,\mathrm{K}$ of the desired temperature, respectively.

carrier head which is pressed onto a pad covering the main plate. Both carrier and main plate rotate while a defined amount of slurry is poured onto the pad. The slurry is a liquid including colloidal particles. Between sample and pad a small film of slurry is formed. While the chemical component modifies the surface at a homogeneous depth the combined mechanical polishing effect of colloids and pad take of the most protruding parts. This combined effect results in a very smooth surface.

A Logitech CDP machine and a silicic acid based slurry (Syton) were used for polishing the samples. The standard parameters for the main plate and carrier rotation velocities, the download pressure on the sample and the flow of slurry are shown in table 3.1. Even though standard parameters are provided the polishing process has to be adjusted for every polished sample individually by checking the result during polishing. The polishing process takes about $2\,\mathrm{min}$ and has been optimized within our group.

| main plate | carrier | download pressure | slurry |
|---|---|---|---|
| 60rpm | 40rpm | 0.5 .. 0.7mbar | 50 mL/ min |

**Table 3.1:** Main CMP parameters

## 3.2 In-situ optical microscopy

For in-situ characterization the samples were annealed in the optical microscope. The evaluation of the obtained results is described in detail in the following.

For in-situ investigation of the layer exchange process a Leitz DMRX optical microscope was used. The microscope has been equipped with a heating stage (see Fig. 3.1) and a digital camera (Sony DXC-151P CCD/RGB). The entire setup of the in-situ optical microscope is shown in Fig. 3.4. The camera image can be observed live at a monitor. The heating stage is powered by a power supply and operated by a PID temperature controller (see section 3.1.4). The controller is set via a Labview programm on the computer. Images were recorded using the program 'supervision cam' within typical time intervals of $10\,\mathrm{s}$ to $5\,\mathrm{min}$ depending on the process parameters. The spatial resolution limit of the setup is about $0.5\,\mu\mathrm{m}$.

The samples were put upside down onto the heating block. Thus the initial glass/Al interface is observed during the annealing through the glass substrate. Due to the high reflectivity of the Al the micrographs appear bright at the beginning of the process. As soon as the size of the Si grains exceeds the resolution limit of the microscope the crystallized Si becomes visible as small dark spots at the glass/Al interface due to the lower reflectivity of Si compared with Al. These dots grow further and finally form a continuous poly-Si film. Then the image appears completely dark. Fig. 3.5(a) shows an optical micrograph of a samples after $21.5\,\mathrm{min}$ annealing. The silicon covers $50\,\%$ of the micrograph area. Dark silicon grains have appeared. Fig. 3.5(b) shows the corresponding crystallized fraction $R_C$ curve. The definition and determination of the $R_C$ value is described in the next paragraph. The dot marks the image in (a).

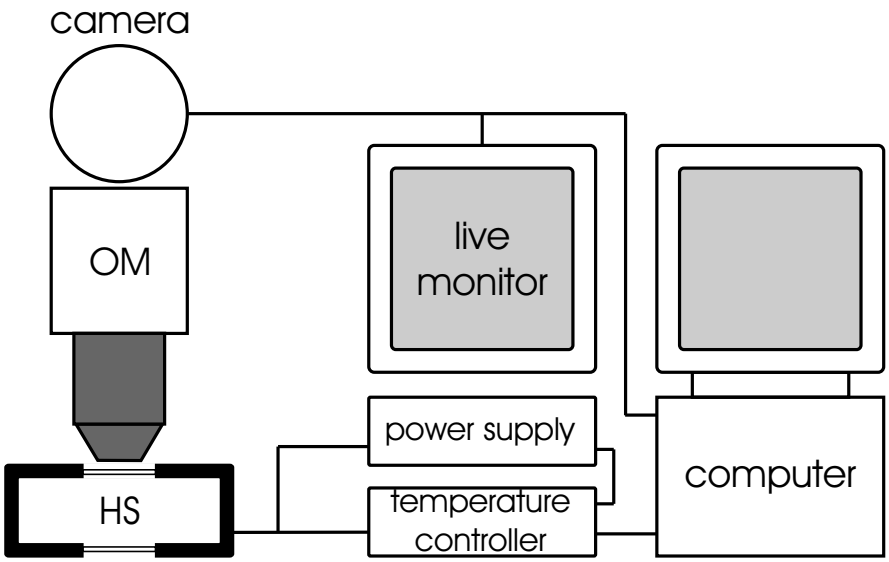


**Figure 3.4:** Setup for in-situ microscopy. The sample in the heating stage (HS) (see Fig. 3.1) is observed in the optical microscope (OM). A CCD camera on the microscope is connected to a live monitor and a PC. The temperature controller operates a power supply to adjust the annealing temperature. The computer uses a Labview program to set the temperature profiles in the controller.

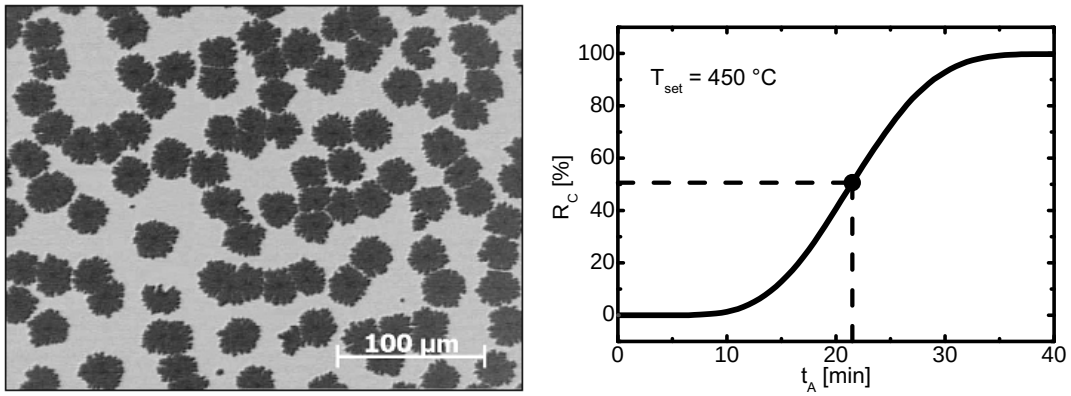


(a) (b)

**Figure 3.5:** (a) Optical micrograph of a sample after $21.5\,\mathrm{min}$ annealing at $T_{set} = 450\,°\mathrm{C}$. The growing silicon grains are dark within the bright Al matrix. (b) Corresponding crystallized fraction curve $R_C$. $R_C$ starts at $0\,\%$ when no silicon is present in the aluminum and reaches $100\,\%$ when the layer exchange is completed. The spot represents the case of the micrograph in (a).

Before the annealing a 'blanc' image is acquired of the glass/Al interface as a reference for the CCD camera. The images are evaluated using image processing techniques of the program 'Image Tool'. 'Image Tool' scripts were used to automate image analysis. First, the color micrographs are converted to 8bit greyscale. Second, the 'blanc' image is subtracted from each image in order to remove effects from illumination non-uniformity and difference in brightness of images of different series. Thus the compatibility of the images of different series can be guaranteed. The threshold can be set to 170 out of 256 greyscale tones for all series. All pixels brighter than this margin are evaluated to be white (Al) and all darker pixels to be black (Si). The black fraction of the images is determined and used as crystallized fraction $R_C$. The crystallized fraction curves are evaluated as function of the annealing time $t_A$. $R_C$ is $0\,\%$ at the beginning of the process and corresponds to all Al at the interface. The first time spots area detect is defined as the nucleation time $t_N$. As soon as $R_C$ reaches $100\,\%$ the entire glass surface is covered with poly-Si. The process time $t_P$ is defined as the time required to reach $R_C = 95\,\%$.

Counting the number of black objects $n$ in the black and white image of area $A_0$ determines the nucleation density $N_G$ in each image ($N_G = \frac{n}{A_0}$). In Fig. 3.6 the nucleation density $N_G$ is shown as a function of the annealing time $t_A$ for a specimen with a thermal oxide interface formed at $500\,$°C for $1.5\,\mathrm{h}$ annealed at $T_A = 450\,$°C. Nucleation starts after $t_A = 15\,\mathrm{min}$ and increases rapidly until after about $30\,\mathrm{min}$ nucleation is strongly slowed down. The maximum nucleation density is reached after $t_A = 65\,\mathrm{min}$. The nucleation density detected in the images decreases again, because neighboring grains coalesce and are not distinguished anymore. The maximum of the nucleation density was used to evaluate the final estimated grain size $d_G$ of grains assumed to be squared ($d_G = \sqrt{\frac{1}{N_G}}$). The estimated grain size includes several assumptions: (i) the maximum number of grains is detected when no new grains are formed, (ii) at this point no grains have collided, i.e. all grains are separate and counted, (iii) all grains are averaged in size, (iv) a square shape of the grains is assumed, (v) the areas grown from one nucleus are a grain, i.e.

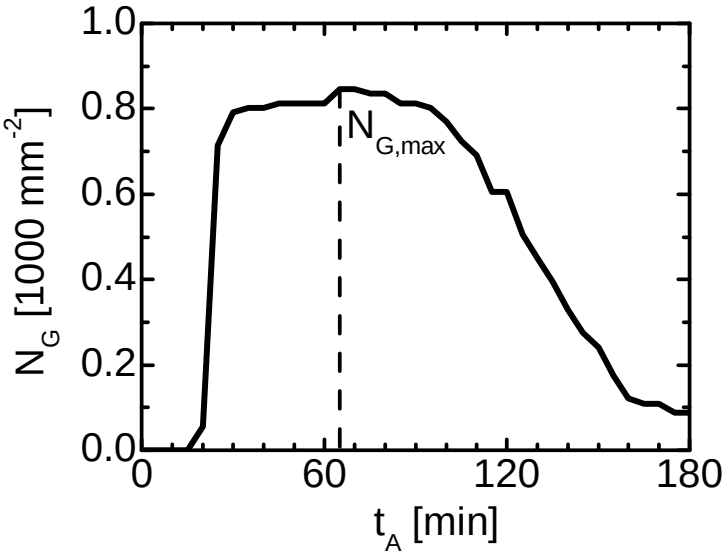


**Figure 3.6:** Nucleation density $N_G$ versus annealing time $t_A$ for a specimen with a thermal oxide formed at $500\,$°C for $1.5\,\mathrm{h}$ annealed at $T_A = 450\,$°C.

monocrystalline.

## 3.3 Electron Back Scatter Diffraction

Crystallographic analysis was done by Electron Back Scatter Diffraction (EBSD). A nice overview on EBSD is given in [88].

EBSD uses the elctron beam from a scanning electron microscope and detects the back scattered electrons with a phosphor screen or CCD camera. The incident angle of the electron beam is low, about $20°$ with respect to the sample surface. Thus the penetration depth of the electrons is decreased and the fraction of back scattered electrons from the sample is increased. The elastic scattering of the electrons is either (i) a coulomb interaction with a nucleus or (ii) an interaction with the electron gas. As a result electrons are scatter in all direction almost homogeneously. Due to the elastic scattering the electrons do not lose energy. Thus the electron propagate in all direction of the sample with the same energy. Electron diffraction in the excited volume increases the number of electrons fulfilling Bragg's condition:

$$n\lambda = 2\,d\,\sin\Theta \tag{3.2}$$

where $n$ is an integer (order of diffraction), $\lambda$ is the wave length of the electron beam, $d$ the lattice spacing and $\Theta$ is the diffraction angle. The incident electrons interact with a small volume of some cubic nanometers. With the detection screen being some centimeters away the detection volume can be assumed to be one point. Due to the homogeneous distribution of all electron propagation directions in the sample the diffracted electrons exhibit a rotational symmetry around the normal to the respective lattice planes fulfilling Bragg's condition. Thus the diffracted electrons show a maximum in two cones symmetric to the lattice planes in forward and backward direction. When these two cones intersect with the plane detection screen a double line is formed. These lines are referred to as Kikuchi lines. Their distance is inversely proportional to the lattice spacing $d$. The sum of all Kikuchi lines is called Kikuchi pattern. It is characteristic for the lattice type and spacing and thus allows the identification of both the investigated material and the crystal orientation. Since the samples investigated here are all Si, EBSD is used to determine the samples' crystal orientation.

# 4 Results

In order to understand and optimize the aluminum-induced layer exchange process (ALILE) two main process parameters were modified. The role of an interlayer between aluminum and silicon was intensely studied (sec. 4.1). Therefor different types of oxidation conditions were tested. The thickness of the oxide layer was varied in a wide range from just about $1\,\mathrm{nm}$ to several $10\,\mathrm{nm}$. On the one hand thick oxide layers and high annealing temperatures leads to large grain sizes in short process times. On the other hand thin oxide layers and low annealing temperatures enhances the formation of $(100)$ orientated grains. Molybdenum as an alternative interlayer was investigated. It is shown that molybdenum interlayers enable the layer exchange process as well. They even facilitate the lift-off process of the silicon islands.

In a thermal annealing process the process temperature is a crucial parameter. So far only isothermal annealing experiments have been reported in the ALILE process. Here the influence of different temperature profiles was studied (sec. 4.2). Experiments on increasing and decreasing the temperature during annealing were performed. The heating step experiments show that after a certain point in the annealing process the temperature can be increased without causing additional nucleation but resulting in shorter process time. This reinforces the existence of depletion regions around the growing grains. Once the depletion regions overlap the temperature can be increased. The depletion regions become apparent in cooling step experiments where additional nucleation is caused by supercooling. Zones without additional nucleation around existing grains are direct experimental proof of the existence of concentration profiles, namely the depletion regions.

## 4.1 Interlayer

It was shown that an aluminum oxide interlayer between the initial Al and a-Si is needed in the aluminum-induced layer exchange process [54]. The interlayer controls the velocity of the crystallization process and the nucleation density. Both, oxidation of the aluminum layer as well as the oxidation of the amorphous silicon layer in an inverse layer structure were shown to lead to a layer exchange. Still many questions concerning the interlayer need to be answered.

Two fundamental questions arise regarding the role of the interface layer. 'What happens without an interface layer?' and 'Why is an oxide layer needed?'. In order to answer the first question a sample was prepared without an interlayer, i.e. the a-Si was deposited directly onto the Al. Additionally a sample with oxide interface was prepared. The samples were annealed at $480\,°\text{C}$ for $45\,\text{min}$ and the Al was etched off wet chemically. SEM images without (a) and with (b) oxide layer are shown in Fig. 4.1. The samples were tilted by $30°$. At the bottom of the micrographs is the glass substrate covered with silicon. In both cases the glass is covered with large compact Si islands. The sample without oxide layer shows a porous silicon structure. Through holes in the porous structure the glass substrate is visible. No continuous film is obtained. With oxide layer a continuous Si film covers the glass beneath the islands. Thus, the use of an oxide layer leads to the formation of a continuous layer. This continuous Si layer is used as substrate for the subsequent epitaxy.

TEM investigations were made in order to determine the influence of the annealing process on the oxide layer. In Fig. 4.2 a TEM cross section of a sample after annealing is shown. The glass is covered by a continuous silicon layer. The top layer consist of Al with silicon islands. The presented section shows mostly silicon islands. However, top and bottom layers are clearly separated. In the inset the color-coded superposition of three electron energy loss spectroscopy (EELS) elemental maps is shown. Here, red corresponds to Al, blue to O and green to Si. Even after the layer exchange process the oxide layer is still at the interface

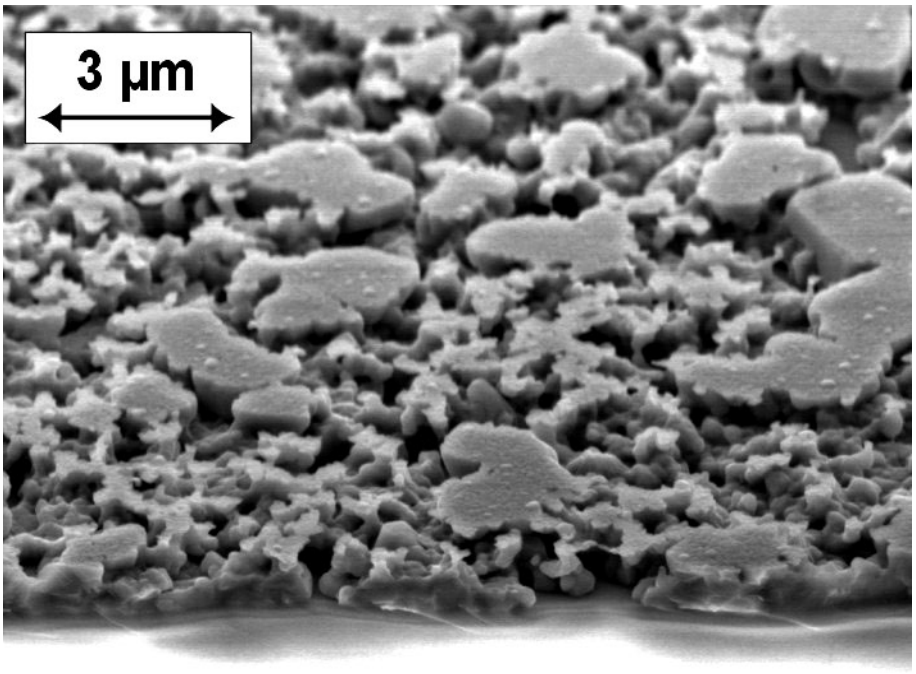


(a)

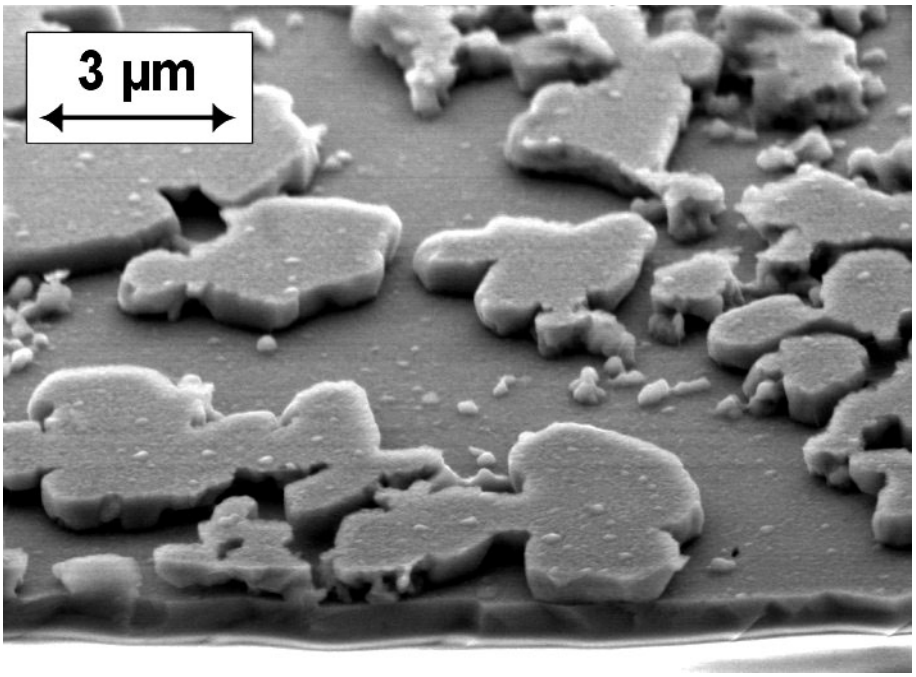


(b)

**Figure 4.1:** SEM micrographs of the crystallized Silicon after annealing and wet chemical removal of the Al without (a) and with (b) oxide interlayer [89]. In (a) a porous crystalline Si structure is formed. In (b) the glass substrate is covered with a continuous poly-Si film. On top of the film are Si islands which are crystalline as well.

between the c-Si seed layer (bottom) and the Al matrix with Si islands (top). In the inset almost no Al can be seen. But clearly the oxide interface between the si grain in the bottom layer and the Si island in the top layer is continuous even after the layer exchange. These results imply several conclusions. In order to remain at the same position without relocation the oxide layer must be permeable for both Al and Si. The silicon grains formed within the Al layer cannot grow across the oxide interface, they remain confined within the Al layer between oxide layer and glass. This leads to lateral growth and resulting continuous, smooth poly-Si layers. The thicknesses of the resulting c-Si and Al(+Si) layer are thus determined by the thicknesses of the initial Al and a-Si layers, respectively. Separation of top and bottom layer throughout the process is one of the task of the interlayer.

In order to answer the second question, why an oxide layer is needed and to get a more detailed insight into the role of the interlayer, the oxide layer was varied by changing the thickness and preparation method (sec. 4.1.1). Alternatively a thin molybdenum layer was used as interface layer. This is described in sec. 4.1.2.

### 4.1.1 Oxide interlayer

Three different types of oxide interlayer were prepared by varying the oxidation conditions of the Al surface:

- Type A: **Thin oxide** formed by oxidizing the Al surface in the deposition chamber by exposure to a gas mixture of $[Ar]\,/\,[O_2] = 40sccm/10sccm$ at $6.5 \cdot 10^{-3}\,\mathrm{mbar}$ for $60\,\mathrm{min}$ at room temperature.

- Type B: **Standard oxide** formed by exposure to air for $20\,\mathrm{h}$ at room temperature.

- Type C: **Thick oxide** formed by thermal oxidation of the Al surface in a furnace at $560\,°\mathrm{C}$ in oxygen atmosphere for $2\,\mathrm{h}$.

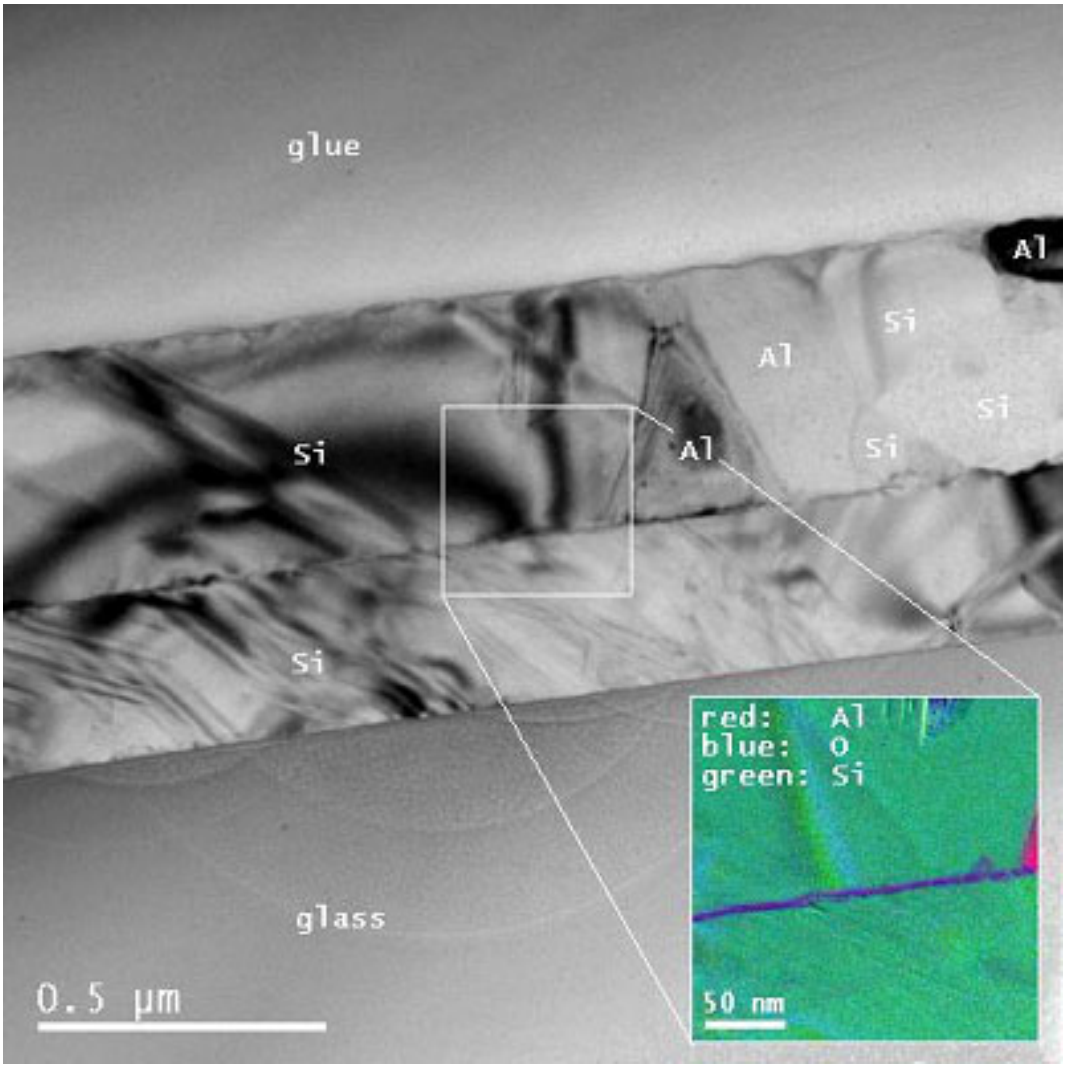


**Figure 4.2:** TEM cross section of a layer stack after annealing. On the glass substrate are the poly-crystalline Si seed layer and on top of it is the Al(+Si) layer. In this portion of the Al(+Si) layer mostly crystalline Si islands are found. In the inset a color coded EELS elemental map is shown. The oxide layer (blue) remains in position throughout the layer exchange process.

To investigate the influence on the incorporated amount of oxygen the different sample types were analyzed by Auger electron spectroscopy (AES) depth profiling. Fig. 4.3 shows AES counts for oxygen as a function of the sputter cycles for samples of type A, B and C [1]. The a-Si layer is on the left side, the Al layer on the right side and the oxide layer in between as indicated at the top of the graph. Whereas samples of type A and B show a narrow oxygen peak at the interface indicating that the oxide layer is quite thin, sample C exhibits a broad oxygen signal indicating that the aluminium oxide layer stretches over several AES sputter cycles significantly into the Al-layer. Additionally the maximum number of oxygen counts increases for sample C. Note that the sputter cones obtained during the AES depth profiling lead to a broadening of the signal. The AES measurement is surface sensitive. If the surface is bend the analysis is integrated over a certain thickness of the film. Only the oxide in specimen type C is thicker than the curvature of the sputter cone. Thus the number of counts is higher and the maximum extends across several cycles. TEM investigations showed that the oxide layer thickness for the samples was increased from $4\,\mathrm{nm}$ to above $30\,\mathrm{nm}$ for samples of type A and C, respectively. While no TEM investigations were made on sample type B it is estimated from TEM results of other interlayers and the AES results in Fig.4.3 that it should be about double the thickness of the interlayer of sample type A. Thus the amount of oxygen at the interface was successfully altered by varying the oxidation conditions.

The influence of the different oxide layers on the layer exchange process was studied using the in-situ microscope setup. The samples were placed face down in the heating stage to enable the observation of the glass/Al-interface through the glass substrate. Two micrographs are shown in Fig. 4.4 recorded for samples of type A (Fig. 4.4b) and C (Fig. 4.4a) at a crystallized fraction $R_C = 40\,\%$ (defined in section 3.2) after $35\,\mathrm{min}$ and $29.5\,\mathrm{h}$ annealing at $450\,°\mathrm{C}$, respectively. The silicon areas appear as dark round shapes in the bright aluminum matrix. For sample type A the nucleation density is much higher ($N_{G,A} = 3460\,\mathrm{mm}^{-2}$) than for sample type

[1] The zero sputter cycles were set at the onset of the oxide layer

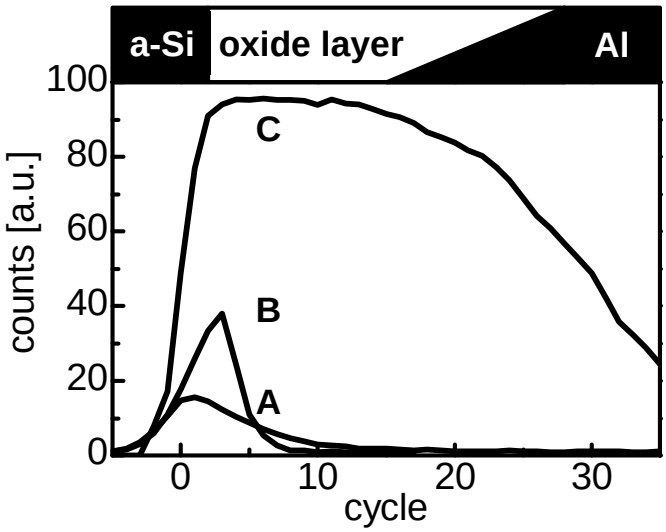


**Figure 4.3:** Auger depth profile of oxygen at the a-Si/Al-interface after deposition. The number of counts vs. the sputter cycles is shown. The corresponding layers are shown at the top of the graph. Samples of type A, B and C were measured. An increase in the oxygen content at the interface could be confirmed.

C ($N_{G,C} = 44\,\mathrm{mm}^{-2}$ [2]). For sample type C the grains grow dendritic and some Al inclusions are visible in the growing grains. These inclusions should be avoided, because continuous poly-Si layer are desired for epitaxial thickening. Still the large difference in nucleation density demonstrates one of the most striking observations in the ALILE process. In Fig. 4.4b large areas $> 100 \times 100\,\mu\mathrm{m}^{-2}$) without any nuclei are visible. In these areas no new grains appear throughout the entire process. The nucleation of the first grain suppressed nucleation of further grains in a self-limiting process. The phenomenon of self-limited nucleation suppression can stretch over several $100\,\mu\mathrm{m}$. The oxide layer controls the flux of silicon from the amorphous Si phase into the Al. If this flux is inhibited by a thick interlayer less silicon is available in the Al layer and the nucleation rate is lower. Additionally this increases the process time strongly. Sample type C in Fig. 4.4b had to be annealed for $29.5\,\mathrm{h}$. The origin of the nucleation suppression is discussed in detail in the chapter 5.

[2] This number is derived from a larger image not shown here

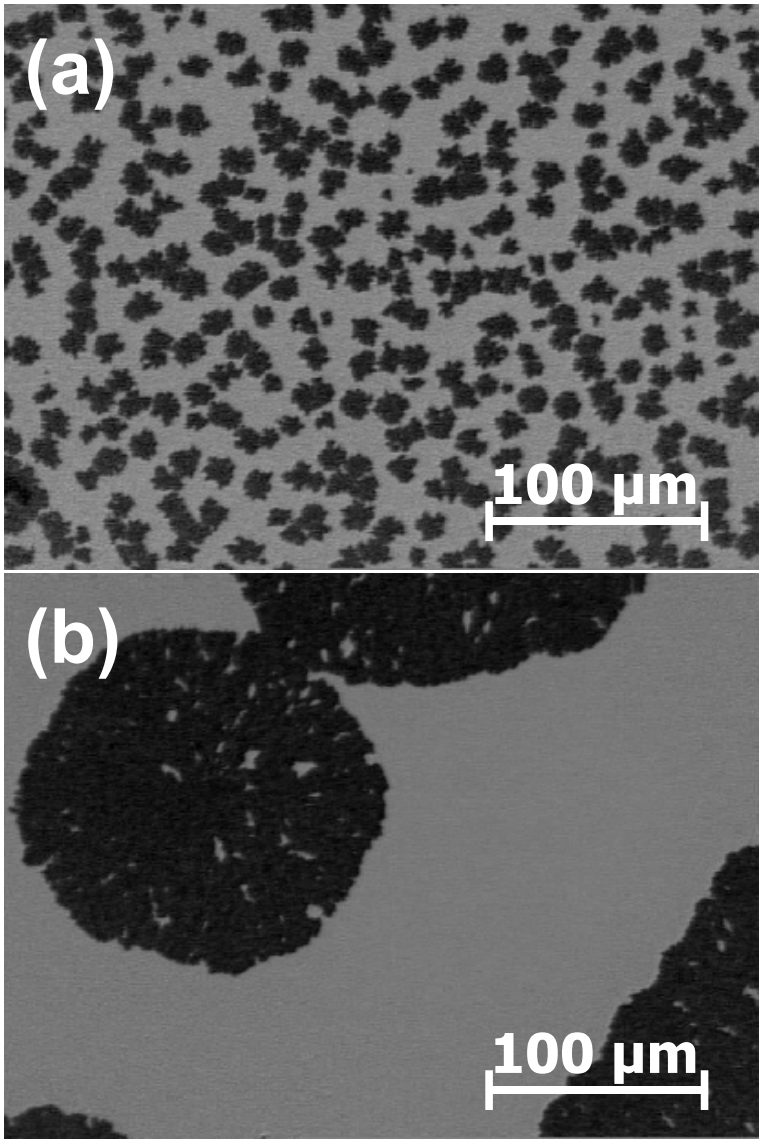


**Figure 4.4:** Optical micrograph of sample type (a) A (thin oxide) and (b) C (thick oxide) annealed at $450\,$°C at a crystallized fraction $R_C = 40\,\%$ after $35\,\mathrm{min}$ and $29.5\,\mathrm{h}$, respectively. The images are taken looking through the glass at the initial glass/Al-interface. The dark circles correspond to the silicon growth areas while the bright area is the aluminium. The nucleation density in (b) is much lower than in (a). In (b) several Al inclusions in the growing grains can be observed. These have to be avoided.

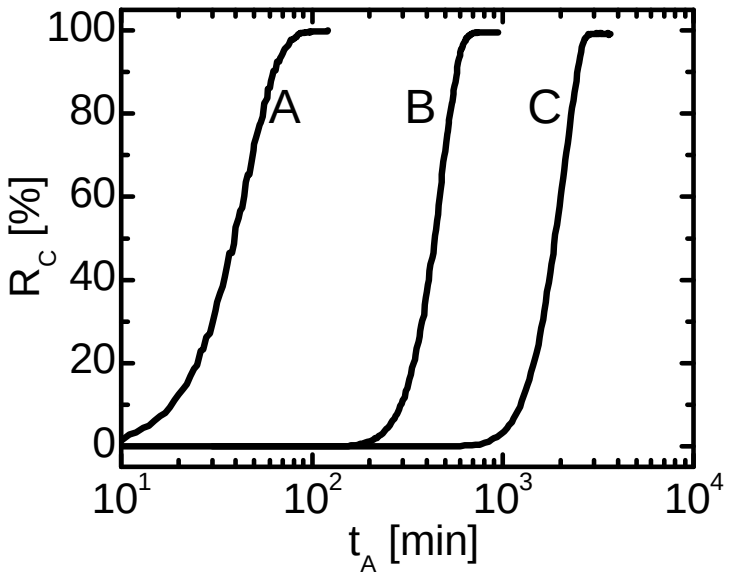


**Figure 4.5:** Crystallized fraction $R_C$ versus annealing time $t_A$ for samples of type A, B and C annealed at $450\,°\mathrm{C}$. While the layer exchange for sample A was completed in less than $2\,\mathrm{h}$ it took about $2d$ for sample type C.

Fig. 4.5 shows the crystallized fraction $R_C$ as a function of the annealing time for samples A, B and C at $450\,°\mathrm{C}$. Annealing of sample A took less than two hours while the layer exchange for sample C took several days. The $R_C$ reaches $100\,\%$ for all types of oxide, i.e. all samples formed a continuous silicon layer[3]. Even for the very thick oxide (sample C) the layer exchange took place. Thus, the thicker the oxide, the lower the nucleation rate and the higher the process time $t_P$ needed to complete the process.

The process time $t_P$ is defined as the annealing time needed to reach a crystallized fraction $R_C$ of $95\,\%$, $t_P = t_A\,(R_C = 95\,\%)$. The process time $t_p$ (solid circles) and estimated grain size $d_G$ (open circles) for the three samples annealed at $450\,°\mathrm{C}$ are shown in Fig. 4.6. Thicker oxides lead to higher process times and larger estimated grain sizes. Note the enormously large estimated grain size of above $100\,\mu\mathrm{m}$ of the thermally oxidized sample (as already visible in Fig. 4.4b). This is the largest, published estimated grain size achieved with the ALILE process so far. However,

[3]the Al inclusion in Fig. 4.4b are to small at the end in order to contribute to a significant reduction of $R_C$ for sample type C

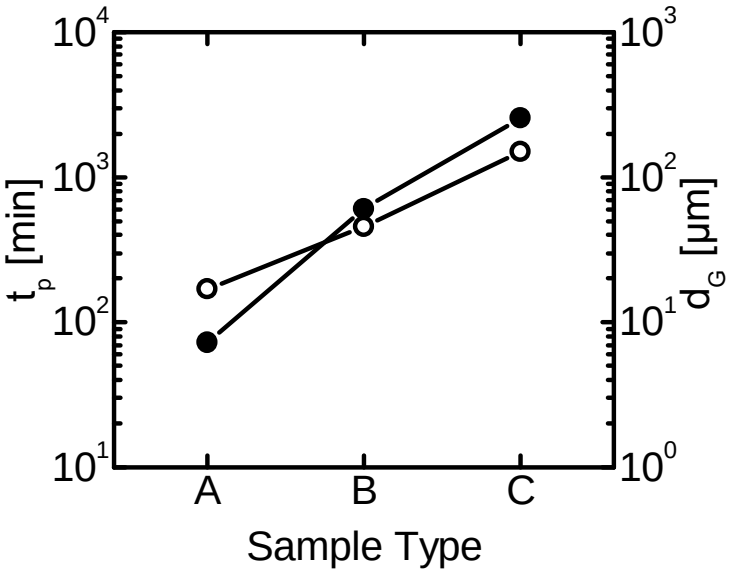


**Figure 4.6:** Process time $t_p$ (solid circles) and estimated grain size $d_G$ (open circles) for samples A, B and C annealed at $450\,$°C. Sample A: thin oxide. Sample B: standard oxide. Sample C: thick oxide. The lines in the graph are guides to the eye.

the process times to reach these large estimated grain sizes are very high, up to several days. For technological applications a compromise between grain size and process time in short process times has to be made.

Both parameters - process time and estimated grain size - are a function of the annealing temperature as well. Fig. 4.7 shows process time $t_p$ and estimated grain size $d_G$ as a function of the annealing temperature $t_A$ for a sample of type B. The sample was annealed at $450\,$°C, $480\,$°C and $500\,$°C. While the process time varies strongly by about an order of magnitude (from $43\,\mathrm{min}$ at $500\,$°C to $605\,\mathrm{min}$ at $450\,$°C), the estimated grain size is only doubled (from $15\,\mu\mathrm{m}$ to $37\,\mu\mathrm{m}$).

In order to compare the influence of annealing temperature and type of oxide layer, samples of type B and C were annealed at higher temperatures to reduce the process times. The annealing temperatures were increased until the process time for all samples was below $< 2\,\mathrm{h}$. Sample A was annealed at $450\,$°C as in Fig. 4.8. Sample type B was annealed at $480\,$°C. Raising the annealing temperature by $30\,$°C reduced the process time by almost an order of magnitude. Sample C had to be annealed at $540\,$°C - i.e. $90\,$°C higher than sample A - to reduce the process

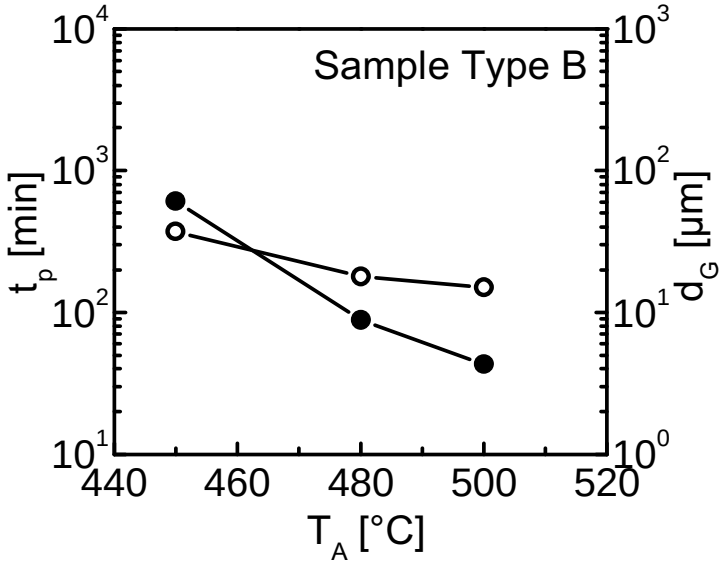


**Figure 4.7:** Process time $t_p$ (solid circles) and estimated grain size $d_G$ (open circles) vs. annealing temperature $T_A$ for sample type B (standard oxide).

time to about $2\,\mathrm{h}$. The estimated grain sizes $d_G$ were smaller for samples B and C compared to the case of annealing at $450\,°\mathrm{C}$ (Fig. 4.6). Still a strong increase in the estimated grain size $d_G$ for the sample of type C was found compared to sample type A and B even at higher annealing temperature. The difference in $d_G$ from sample A and C is about one order of magnitude at similar process time, the estimated grain size for sample C is $150\,\mu\mathrm{m}$, for sample of type A it is just about $17\,\mu\mathrm{m}$.

Thus, it is concluded that the process time $t_p$ is dominated by the annealing temperature $T_A$ whereas the oxide layer thickness $d_{ox}$ determines mainly the estimated grain size $d_G$. Thus a second task of the interlayer is the control of the nucleation density $N_G$ and as a consequence the estimated grain size $d_G$. For a detailed discussion of these result see chapter 5.4.

After demonstrating the influence of the interlayer on the nucleation density, the influence on the grain growth is investigated. Analyzing the growth of a single grain the radius growth velocity was studied. This quantity may be taken as a measure of the grain growth. In Fig. 4.9 shows the development of the radius of a single grain $r_G\,(t)$ analyzed during annealing of a specimen of type C at $T_A = 400\,°\mathrm{C}$.

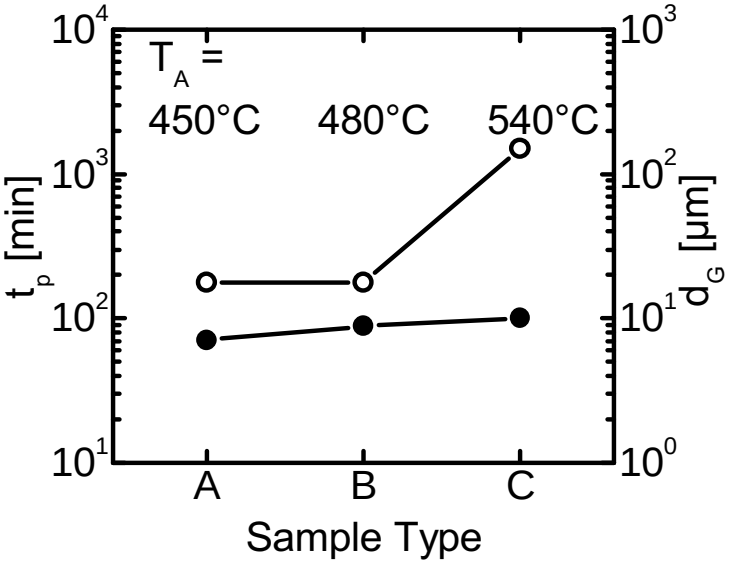


**Figure 4.8:** Adjustment of the process time $t_p$ (solid circles) to below 2 h for the three differently oxidized samples by raising the annealing temperature $T_A$ from 450 °C to 480 °C for sample B and to 540 °C for sample C. The estimated grain size $d_G$ (open circles) is still increasing strongly from sample B to C with increasing oxide thickness. The lines in the graph are guides to the eye.

Here the nucleation time $t_N$ is defined by the time when the grain becomes visible in the optical microscope. The radius growth velocity $v_G = dr_G/dt_A$ increases at the beginning until a final, constant grain growth velocity $v_{G,0}$ is obtained. The slowest annealing process (thick oxide and low annealing temperature) was chosen to define $t_N$ and $v_{G,0}$ because here the steady increase in the grain growth velocity before reaching a constant $v_{G,0}$ can most easily be demonstrated. [4] The linear growth of the radius means that the area of the grain grows as ${t_A}^2$. This finding is quite striking because it means that during the process more and more Si is incorporated into the growing surface.

The grain radius $r_G$ versus annealing time $t_A$ for the different sample types is shown in Fig. 4.10. Several grains for each specimen were evaluated and the final grain growth velocity $v_{G,0}$ was determined by a linear fit to the $r_G$ curves and

[4] The noise in the curve is caused by small movements of the image and variations in image brightness during the annealing.

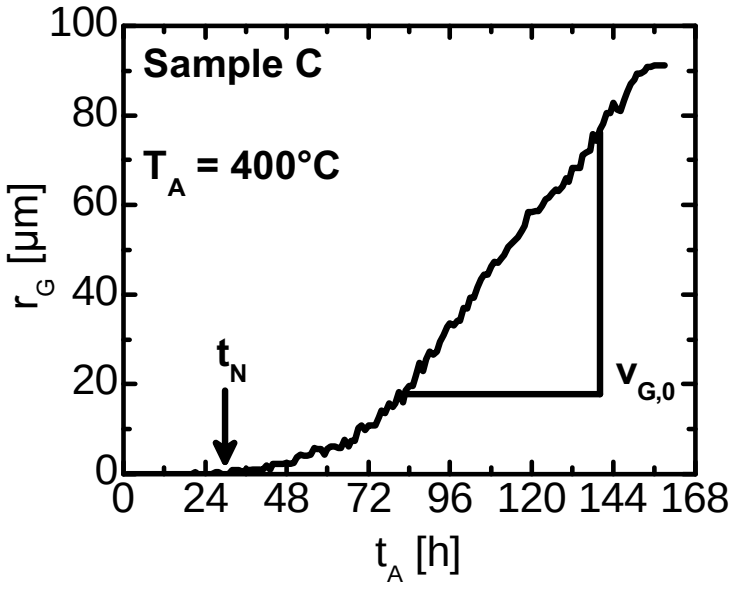


**Figure 4.9:** The radius of a single grain $r_G$ as a function of the annealing time $t_A$ for a specimen type C annealed at $T_A = 400\,°\text{C}$. The grain becomes visible at the nucleation time $t_N$. The grain growth velocity increases until the final, constant grain growth velocity $v_{G,0}$ is obtained.

by calculating the average value. The grain growth velocity for specimen A is $0.227 \pm 0.028\,\mu\text{m/min}$. For both the other specimens the grain growth velocity was found to be approximately equal at $0.077 \pm 0.006\,\mu\text{m/min}$ and $0.076 \pm 0.001\,\mu\text{m/min}$ for samples type B and C, respectively. The grain growth velocity is similar for all grains in the same experiment. All grains in the same experiment nucleate at approximately the same time.

In Fig. 4.11 the density of grains $N_G$ is shown as a function of the annealing time for a specimen of type C annealed at $450\,°\text{C}$. The density of grains is very low at the end of the process indicating the very large grain size. Three different phases of the process are marked. In phase (I) no grains are visible. In phase (II) nucleation takes place and these grains grow, thus this phase is referred to as *nucleation phase*. After a certain time the nucleation comes to an end. The existing grains continue to grow until the layer exchange is completed. This phase (III) is referred to as *growth phase*. The process time in case of the sample in Fig. 4.11 is about $43\,\text{h}$ (Fig. 4.6). Depending on the process parameters the phases have

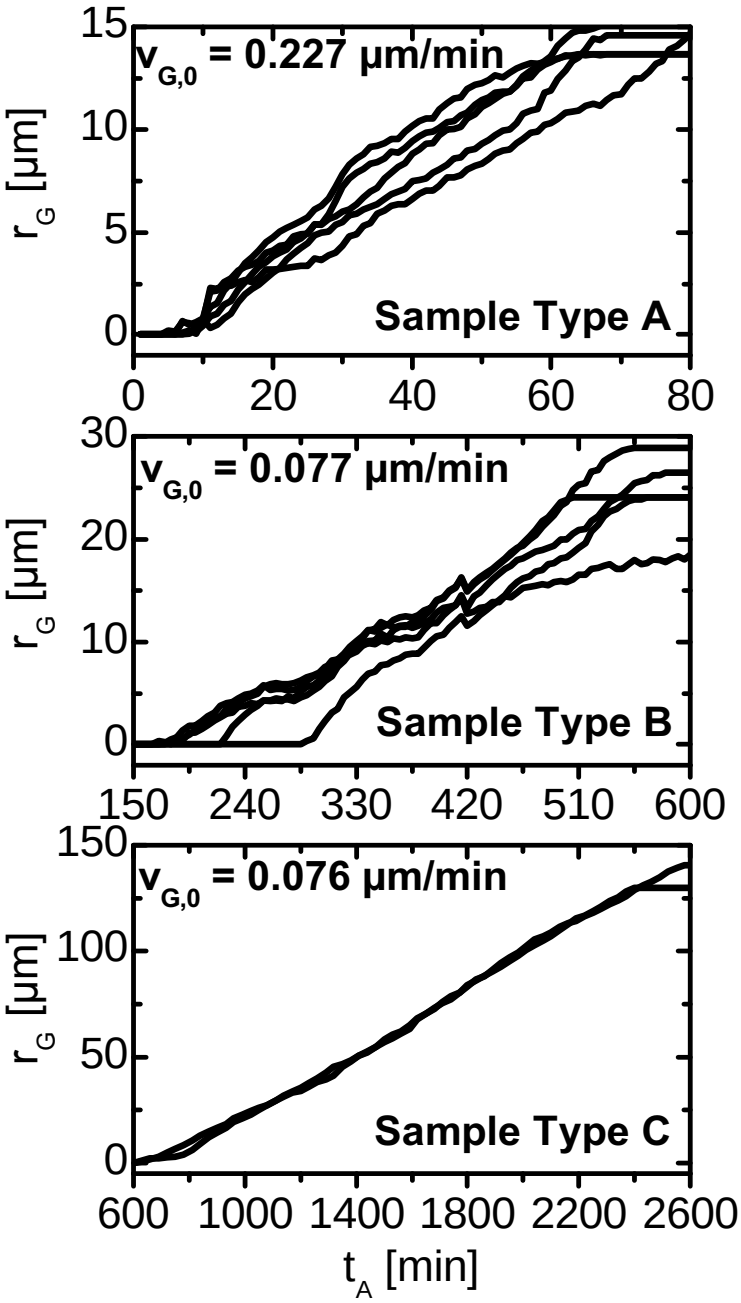


**Figure 4.10:** Radius $r_G$ of several grains in the same experiments as a function of the annealing time $t_A$ for specimen A, B and C annealed at $450\,°C$. For sample type A the average final grain growth velocity $v_{G,0}$ is faster than for the two other specimen.

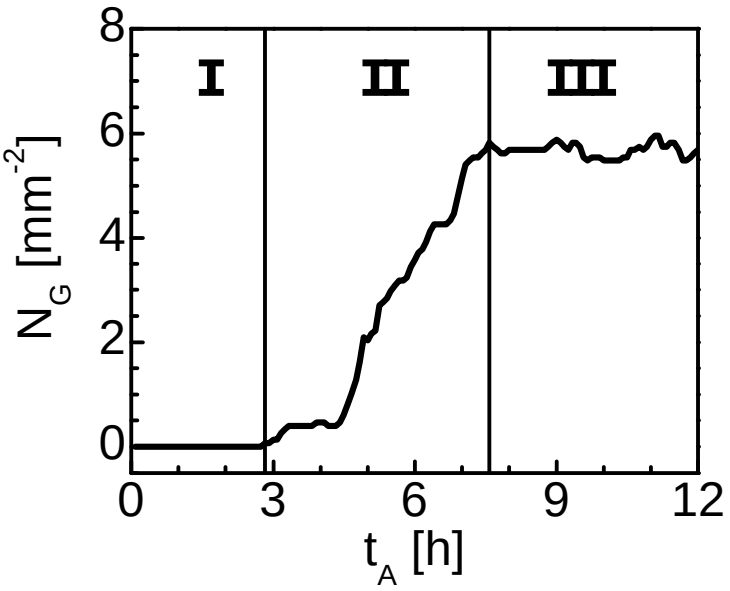


**Figure 4.11:** Density of grains $N_G$ as a function of the annealing time $t_A$ for a specimen type C annealed at $450\,°\mathrm{C}$. Three characteristic phases of the process are marked. In phase (I) no nuclei are formed. In the nucleation phase (II) more and more silicon grains become visible. In the growth phase (III) nucleation is suppressed and the layer exchange is continued by growth of the existing grains only. The process time is $t_P = 43\,\mathrm{h}$

different durations. Sometimes all grains appear basically at the same moment, i.e. within one or two micrographs in a time period short as compared to the process time. This is the case when thick oxide interfaces (type C) are used. In Fig. 4.11 the nucleation phase last about $4\,\mathrm{h}$ which is short compared to a process time $t_P = 43\,\mathrm{h}$. However there are also other cases were the new grains are formed almost throughout the entire process and the growth phase (III) is short.

The self limited nucleation suppression is one of the characteristic features of the ALILE process. Due to the low nucleation density large grain sizes are obtained in the ALILE process. The mechanism responsible for the self-limitation of the nucleation is discussed in detail in chapter 5.

Besides large grain size the orientation of the resulting grains and the structural quality of the grains is of crucial importance for the subsequent epitaxial thickening. It was demonstrated that the resulting poly-Si layers exhibit a preferen-

tial $(100)$ orientation [81]. This crystal $(100)$ orientation is desirable for low-temperature epitaxy [90, 91, 64]. Kim et al. [67] showed that the preferential Si grain orientation of the resulting seed layers depends on the annealing temperature. Low annealing temperature leads to a higher degree of preferential $(100)$ orientation. Here not only the annealing temperature but also the influence of the interface was investigated. In Fig. 4.12 EBSD maps for samples of type B and C annealed at three different temperatures namely at $450\,$°C, $500\,$°C and $550\,$°C are shown. The different colors in the maps correspond to different crystal orientations: red is $(100)$, green is $(110)$ and blue is $(111)$ orientation. No orientation could be assigned to the black spots either due to inhomogeneities in the crystallite or at the sample surface. In general the maps for the sample with native oxide interface (type B) are more red, i.e. more grains are close to $(100)$ orientation, than in case of samples with thermal oxide (type C) which are more blue, i.e. more grains are close to $(111)$ orientation. Thus, the ALILE process allows the fabrication of both, layers with a preferential $(100)$ orientation and layers with a $(111)$ orientation. Remarkably almost none of the maps exhibits clear green color indicating that almost no grains of $(110)$ orientation are formed. When looking at the temperature dependence the finding of Kim et al. [67] is confirmed. The lower the annealing temperature the more $(100)$ orientated grains are found for both oxide interlayers.

The EBSD maps in Fig. 4.12 have different scale because also the nucleation densities differ strongly. For the sample type C (thermal oxide) the estimated grain sizes are above $100\,\mu\mathrm{m}$ for all annealing temperatures. In the maps it is evident that areas of homogenous crystal orientation are much smaller than the estimated grain size. Thus it is concluded, that each region grown from nucleus must include several orientations in case of sample type C. Furthermore many black spots are found which might be due to a microcrystalline structure. For the sample type B (native oxide) larger connected areas with similar orientation can be distinguished. From optical micrographs the grain size was estimated to be $12\,\mu\mathrm{m}$ in case of the sample annealed at $T_A = 550\,$°C increasing up to $36\,\mu\mathrm{m}$ for the sample

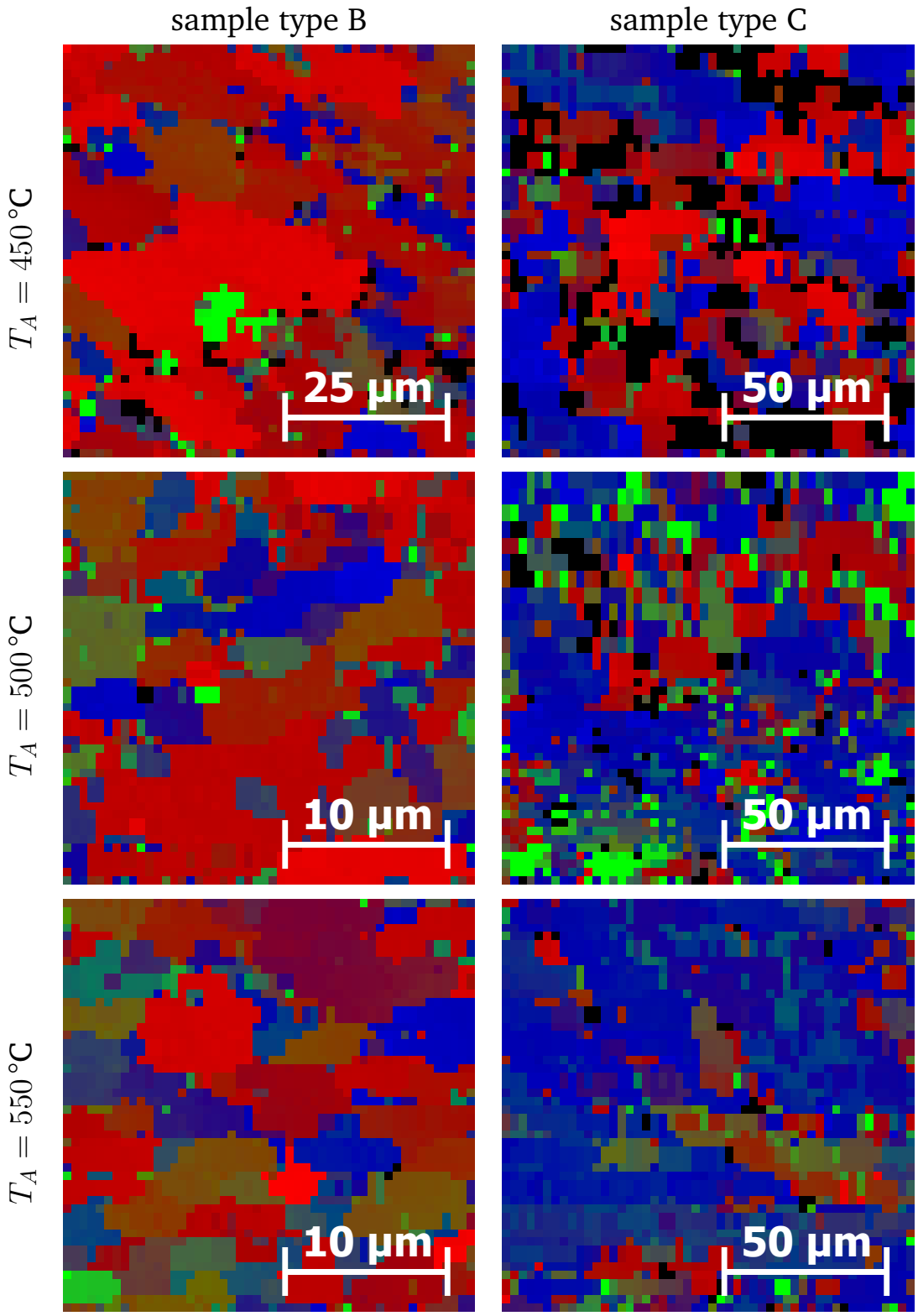


**Figure 4.12:** EBSD maps for samples type B (native oxide) and C (thermal oxide) annealed at $450\,°C$, $500\,°C$ and $550\,°C$. Native oxide and low annealing temperature enhance the degree of preferential $(100)$ orientation.

annealed at $T_A = 450\,$°C. This leads to the conclusion that the nucleation density does not correspond directly to a crystallographic grain size. Further investigations concerning the structure within the areas growing from one nucleus in the seed layers have to be performed.

The inverse pole figures for the two most distinct case for (a) the sample type B (native oxide) annealed at low temperature ($T_A = 450\,$°C) and (b) sample type C (thermal oxide) annealed at high temperature ($T_A = 550\,$°C) are shown in Fig. 4.13. The inverse pole figure is the superposition of all equivalent orientations. The three corners correspond to the the three low index orientations (100), (110) and (111) like the color code from the EBSD maps. The detection spots agglomerate close to the $(100)$ orientation in Fig. 4.13(a) and close to the $(111)$ orientation in Fig. 4.13(b).

In order to quantify the result obtained for the different samples the red fraction of the maps has been analyzed. The red fraction is changed with the tilting angle $\alpha$ with respect to the $(100)$ orientation ($\alpha = 0° = (100)$). All angles larger than $45°$ have no red fraction. The ratio of orientation within $\alpha \leq 20°$ to the overall area under investigation is referred to as preferential $(100)$ orientation $R_{(100)}$. Fig. 4.14 shows $R_{(100)}$ for the six EBSD maps. The solid circles correspond to the native oxide results (sample type B) and the open circles to the thermal oxide (sample type C). The above described trend can be confirmed for the preferential $(100)$ orientation $R_{(100)}$. The native oxide and lower annealing temperature $T_A$ enhance the degree of preferential $(100)$ orientation. For the sample of type B annealed at $450\,$°C $R_{(100)}$ is close to $70\,\%$. For sample of type C and an annealing temperature of $550\,$°C $R_{(100)}$ decreased below $10\,\%$[5].

Usually preferential orientations are determined by the fastest growth of a particular orientation. Depending on the velocity of a process or subprocess preferential orientations are formed. In the presented case the thermal oxide (sample type C)

[5]The preferential $(100)$ orientation $R_{(100)}$ is quantitative but limited number for the orientations in the films. It allows for a quantitative evaluation but comparison of the EBSD maps in Fig. 4.12 with the result shown in Fig. 4.14 shows strong differences even for similar $R_{(100)}$.

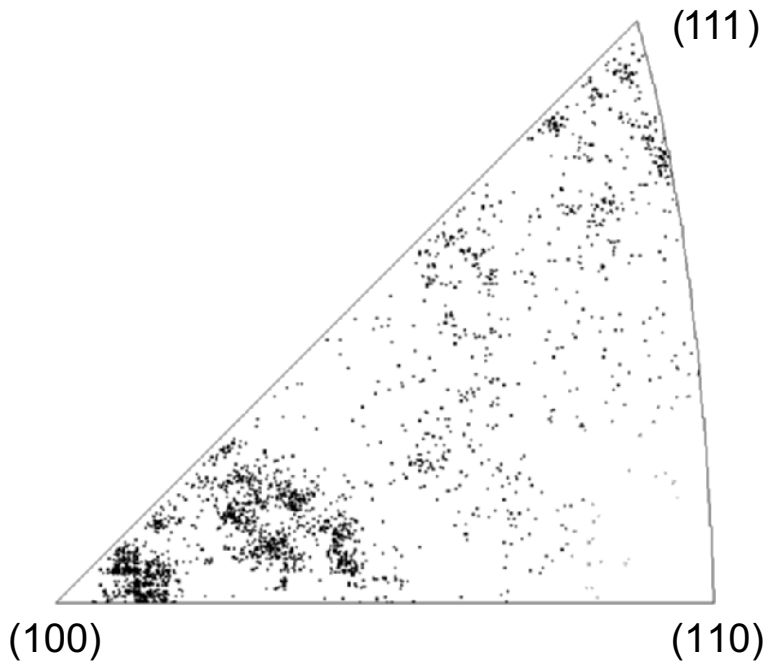


(a)

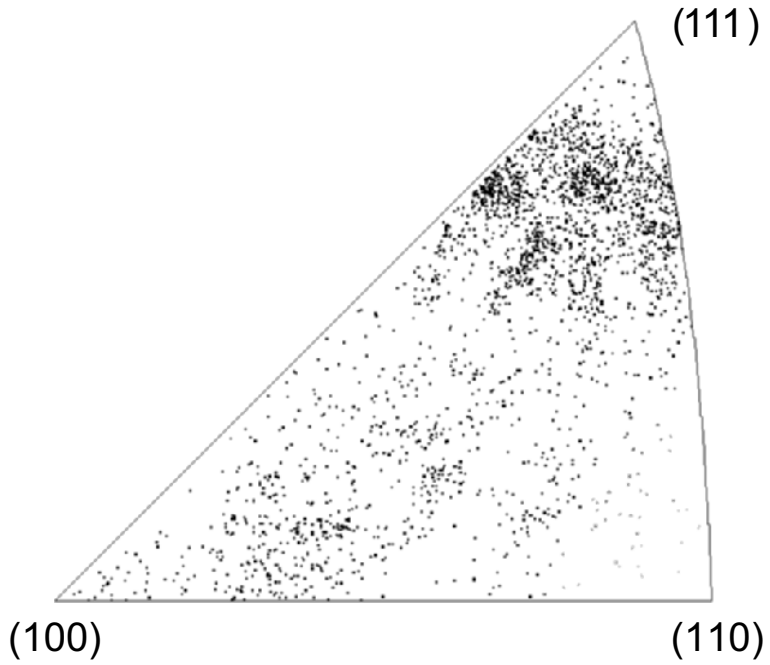


(b)

**Figure 4.13:** Inverse pole figures corresponding to the EBSD maps shown in Fig. 4.12 for (a) the sample type B (native oxide) and low annealing temperature ($T_A = 450\,°\text{C}$) and (b) the sample type C (thermal oxide) and high annealing temperature ($T_A = 550\,°\text{C}$). In (a) a preferential $(100)$ orientation in (b) a preferential $(111)$ orientation is detected. In neither case (110) orientated grains are found.

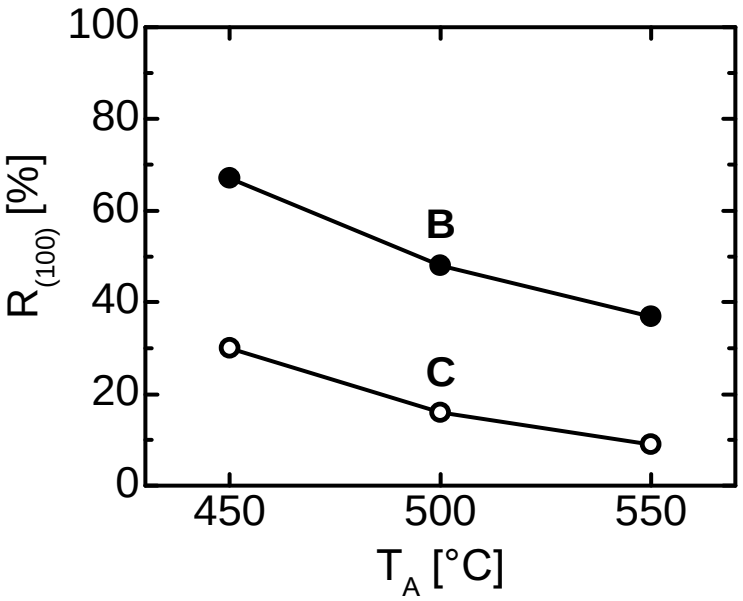


**Figure 4.14:** Preferential $(100)$ orientation $R_{(100)}$ as a function of the annealing temperature $T_A$ for sample type B (solid circles) and sample type C (open circles). The preferential $(100)$ orientation $R_{(100)}$ is defined as the ratio of orientations tilted by $\leq 20°$ with respect to the $(100)$ orientation. The results are obtained from analyzing the EBSD maps in Fig. 4.12. Lower annealing temperature $T_A$ and thinner oxide interlayer leads to a higher preferential $(100)$ orientation.

annealed at low temperature ($450\,$°C) is the slowest and the native oxide (sample type B) annealed at high temperature ($550\,$°C) is the fastest process. But these two cases exhibit no strong preferential orientation ($R_{(100)} \approx 30..40\,\%$).

Besides the large grains the second important attribute of the ALILE seed layers is the preferential $(100)$ orientation. By altering the annealing temperature and the type of oxide interlayer the degree of preferential $(100)$ orientation has been modified succesfully. With a native oxide and low annealing temperature a preferential $(100)$ orientation of up to $R_{(100)} = 70\,\%$ was obtained. The use of a thermal oxide and high annealing temperature decreased the preferential $(100)$ orientation below $10\,\%$. In section 5.5 a possible explanation for this behavior is suggested. It will be shown that the annealing temperature and interlayer influence can be explained by preferential nucleation of silicon at the interface.

### 4.1.2 Molybdenum interface

An attractive alternative to the oxidation of the aluminum layer is the direct deposition of an interlayer. This would allow to deposit the layer stack without breaking the vacuum which allows much faster sample preparation. On the one hand direct or reactive deposition of an oxide is an option. However, also very different approaches can be followed. Here, thin molybdenum layers deposited between the initial Al and a-Si layers were studied as an alternative to the oxide interlayer. In Al metallization Mo, W and Ta based Si nitrides and other compounds are used as diffusion barrier [92, 93]. A Mo target within the DC magnetron sputtering chamber for Al and a-Si deposition allowed the alternative use of a Mo interlayer without any vacuum break and resulting oxidation of the Al layer. Since Mo is used in Al/Si diffusion barriers investigations it was explored wether the diffusion barrier could be deposited thin enough to allow controlled diffusion between the two layers.

The controlled deposition of very thin layers is quite challenging especially with DC magnetron sputtering. To verify the success of the deposition Auger electron spectroscopy (AES) depth profiles were measured. In Fig. 4.15 the AES results for specimens with a nominal Mo thickness of $d_{Mo} = 12\,\mathrm{nm}$, $24\,\mathrm{nm}$ and $48\,\mathrm{nm}$ between the initial Al and a-Si layers are shown. It is clearly demonstrated that the amount of Mo at the interface increased. Thus different thicknesses of the Mo interlayer were successfully deposited.

In Fig. 4.16 the crystallized fraction $R_C$ curves for samples with nominal $12\,\mathrm{nm}$, $24\,\mathrm{nm}$ and $48\,\mathrm{nm}$ Mo thicknesses are shown. The annealing temperature was $550\,°\mathrm{C}$. With increasing Mo interface thickness the processes is slowed down. While the layer exchange for the $12\,\mathrm{nm}$ Mo sample is finished in $6 - 7\,\mathrm{min}$, the layer exchange of the sample with $48\,\mathrm{nm}$ Mo starts after about $20\,\mathrm{min}$ only.

The saturation value of the crystallized fraction decreases gradually with increasing interlayer thickness. While for $12\,\mathrm{nm}$ Mo a complete layer exchange can be observed ($R_C = 100\,\%$), only about $R_C = 80\,\%$ are reached for $48\,\mathrm{nm}$ Mo. In

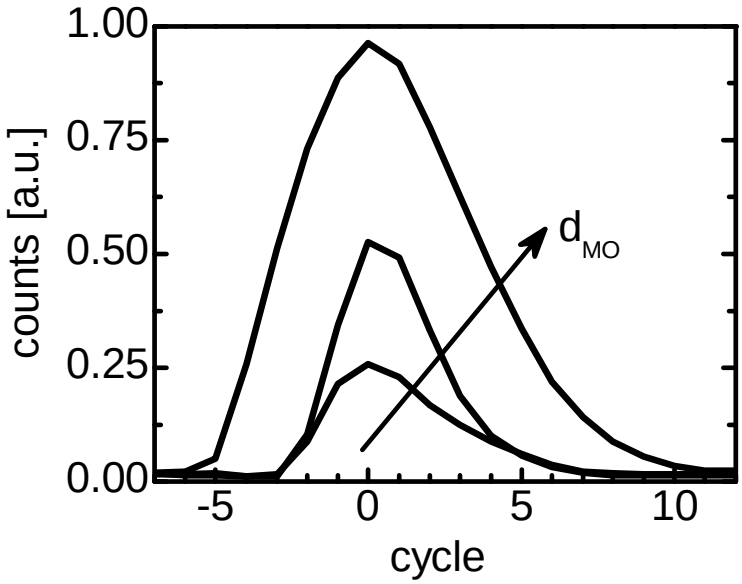


**Figure 4.15:** Counts versus sputtering cycles from Auger electron spectroscopy Mo depth analysis of samples with three different Mo interfaces. The cycles have been normalized such that the Mo maximum counts are in cycle $0$ for all samples. The nominal thickness of the Mo film is $d_{Mo} = 12\,\mathrm{nm}$, $24\,\mathrm{nm}$ and $48\,\mathrm{nm}$.

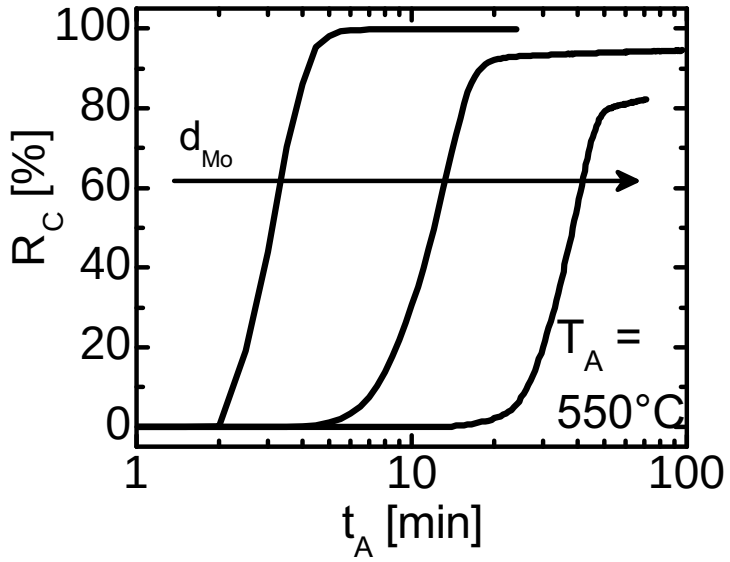


**Figure 4.16:** Crystallized fraction $R_C$ versus annealing time $t_A$ for samples with different nominal thicknesses of the Mo interlayer ($d_{Mo} = 12\,\mathrm{nm}$, $24\,\mathrm{nm}$ and $48\,\mathrm{nm}$). The samples were annealed at $T_A = 450\,°\mathrm{C}$.

Fig. 4.17 optical micrographs of a sample with $48\,\mathrm{nm}$ Mo interlayer thickness are shown after annealing for $25\,\mathrm{min}$, $35\,\mathrm{min}$ and $45\,\mathrm{min}$ at $550\,°\mathrm{C}$. For this samples the growth of a single, dendritic crystallite can be observed. The dendritic growth is strongly reduced in case of thinner Mo layers (not shown here). The reason why the crystallized fraction does not reach $100\,\%$ is due to Al inclusion caused by the dendritic growth. It has to be pointed out that the crystallized fraction curve in case of a single crystallite within the image area is not correct. The actual crystallized fraction develops slower. In $R_C$ just the fraction of the image area transformed is evaluated. In case of the sample shown in Fig. 4.17 the grain is much larger than the image. Thus, the grain growth continues outside the image area while $R_C$ already reached it's maximum. As a matter of fact the crystal in Fig. 4.17 grew to about $700\,\mu\mathrm{m}$ final diameter which could only be detected in a larger micrograph (not shown here).

Crystallized fraction curves $R_C\,(t_A)$ for samples with $12\,\mathrm{nm}$ Mo interlayer thickness annealed at different temperatures are shown in Fig. 4.18. The curves are similar to the ones from the oxide interfaces. Higher annealing temperature decreases the process time. However different from the case of the oxide layer [94] the nucleation time does not strongly denpend on the annealing temperature. The reason for this remains unclear. Probably the nucleation starts right away due to the direct contact of metal (Mo) to a-Si instead of having an intermediate dielectric oxide layer. This could support the screening effect suggested by Hiraki [30]. However, it remains unclear why this would only influence the nucleation time but not the process time.

In Fig. 4.19 the nucleation density $N_G$ and estimated grain size $d_G$ as a function of the annealing temperature $T_A$ for the specimen with $12\,\mathrm{nm}$ Mo interface are shown. Quite large estimated grain sizes $d_G$ of up to $40\,\mu\mathrm{m}$ were obtained.

The Mo interlayer was found to have an advantageous side effect. The surface topography of a sample grown with an $12\,\mathrm{nm}$ Mo interlayer after etching off the Al is shown in Fig. 4.20. According to the SEM micrograph a smooth seed layer

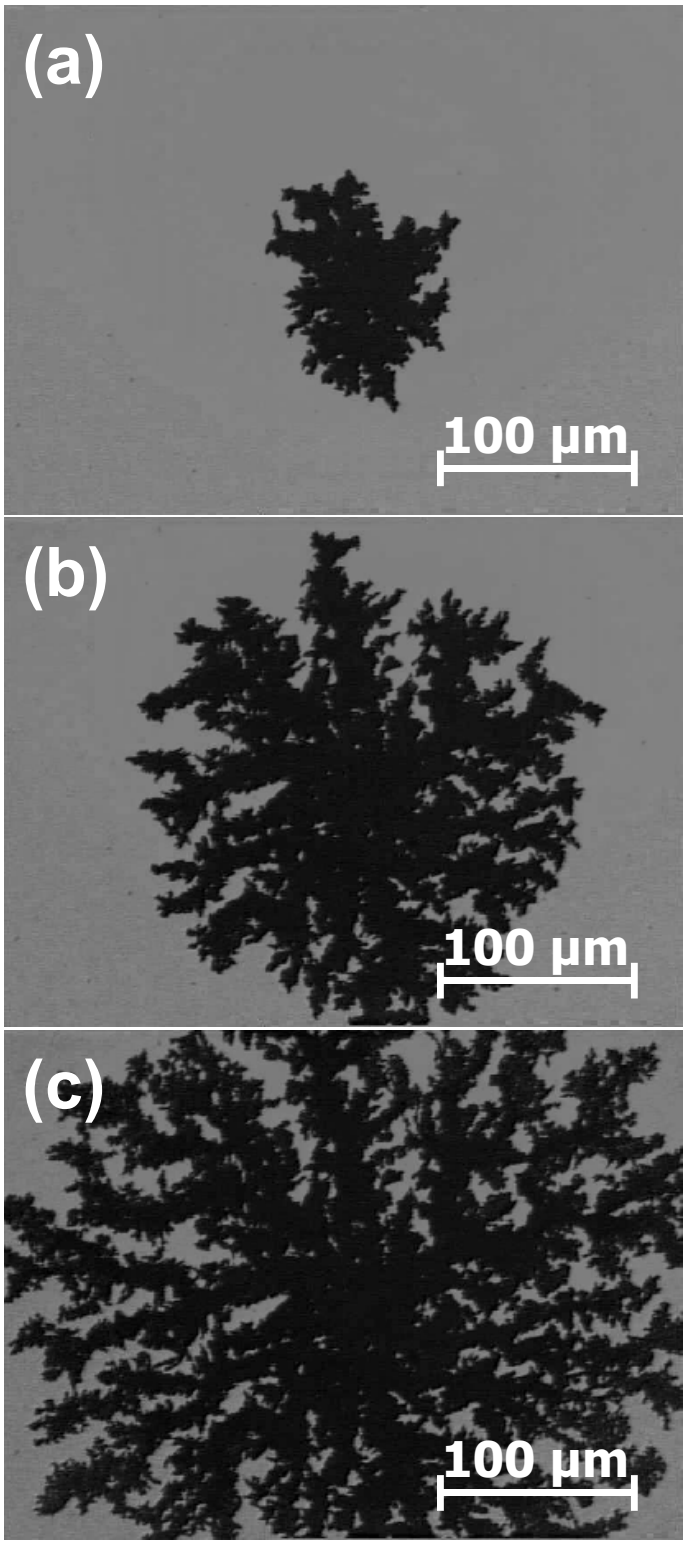


**Figure 4.17:** Series of optical micrographs of the initial glass/Al interface showing a large dendritic grain growing during annealing of a specimen with $48\,\mathrm{nm}$ Mo interlayer at $550\,°\mathrm{C}$ after (a) $25\,\mathrm{min}$, (b) $35\,\mathrm{min}$ and (c) $45\,\mathrm{min}$.

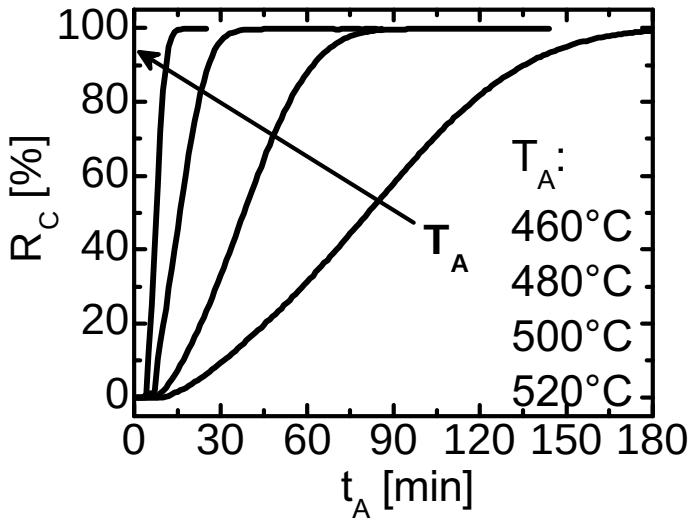


**Figure 4.18:** Results for $12\,\mathrm{nm}$ molybdenum interface. Crystallized fraction $R_C$ vs. annealing time $t_A$ at different annealing temperatures $T_A$.

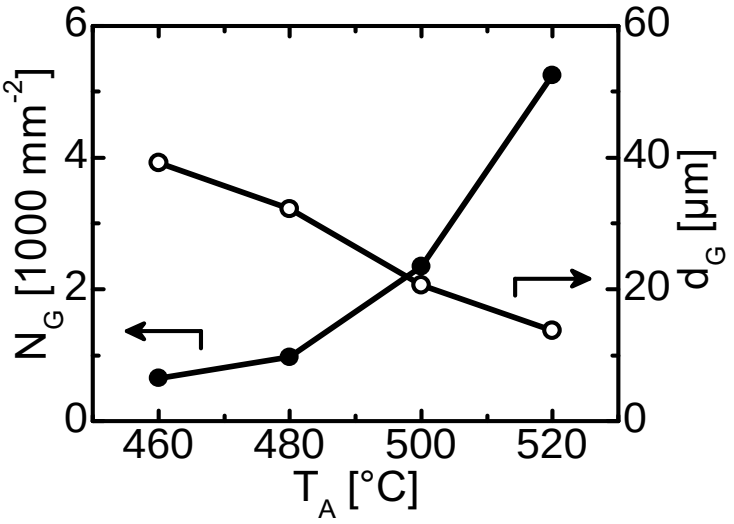


**Figure 4.19:** Results for $12\,\mathrm{nm}$ molybdenum interface. Nucleation density $N_G$ (solid circles) and estimated grain size $d_G$ (open circles) versus annealing temperature $T_A$.

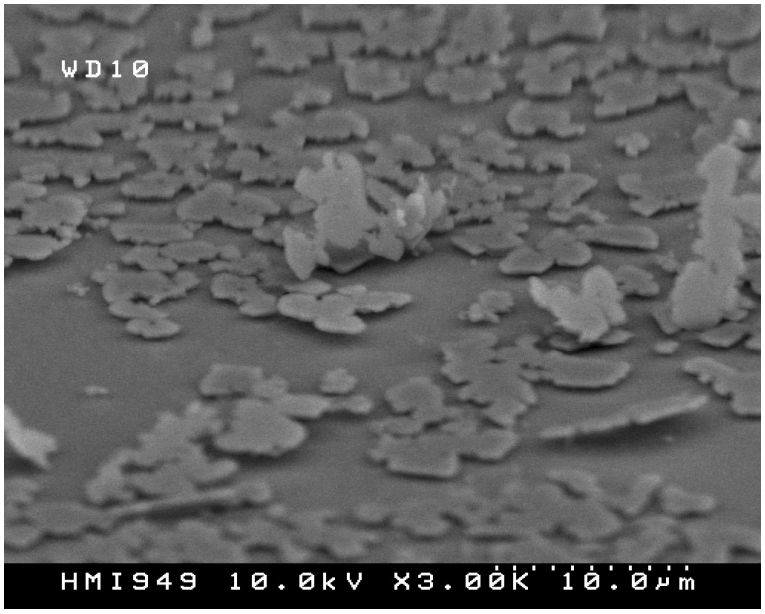


**Figure 4.20:** SEM image of a sample with $12\,\mathrm{nm}$ Mo interlayer after complete layer exchange and standard Al etching. As for samples with oxide interface layer silicon islands are formed in the top layer. Due to the removal of the Mo interlayer by the Al etchant some of these islands are lifted off.

has formed and the crystalline Si islands in the top layer have partially been lifted off without any mechanical force. The removal of the Si islands has to be assured prior to epitaxial thickening. A lift off process would probably be the most elegant way to achieve the removal of the islands. A similar lift off process was suggested by special adjustment of the oxide layer and the etching technique [95]. Here the Al oxide layer is etched at high temperature ($130\,^{\circ}\mathrm{C}$) in a phosphoric acid based etchant. The use of alternative (non Al oxide) interface layers might offer an easier path towards a Si islands lift off process than the use of a chemically very resistant Al oxide interlayer.

Within this section it was shown that not only oxide layers can serve as suitable interlayers which allow a complete layer exchange and the formation of a continuous poly-Si layer. This indicates that there is probably a large variety of suitable interlayer materials. In microelectronics many different alloys are used as diffusion barriers in metallization. Among those there could be reasonable candidates for the ALILE process. In conclusion of these results it is suggested that the inter-

face layer has to fulfill two main requirements.

1. Thermal stability: The interlayer should be thermally stable, i.e. the melting point should be much higher than the annealing temperature.

2. Chemical stability: The interlayer should not form alloys with either Al or Si at the annealing temperature.

Unfortunately, the second point made Mo not the ideal choice. It was found that in some experiments both Al and Si react with Mo. Better materials need to be found. So far native Al oxide as interlayer material still yields the best result due to homogeneously connected crystallites and preferential $(100)$ orientation.

## 4.2 Temperature profiles

Besides the interlayer the annealing temperature is the most important parameter in the ALILE process. So far only isothermal experiments were made. In the following experiments are described which use temperature profiles in order to improve the process by increasing the grain size to process time ratio in heating step experiments (4.2.1) and to improve the understanding of the process by enforcing additional nucleation in cooling step experiments (4.2.2).

The experience obtained from the interlayer experiments described in the previous chapter were used in the selection of the proper specimens for the two types of temperature profile experiments. The heating step experiments which aim at optimizing the process were performed with samples which are regularly used (similar to sample type B). These samples were oxidized by exposure to air for $2\,\mathrm{h}$. In the cooling experiments samples with a low nucleation density were needed. But the layer exchange should not take too long. Thus samples were thermally oxidized at $525\,°\mathrm{C}$ for $1.5\,\mathrm{h}$ (similar to sample type C) and annealed at temperatures up to $550\,°\mathrm{C}$ in order to obtain a fast layer exchange.

### 4.2.1 Heating step

In isothermal annealing experiments the ALILE process could be divided in three phases (see Fig. 4.11). In the *growth phase III* no additional grains are formed and the layer exchange process is continued merely by growth of existing grains. The idea of the heating step experiments is to increase the annealing temperature during the *growth phase* in order to increase the grain growth velocity and thus decrease the process time without causing additional nucleation. In all experiments samples of a specific specimen were used in order to maintain the best comparability of the obtained results. For reference purposes samples have been annealed at a constant temperature nominally $460\,$°C and $500\,$°C. For the heating step experiments the annealing was started at nominally $460\,$°C and increased to an annealing temperature of maximal $500\,$°C. Two different kinds of procedures were applied. In experiment *HS1* the nominal annealing temperature $T_A$ was increased from $460\,$°C to $500\,$°C while varying the step time $t_S$ from $40\,\mathrm{min}$, $60\,\mathrm{min}$ to $80\,\mathrm{min}$ (Fig. 4.21(a)). For the reference curves (dashed lines) the annealing took place isothermally at $460\,$°C and $500\,$°C. In experiment *HS2* the nominal annealing temperature was increased from $460\,$°C in steps of $T_S = 10\,$°C, $20\,$°C, $30\,$°C and $40\,$°C at $t_S = 60\,\mathrm{min}$ (Fig. 4.21(b)). Again the reference profiles are indicated as dashed lines.

Figure 4.22 shows the crystallized fraction $R_C$ curves for experiment *HS1*. The very left and very right curve (dashed lines) represent the reference curves annealed isothermally at $500\,$°C and $460\,$°C, respectively. The other curves show the results of the heating step experiments. The three $R_C\,(t_A)$ curves show the same behavior before the temperature change. This is an indicator for the reproducibility of the experiment. At the annealing steps $t_S = 40\,\mathrm{min}$, $60\,\mathrm{min}$ and $80\,\mathrm{min}$ $R_C$ has reached $1.5\,\%$, $12.6\,\%$ and $45.1\,\%$, respectively. As a result of the temperature change the slope of the $R_C$ curves increases strongly for $t > t_S$. Due to the higher temperature the grain growth velocity is increased and additional nucleation takes place. Thus the slope of the $R_C$ curves has a similar slope as the reference curve

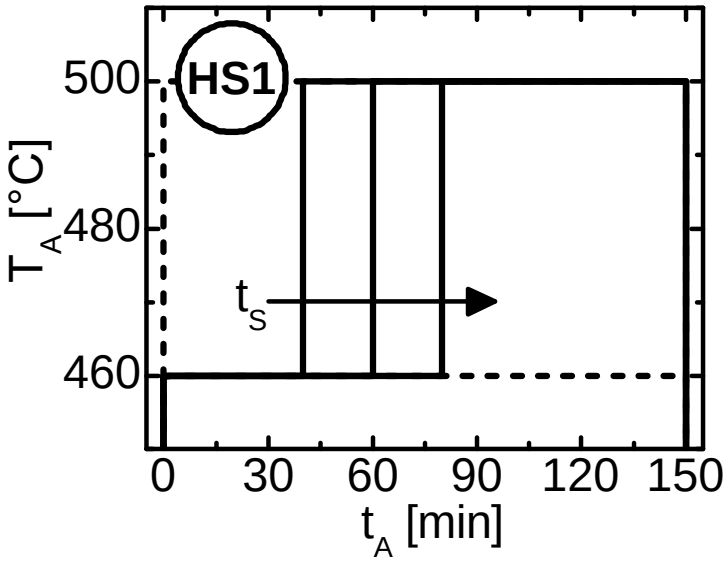


(a)

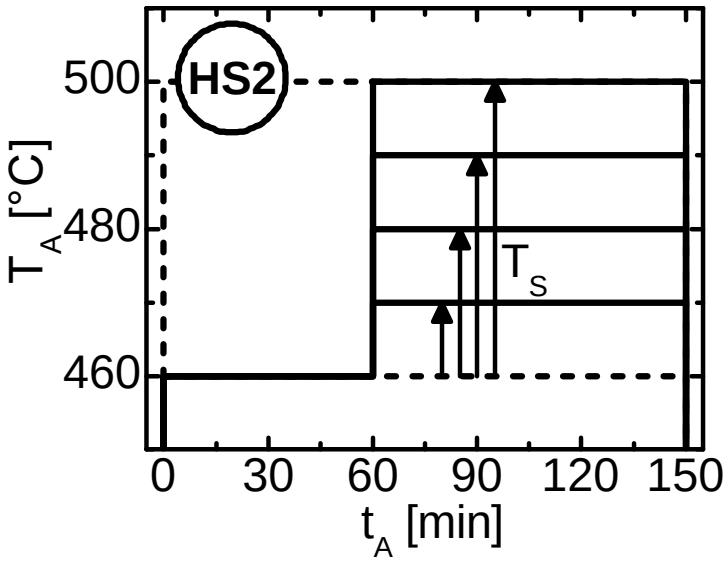


(b)

**Figure 4.21:** Annealing temperature $T_A$ versus annealing time $t_A$ for the temperature profiles used in non-isothermal annealing experiments. (a) *HS1*: variation of the heating step time $t_S$. (b) *HS2*: variation of the heating step temperature $T_S$. Dashed lines are the reference profiles annealed isothermally.

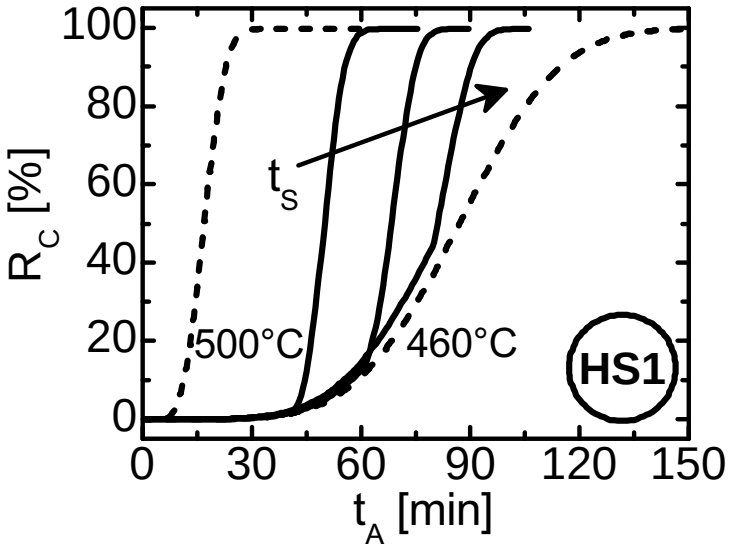


**Figure 4.22:** Crystallized fraction $R_C$ vs. annealing time $t_A$ for experiment *HS1*. The left and the right curves (dashed lines) are isothermal anneals at $500\,$°C and $460\,$°C, respectively. The other samples where annealed at $460\,$°C until $t_S = 40\,\mathrm{min}$, $60\,\mathrm{min}$ and $80\,\mathrm{min}$ and then heated to $500\,$°C.

annealed at $500\,$°C. This leads to a strong reduction in process time compared to the reference curve annealed at $460\,$°C.

In Fig. 4.23 the $R_C\,(t_A)$ curves for experiment *HS2* are shown. Again the same reference curves are included as dashed lines. Up to $t_A = 60\,\mathrm{min}$ the three $R_C$ curves follow the same dependence. At $t_A = 60\,\mathrm{min}$ $R_C$ varies only between $8.9\,\%$ and $12.9\,\%$ for the three samples. The slope of the $R_C$ curves clearly increases with increasing $T_S$. The process time $t_P$ ($R_C = 95\,\%$) is reduced by up to $45\,\mathrm{min}$ for the sample with the highest $T_S$ as compared to the reference sample annealed at $460\,$°C.

The main objective of these experiments is the modification of the temperature profile in order to get large grains in short process times. In order to distinguish between the nucleation density at the heating step and the final nucleation density the indices $S$ and $F$ are introduced, respectively. The values have to be calculated differently because the layer exchange is not complete at the step time. Thus, not the entire image area is covered by Si but only the crystallized fraction. This has

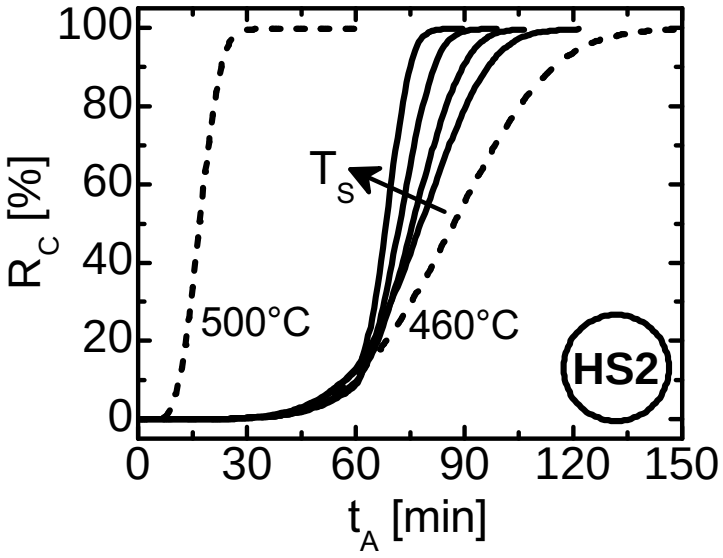


**Figure 4.23:** Crystallized fraction $R_C$ vs. annealing time $t_A$ for experiment *HS2*. The left and the right curves (dashed lines) are isothermal anneals at $500\,$°C and $460\,$°C, respectively. (b) The step temperature $T_S$ has been varied from $10\,$°C, $20\,$°C, $30\,$°C to $40\,$°C at $t_S = 60\,\mathrm{min}$.

to be taken into account when calculating the grain size. To determine the nucleation density the number of objects in the micrographs is counted. The largest number of objects $N_0$ within an image during the entire annealing together with the image area $A_0$ determines the average final nucleation density $N_{G,F} = N_0/A_0$. The average final grain area $A_{G,F}$ is inversely proportional to the final grain density $N_{G,F}$, $A_{G,F} = 1/N_{G,F}$. The average final estimated grain size $d_{G,F}$ is the square root of the average final grain area $A_{G,F}$ ($d_{G,F} = {A_{G,F}}^{1/2}$). Hence, lower $N_{G,F}$ is desirable to increase the grain size. The nucleation density $N_{G,S}$ at the step time $t_S$ is calculated similar to $N_{G,F}$, but using the number of objects $N_{0,S}$ at $t_S$ ($N_{G,S} = N_{0,S}/A_0$). Calculating the average grain area $A_{G,S}$ at the step time $t_S$ it has to be taken into account that not the entire area is covered with silicon but only the crystallized fraction $R_C$. Thus $A_{G,S}$ is inversely proportional to the nucleation density $N_{G,S}$ multiplied by the crystallized fraction $R_{C,S}$ at the step time $t_S$ ($A_{G,S} = R_{C,S} \cdot 1/N_{G,S}$). The average estimated grain size $d_{G,S}$ is the square root of the average grain area $A_{G,S}$ ($d_{G,s} = {A_{G,S}}^{1/2}$).

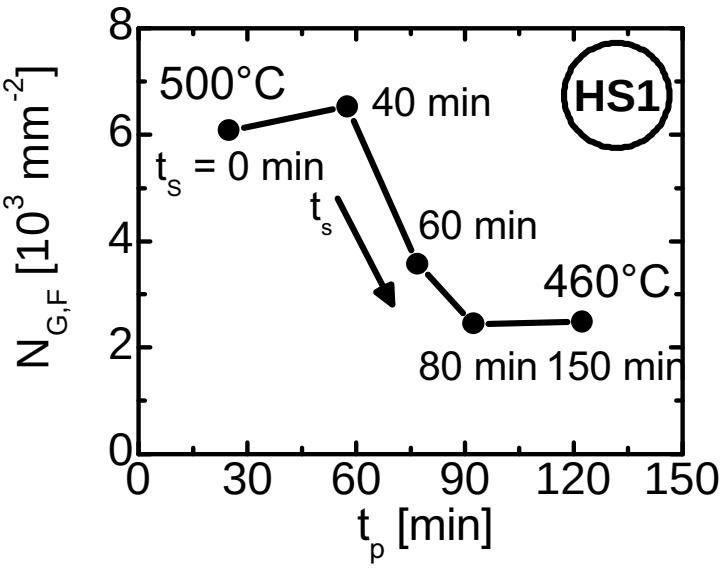


**Figure 4.24:** Average final grain density $N_{G,F}$ vs. process time $t_P$ for experiment HS1. The corresponding step times are indicated. The reference curves have been interpreted as $t_S$ = 0 min (500 °C) and $t_S$ = 150 min (460 °C). $N_{G,F}$ decreases strongly for $t_S$ between 40 min and 80 min.

In Fig. 4.24 $N_{G,F}$ is shown versus the process time $t_P$ (time at $R_C = 95\,\%$) for experiment *HS1* together with the corresponding step times $t_S$. The final nucleation density $N_{G,F}$ is strongly modified by $t_S$. Increasing the temperature from $460\,$°C to $500\,$°C after $40\,\mathrm{min}$ does not lead to a major change in $N_{G,F}$ compared with the isothermal anneal at $500\,$°C ($t_S = 0\,\mathrm{min}$). Between $t_S = 40\,\mathrm{min}$ and $t_S = 80\,\mathrm{min}$ increasing $t_S$ results in a strong reduction of $N_{G,F}$. Whereas for times above $80\,\mathrm{min}$ no further change can be observed. This means that upon reaching a certain annealing time $t_A$ the annealing temperature can be increased without any new nucleation. Thus the grain size remains the same but the process time is reduced. The initial goal of the heating step approach has been reached successfully even with a single temperature step. It is believed that an annealing temperature limit exists to which the sample can be heated at any time without additional nucleation. The time evolution of this annealing temperature limit is unclear.

In order to investigate the behavior more closely a further specimen prepared with the same deposition parameters as the specimen before has been annealed with

a smaller increment in step time and step temperature. It was found that for this specimen the decrease in $N_{G,F}$ took place already at a shorter step time of $30\,\mathrm{min}$ to $50\,\mathrm{min}$ instead of $40\,\mathrm{min}$ to $80\,\mathrm{min}$ as for the specimen examined above. In the experiments both step temperature $T_S$ and step time $t_S$ were varied in order to determine the course of the annealing temperature limit. Thus, various step time and step temperature couples from $t_S = [30, 35, 40, 50\,\mathrm{min}]$ and $T_S = [5, 10, 15, 20, 25\,°\mathrm{C}]$ were chosen. In Fig. 4.25 the difference between $N_{G,F}$ and $N_{G,S}$, i.e. the additional average nucleation density, is shown versus the average grain size $d_{G,S}$ at the step time $t_S$. It can clearly be seen in the figure that upon reaching an average grain size at $t_S$ of about $d_{G,S} = 5.5\,\mu\mathrm{m}$ no further nucleation occurs. This behavior is independent of the step temperature (not shown here). However, when the average grain size $d_{G,S}$ at $t_S$ is below $5.5\,\mu\mathrm{m}$ new nucleation takes place depending on the step temperature $T_S$. Higher $T_S$ are accompanied by an increase of the nucleation (not shown in Fig. 4.25). The average final grain density does not exceed $N_{G,F} = 3.7 \cdot 10^3\,\mathrm{mm}^{-2}$ in case of $d_{G,S} > 5.5\,\mu\mathrm{m}$. Thus the maximum final grain size that can be reached is about $d_{G,F} = 16.5\,\mu\mathrm{m}$ ($d_{G,F} = (1/N_{G,F})^{1/2}$ with $N_{G,F} = 3.7 \cdot 10^3\,\mathrm{mm}^{-2}$).

This observation can be interpreted as follows. At the step time $t_S$ there exists a zone of $d_Z = 5.5\,\mu\mathrm{m}$ (at $d_{G,S} = 5.5\,\mu\mathrm{m}$) on each side of the grain where no new nucleation ($d_{G,F} = d_{G,S} + 2d_Z$) takes place (Fig. 4.26). Once these zones overlap the temperature can be increased to higher values and still now new grains nucleate. This is a first experimental proof for the depletion regions responsible for the suppression of nucleation suggested by Nast et al. [52].

The goal of the heating step experiments was to reduce the process time without increasing the nucleation density. This goal was achieved. An estimated grain size limit was found at which the annealing temperature could be increased without new nucleation. This is a first proof for the depletion regions being responsible for the nucleation suppression. With increasing the annealing temperature after the critical grain size is reached the grain growth velocity can be increased strongly and thus the process time is decreased without further nucleation.

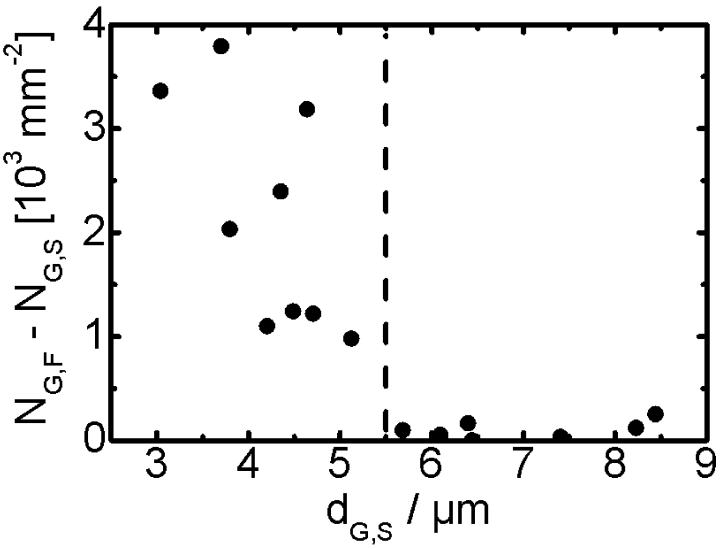


**Figure 4.25:** Additional nucleation, i.e. difference between average final grain density $N_{G,F}$ and average grain density at the step time $N_{G,S}$ vs. average grain size at the step time $d_{G,S}$ for various step time and step temperature couples, $t_S = [30, 35, 40, 50\,\mathrm{min}]$ and $T_S = [5, 10, 15, 20, 25\,°\mathrm{C}]$. As soon as $d_{G,S}$ is larger than $5.5\,\mu\mathrm{m}$, no new nucleation can be observed.

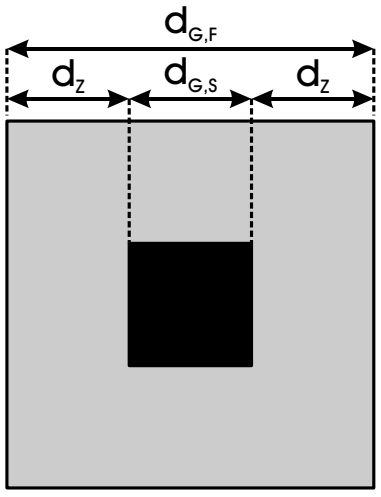


**Figure 4.26:** Sketch of a grain at the step time $t_S$. The final grain size $d_{G,F}$ is the grain size at the step time $d_{G,S}$ plus twice a zone depleted of silicon around the growing grain $d_Z$ ($d_{G,F} = d_{G,S} + 2d_Z$).

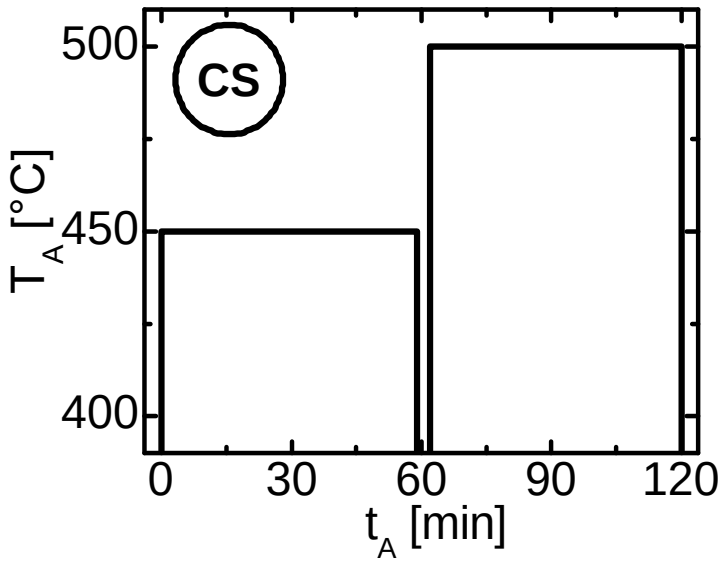


**Figure 4.27:** Annealing temperature $T_A$ versus annealing time $t_A$ for the temperature profile for the cooling step experiment CS. A specimen from the heating step experiments A and B was cooled down to $330\,°C$ within $1\,\mathrm{min}$ before being heated to $500\,°C$.

### 4.2.2 Cooling step

Increasing the annealing temperature before the critical grain size is reached leads to an increase in nucleation density. In chapter 2 it has been pointed out that in multi component systems supercooling and supersaturation lead to nucleation. In the regular isothermal annealing procedure used in the ALILE process nucleation is obviously not caused by supercooling but by supersaturation. Decreasing the annealing temperature causes an even stronger increase in nucleation density. Such experiments give further direct evidence for the formation of depletion regions which control and stop nucleation. First the heating step and the cooling step influence are compared. A sample with a thermal oxide interlayer formed at $500\,°C$ for $1.5\,\mathrm{h}$ was prepared in order to obtain larger grain sizes. In Fig. 4.27 the temperature profile for the first cooling step experiment CS is shown. After $60\,\mathrm{min}$ annealing at $450\,°C$ the sample is cooled to $330\,°C$ within $1\,\mathrm{min}$ prior to a heating step to $500\,°C$. This was compared to a direct heating step to $500\,°C$ after $60\,\mathrm{min}$ annealing at $450\,°C$.

The comparison of micrographs with and without cooling step prior to the heat-

ing step are shown in Fig. 4.28. Again, the bright areas correspond to aluminum whereas the dark spots represent silicon crystallites. Fig. 4.28a was taken after $60\,\mathrm{min}$ annealing at $450\,°\mathrm{C}$ prior to the heating or cooling step. $R_C$ is very small (below $1\,\%$) and the formed nuclei are about $50\,\mu\mathrm{m}$ apart from each other. Fig. 4.28b shows the same sample at the same position after additional annealing for $22\,\mathrm{min}$ at $500\,°\mathrm{C}$. $R_C$ has increased to $25\,\%$. In Fig. 4.28b the same specimen at the same position is shown as in Fig. 4.28a. Comparison of Fig. 4.28a and 4.28b reveals that due to the additional annealing the grains grew significantly and that only very few additional grains have formed. Those are smaller than the already existing grains. Fig. 4.28c shows a sample which had gone through a $1\,\mathrm{min}$ cooling period (see temperature profile Fig. 4.27) before it was heated at $500\,°\mathrm{C}$ for $20\,\mathrm{min}$. The number of nuclei has increased strongly. The sample has not reached $500\,°\mathrm{C}$ as fast as the sample without cooling period. In consequence the grains did not grow to the same, large sizes within comparable time. However, due to the additional nucleation $R_C$ reached $25\,\%$ after about the same time, too. These experiments show that both heating and cooling of a specimen can lead to additional nucleation. Cooling the sample leads to a higher nucleation density than heating.

In another experiment a specimen of type B was annealed at $460\,°\mathrm{C}$ for $240\,\mathrm{min}$ and then cooled down to $220\,°\mathrm{C}$ within $7\,\mathrm{min}$. After cool down the sample was reheated to $520\,°\mathrm{C}$ for $60\,\mathrm{min}$. In Fig. 4.29 optical micrographs of the specimen are shown. Fig. 4.29a shows the sample after $237\,\mathrm{min}$ annealing just before cool down. The different grains are round shaped and can be clearly distinguished. They have approximately the same size (about $30\,\mu\mathrm{m}$). This means that the grains have nucleated at approximately the same time assuming similar grain growth rates . No new grains are formed in case of continued annealing at constant temperature. Fig. 4.29b shows the same specimen at the same position after cool down and reheating (after $253\,\mathrm{min}$). Again, many new silicon grains appeared in the Al layer. The nucleation density before cool down was about $7 \cdot 10^2\,\mathrm{mm}^{-2}$. After cool down and reheating the Si nucleation density of newly formed grains within the initial Al layer was above $5 \cdot 10^4\,\mathrm{mm}^{-2}$. The new Si nuclei are homogeneously

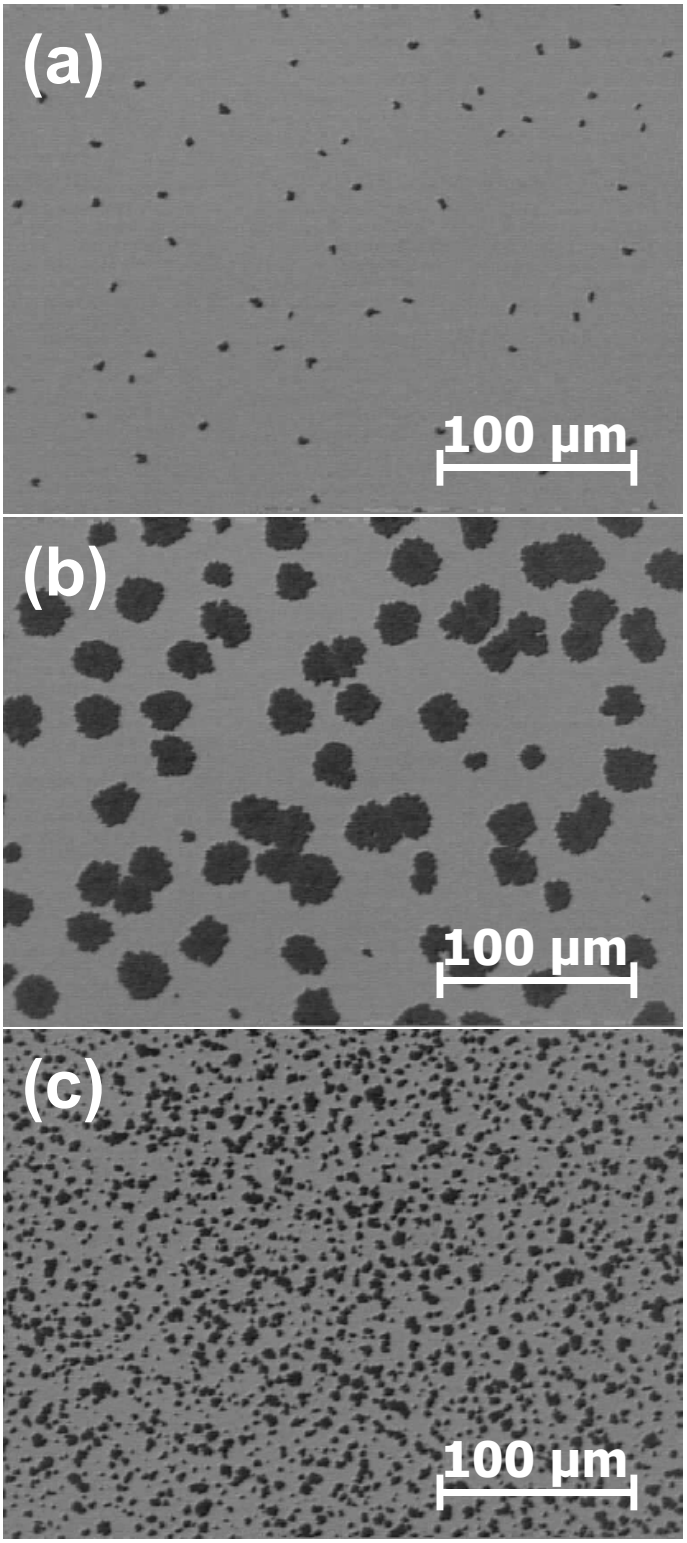


**Figure 4.28:** Optical micrographs from experiment CS. Sample after $60\,\mathrm{min}$ annealing at $450\,°\mathrm{C}$ (a), and subsequent heating to $500\,°\mathrm{C}$ for $22\,\mathrm{min}$ (b). A samples that includes a cooling step down to $330\,°\mathrm{C}$ for $1\,\mathrm{min}$ and was then heated to $500\,°\mathrm{C}$ is shown after a total of $81\,\mathrm{min}$ in (c).

distributed. It is important to notice that there are regions without new nuclei around the preexisting grains. Those are the above introduced depletion regions. The width of the depletion regions is about $9\,\mu\mathrm{m}$ in this case. This is the first direct evidence for the depletion regions. They are made visible directly.

As shown above (Fig. 4.28) samples heated up without cool down did not show this behavior. Thus the cool down (not the reheating) leads to a very high nucleation density far away from the preexisting grains. In the vicinity of the preexisting grains nucleation is suppressed. When reheating the newly formed nuclei grow and become visible in the micrographs. The growth of both the preexisting and the newly formed grains finally leads to the formation of a continuous layer.

In the two cooling step experiments described above two important observations have been made: (i) when cooling the sample during the layer exchange process for a short time many new nuclei are formed. (ii) Under certain conditions of such cooling steps direct evidence of a region without nucleation around existing grains can be found. In order to study these observations more closely a special experiment was designed. Samples with large grain size were chosen in order to obtain a low nucleation density. This allows to investigate both the new nucleation density $\rho_N$ and the depletion regions width $L$. Single cooling step experiment were chosen. The different parameters under investigation are elucidated in the measured annealing temperature $T_A\,(t_A)$ profile as a function of the annealing time $t_A$ in Fig. 4.30. In phase P1 the samples are heated and annealed at a starting temperature $T_1$ until after $t_1$ the annealing temperature is decreased. The cooling period (phase P2) is characterized by three parameters. These are the cooling velocity $v_2$, the cooling temperature $T_2$ and the cooling duration $t_2 - t_1$. After the cooling the samples are reheated to the temperature $T_3$ and annealed until the layer exchange is completed (phase P3). If not stated otherwise the samples were first annealed at $T_1 = 550\,$°C for $t_1 = 24\,\mathrm{min}$ and then cooled close to room temperature ($T_2 = 36\,$°C) for $t_2 - t_1 = 15\,\mathrm{min}$ at $v_2 = 180\,\mathrm{K min}^{-1}$ before being reheated to $T_3 = 550\,$°C until the layer exchange was completed. The cooling velocity $v_2$ was determined by a linear fit in the initial cooling and altered by

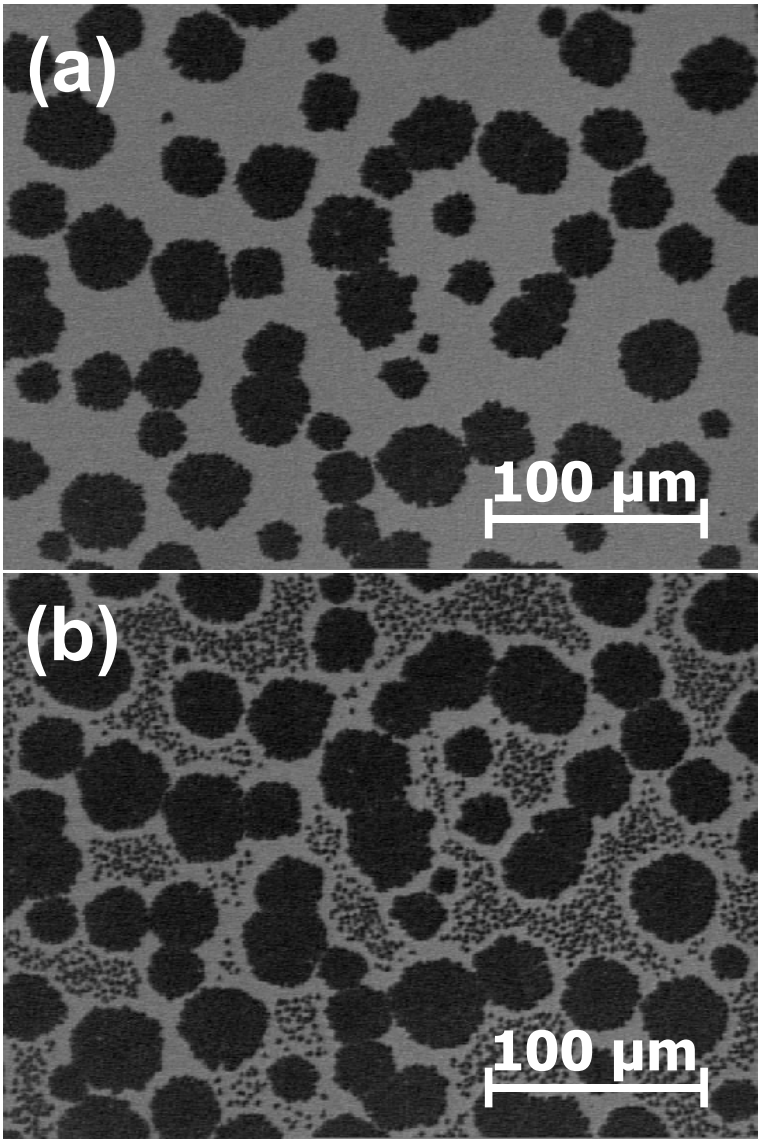


**Figure 4.29:** Optical micrographs taken during annealing of a specimen of type B at $T_A = 460\,°\mathrm{C}$ for about $t_A = 4\,\mathrm{h}$ (a). In a cooling step the annealing temperature $T_A$ was decreased to $220\,°\mathrm{C}$ and before the sample was reheated to $T_A = 520\,°\mathrm{C}$. In (b) after $4\,\mathrm{h}13\,\mathrm{min}$ many new grains have appeared. Around the existing, large grains regions without new nuclei were formed (depletion regions).

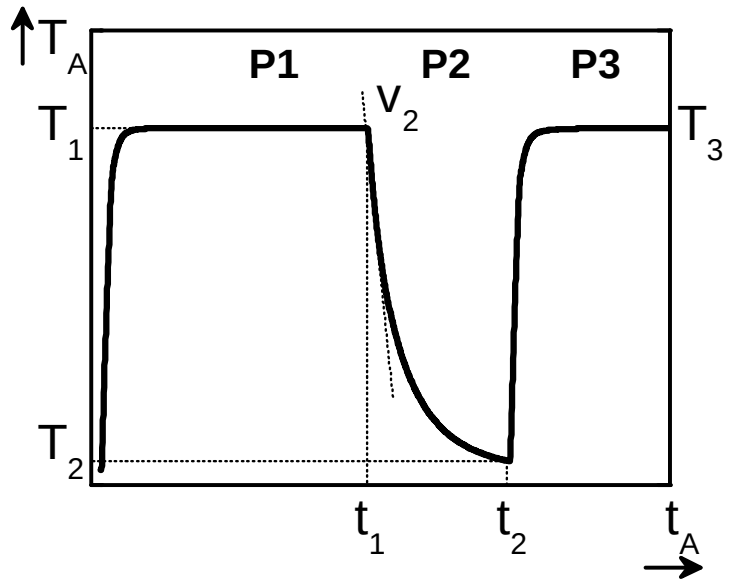


**Figure 4.30:** Measured annealing temperature $T_A$ versus annealing time $t_A$ for the cooling experiments. The important parameters are the temperatures $T_1$, $T_2$ and $T_3$ and the times $t_1$ and $t_2$. The cooling velocity $v_2$ was found to play a crucial role. In this exemplary case the parameters have been $T_1 = 550\,°\text{C}$ until $t_1 = 28\,\text{min}$, a cooling step $T_2 = 36\,°\text{C}$ until $t_2 = 43\,\text{min}$ with $v_2 = 180\,\text{K}\,\text{min}^{-1}$ before being reheated to $T_3 = 550\,°\text{C}$.

introducing small intermediated temperature steps, e.g. several steps decreasing the annealing temperature $T_A$ by $10\,\text{K}$ lasting $10\,\text{s}$ each. The resulting measured decrease in the annealing temperature $T_A$ is approximately linear at about $v_2 = 60\,\text{Kmin}^{-1}$.

In Fig. 4.31a the micrograph of a sample at the time $t_1$ before cooling is shown. Large grains can be seen here. Between the large grains no new nuclei have been formed, i.e. the process is in the growth phase III as defined in section 4.1.1. the distance between the grains is significantly larger than $100\,\mu\text{m}$. In Fig. 4.31b the micrograph of the same sample at $t_2$ after the cooling period (phase P2) is shown. The large grains can still be observed. In the areas without nuclei prior to the cooling step a large number of new nuclei have appeared. Around the large grains regions without additional nuclei, the depletion regions, are visible as shown above (see Fig. 4.31b). The results obtained here are used in the model

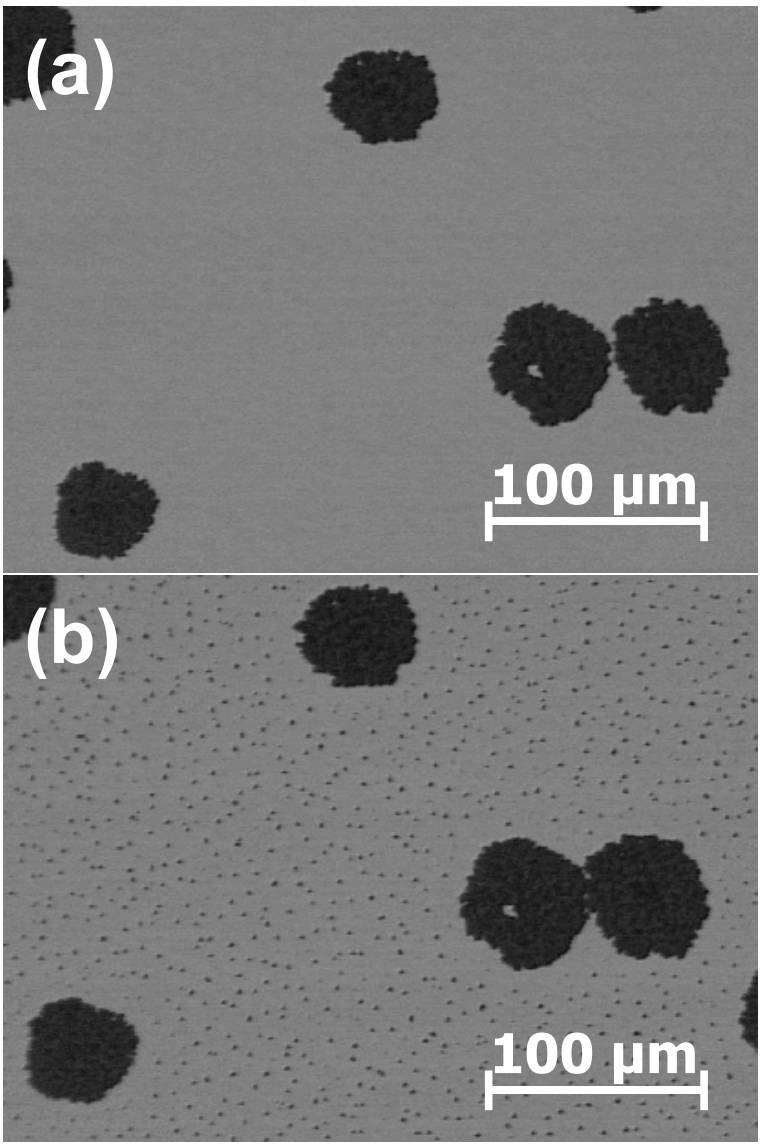


**Figure 4.31:** (a) Optical micrograph of a sample after $t_1$ (just before cooling). Large grains grow with a distance of more than $100\,\mu\mathrm{m}$. (b) The same position at $t_2$. A large number of new nuclei have formed. Around the existing grains depletion regions without nuclei are visible.

presented in chapter 5.

The method to determine the depletion region width $L$ is illustrated in Fig. 4.32. Concentric circles are placed around both the grain and the grain with the corresponding depletion region. The difference in circle radii is interpreted as the depletion region width $L$. The mean value for all grains in a micrograph was used as depletion region width $L$. In a series of experiments the dependence of the

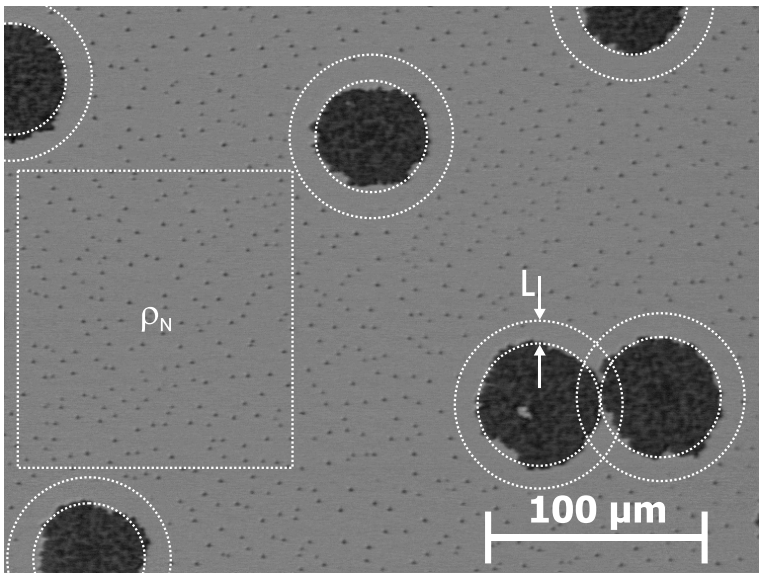


**Figure 4.32:** Evaluation method of the depletion width $L$ and the new nucleation density $\rho_N$ illustrated for the specimen shown in Fig. 4.31. $L$ is the difference in radius of the two concentric circles. The inner circle describes the grain size, while the outer circle describes the grain size plus the depletion region. The additional nucleation density $\rho_N$ has been determined in rectangles outside the depletion regions.

depletion region width and the density of the newly formed grains $\rho_N$ - in the area without grains prior to the cooling step- on the process parameters of the cooling experiments was investigated.

The depletion region width $L$ as well as the density of the newly formed grains was found to be independent of the crystallized fraction $R_C$ which correspond to the point in time when cooling starts $t_1$ (Fig. 4.33). With the results from section 4.1.1 this means that neither the grain size nor the crystallized fraction strongly influence the shape of the depletion regions. Smaller depletion region widths are only obtained when the samples are cooled right after the appearance of the first grains.

The dependencies of the density of newly formed grains $\rho_N$ on both, the temperature before cooling $T_1$ (Fig. 4.34(a)) and the temperature at the end of the cooling period $T_2$ (Fig. 4.34(b)) show a decreasing density of newly formed grains with increasing temperature. In chapter 5 these results will be explained in terms of a

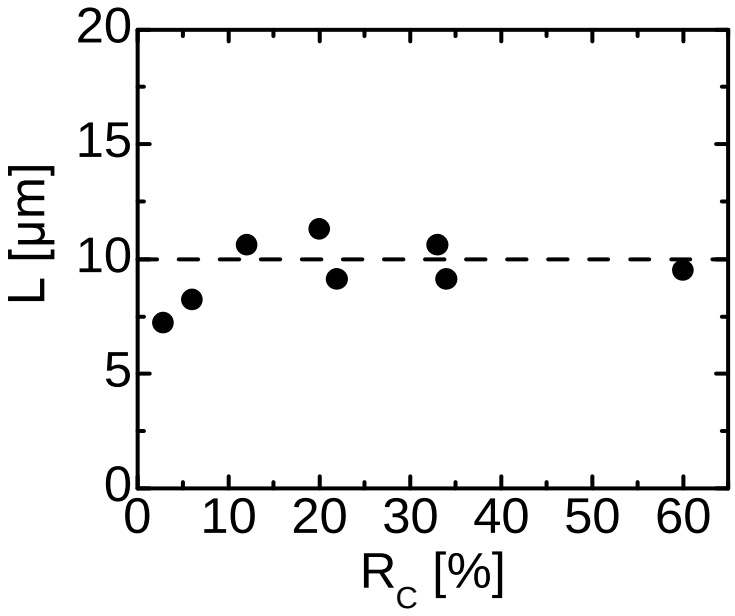


**Figure 4.33:** Depletion region width $L$ as a function of the crystallized fraction $R_C$ at the end of phase I before the cooling step. The depletion region width is constant about $10\,\mu\mathrm{m}$. Only for very low crystallized fractions $R_C$ the depletion region width decreases slightly.

model for nucleation and growth. Here only some handwaving ideas are given to show the direction.

For the experiments shown in Fig. 4.34(a) the samples were annealed at various temperatures $T_1$ until the crystallized fraction $R_C$ reached a value of $10..20\,\%$. Then the samples were cooled to room temperature (RT) for $15\,\mathrm{min}$. The standard parameter is $T_1 = 550\,°\mathrm{C}$ indicated by a dotted line. The fact that the nucleation density is decreasing with increasing temperature $T_1$ is striking, because the higher the temperature the more silicon is dissolved in the Al. The higher silicon concentration does not lead to a larger nucleation density. In order to incorporate more silicon the silicon nuclei formed during cooling must be larger in case of higher temperature $T_1$. The velocity of the silicon atoms is higher at higher temperatures. The effective distance the silicon atoms diffuse before they are frozen in during the cooling step is the integral of the velocity over time. Starting at higher annealing temperature increases both the velocity and the time until the atoms are frozen

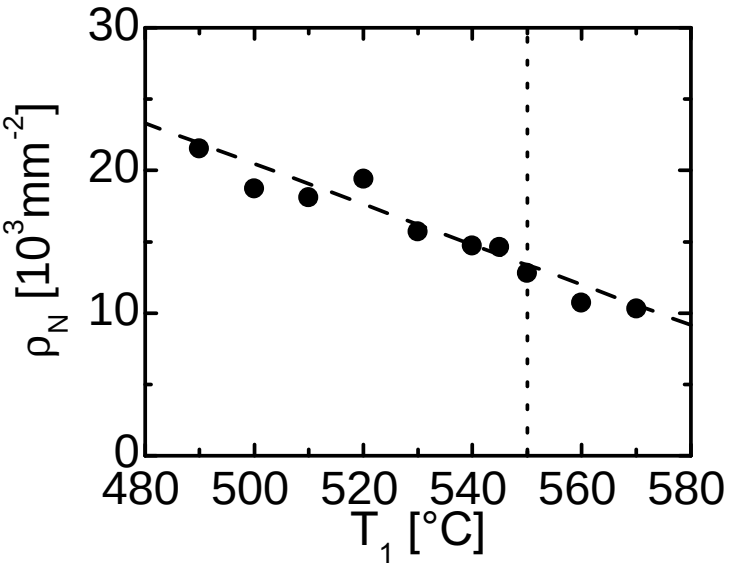


(a)

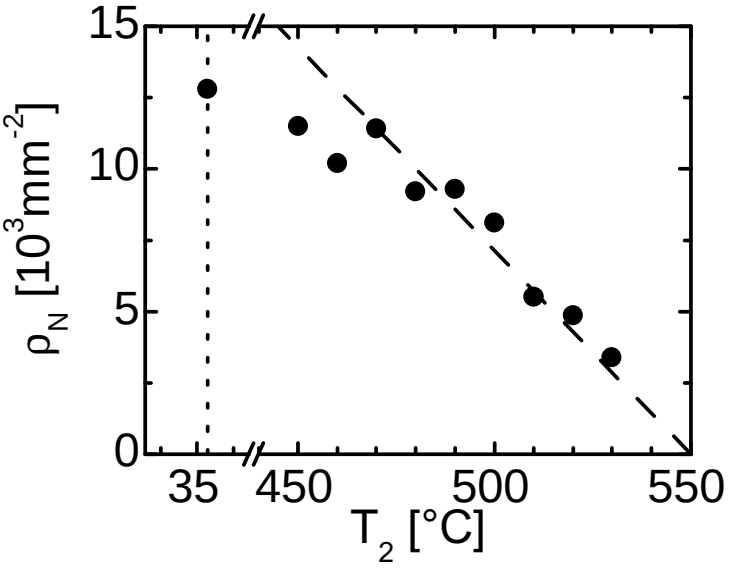


(b)

**Figure 4.34:** Density of newly formed nuclei $\rho_N$ as a function of (a) the temperature $T_1$ before cooling and (b) the temperature $T_2$ at the end of the cooling period. The common, standard parameters are indicated as dotted lines. All samples in (a) were cooled close to RT (36 °C) within $t_2 - t_1 = 15\,\mathrm{min}$. Before cooling samples were annealed at $T_1 = 550\,$°C.

in. Thus the effective distance is larger and thus each formed nucleus can agglomerate more silicon atoms and thus becomes larger. The decrease in nucleation density $\rho_N$ as function of the temperature $T_1$ can be approximated linearly.

The results in Fig. 4.34(b) have been obtained while cooling the sample to different temperatures $T_2$. In all cases the initial temperature $T_1$ was $550\,$°C. The specimens were cooled to the corresponding temperature $T_2$. Once $T_2$ was reached the sample was kept at this temperature for $t_2 - t_1 = 15\,\mathrm{min}$. $T_2$ was varied from $450\,$°C to $540\,$°C. Additionally the result for the standard sample cooled to $36\,$°C is included (dotted line). At small differences $T_1 - T_2$ the course of the new nucleation density $\rho_N$ can be approximated linearly with an intersection with the temperature scale at $550\,$°C, i.e. no cooling step, which makes sense. At larger differences the new nucleation density $\rho_N$ saturates. The obtained results can be understood considering the silicon concentration in the Al layer, again. The Si saturation concentration $C_S$ in Al decreases as a function of the temperature. The larger the temperature change the higher the supersaturation $S = C_{Si}/C_S$ of the Al and the higher the nucleation rate. The saturation of the new nucleation density $\rho_N$ indicates that all nuclei are already formed when the temperature has decreased by about $100\,\mathrm{K}$.

The parameter which has the strongest impact in the cooling experiments is the cooling rate $v_2$. To investigate this parameter the samples were cooled for $15\,\mathrm{min}$ from $550\,$°C to $450\,$°C. When $450\,$°C were reached the temperature was kept constant until $t_2 - t_1$ reached $15\,\mathrm{min}$. The cooling rate $v_2$ was change by introducing small temperature steps, e.g. changing the temperature for $10\,\mathrm{K}$ every $10\,\mathrm{s}$ leads to a cooling velocity of $60\,\mathrm{K min}^{-1}$. The faster the samples are cooled the smaller the depletion region width (Fig. 4.35(a)). At cooling rates above $100\,\mathrm{K\,min}^{-1}$ the depletion region width is approximately constant at about $10\,\mu\mathrm{m}$. This is almost twice as large as the result obtained for the heating step experiments ($L = 5.5\,\mu\mathrm{m}$) described in the previous chapter. This could be attributed to the differences in the studied samples but also to the different dynamics of the process during the heating or cooling step. For slower cooling rates the depletion region width increases

to about $30\,\mu\mathrm{m}$. The dependence of the density of newly formed grains on the cooling rate is shown in Fig. 4.35(b). The faster the cooling rate $v_2$ the larger the newly formed nucleation density $\rho_N$. The dependence can be approximated by a line through origin with a slope of about $75\,\mathrm{min}/\left(\mathrm{K\,mm^2}\right)$. If the cooling velocity $v_2$ is zero, i.e. the sample is not cooled, there is no additional nucleation. Both dependences of the depletion region width $L$ and the nucleation density $\rho_N$ can be understood considering that the integration time is increased and thus the effective diffusion length is increased. The higher the cooling rate, i.e. the faster the sample is cooled, the shorter the distance the silicon atoms can diffuse. Thus the depletion region is smaller because the atoms do not have enough time to diffuse to the existing growing grains. And due to the same reason the nucleation density is larger. These considerations are used in the discussion chapter to elucidate the mechanism responsible for the layer exchange process.

Different interlayers between the initial Al and a-Si layers are investigated. Several Al oxide interlayers as well as an alternative Mo layer are compared. The function of the interlayer is to control the diffusion of silicon into the Al layer. The interlayer separates top and bottom layer throughout the process. Furthermore the interlayer confines the growing silicon grains within the Al layer. It is derived that several interlayers not only oxide layers are suitable. The interlayer has to meet two requirements. It must not be thermally or chemically affected throughout the process but still allow interdiffusion of Al and Si.

The preferential orientation of the resulting poly-Si films has been found to depend both on the annealing temperature and the interlayer. Enhancing the preferential (100) orientation of the layers is mandatory for optimizing the low temperature epitaxy and thus the resulting solar cells.

The use of a heating steps allows to reduce the process time without causing further nucleation. This result reinforces a model with depletion regions causing the nucleation suppression. A cooling step prior to the heating step leads to a very strong increase of nucleation which is expected to originate from supercooling

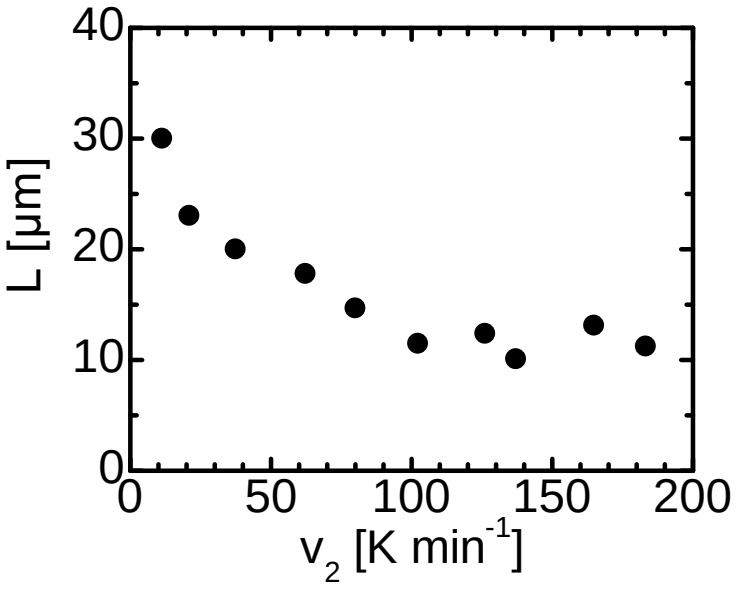


(a)

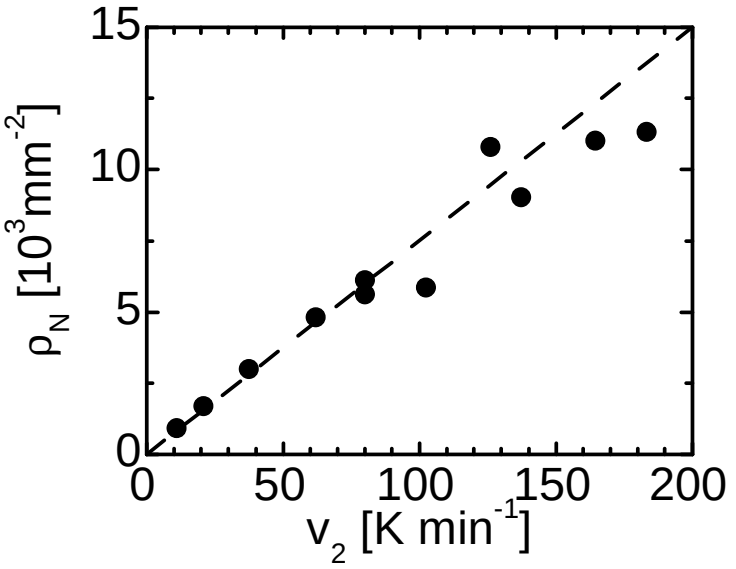


(b)

**Figure 4.35:** (a) Depletion region width $L$ and (b) density of newly formed nuclei $\rho_N$ as a function of the cooling velocity $v_2$.

of the specimen. Zones apparent around the existing grains without additional nucleation are direct proof of the depletion region model.

In the following chapter these findings will be considered and a model will be derived explaining the results.

# 5 Discussion

Two of the most important experimental findings in the aluminum-induced layer exchange process are (i) the suppression of nucleation leading to the formation of large grained poly-Si layers and (ii) the formation of a preferential orientation in these layers. Within this chapter both these findings are discussed.

The model adapted by O. Nast [53] from Ottaviani et al. [40] was extended by Widenborg et al. [55]. The considerations made within this chapter aim at adding further details to this model.

At the beginning of this chapter the very basic, existing model is recalled in Fig. 5.1. On top of the glass substrate the Al (light) and the a-Si (dark) layers are separated by the interface layer (black). The steps of the ALILE process are: (1) Si diffuses across the interface layer into the Al layer. (2) Si diffuses within the Al layer. (3) Si nucleates within the Al layer. (4) Si grains grow. (5) Al diffuses across the interface layer into the initial a-Si layer.

In this chapter it will be shown that the process steps (1) - (4) depend on the silicon concentration within the Al layer. Thus this parameter is very important.

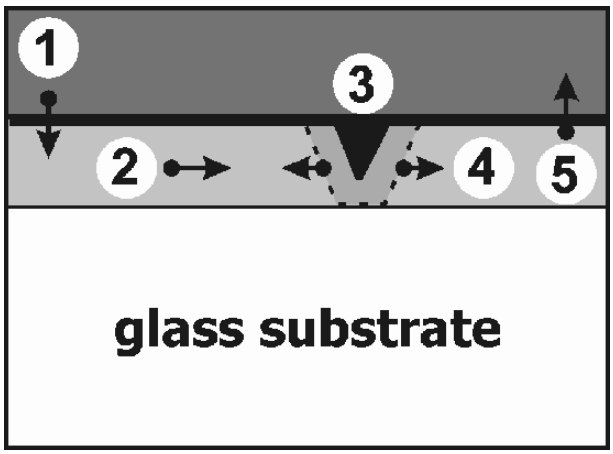


**Figure 5.1:** Scheme of the existing ALILE model separated into 5 major steps: (1) Diffusion of Si across the interlayer; (2) diffusion of Si within the Al layer; (3) nucleation; (4) grain growth; (5) diffusion of Al across the interlayer.

In section 5.1 three crucial Si concentrations will be defined. These are the saturation, maximum and nucleation concentration. These concentrations are used to modify the Al/Si phase diagram and to elucidate the ALILE process within this modified Al/Si phase diagram explaining the origin of the self-limited nucleation suppression (section 5.2). If the silicon concentration is above the saturation concentration but below the critical nucleation no additional nucleation takes place, but existing grains grow.

The considerations made are compared in a very simple qualitative approach with the experimental results from section 4.1 obtained using different interlayers and annealing temperatures (section 5.3). The interaction of the silicon fluxes across the interlayer and within the Al is shown to determine the nucleation time, grain growth velocity and nucleation density.

Finally a model is presented which suggests a possible origin for the preferential orientation in the ALILE process and its dependency on the annealing temperature and the interlayer (section 5.5). This model is based on the idea that the preferential orientation is a result of the preferential formation of certain critical clusters during nucleation.

# 5.1 Definition of three crucial Si concentrations in Al

The concentration of Si within the Al layer is very important to most of the process parameters. The transport of Si atoms from the amorphous silicon layer depends on this parameter as well as the nucleation and growth rate. For the subsequent considerations three crucial Si concentrations are defined using the phase diagram, thermodynamic considerations as well as calculations concerning the nucleation and growth rate.

## 5.1.1 The saturation concentration

In order to understand the thermodynamics of the Al/Si system, a closer look at the Al/Si phase diagram is necessary (Fig. 5.2). The Al/Si system is a eutectic system. The eutectic temperature is $T_{eu} = 850\,\mathrm{K}$. The phase diagram shows the equilibrium lines as a function of the Si content in the Al and the temperature. Even though the phase diagram is only valid in the equilibrium case, it can also be used in the non-equilibrium case in order to understand which state the system tries to reach. In the phase diagram different parts of the system try to form sub-phases which have the mixing ratio of the equilibrium lines at the respective temperature. In Fig. 5.2(b) the Al rich part of the phase diagram is magnified. At the eutectic temperature of $T_{eu} = 850\,\mathrm{K}$ the solid Al dissolves $1.5\,\mathrm{at.\%}$ Si when in contact with a Si system. In the Al rich part of the phase diagram the ALILE process takes place. It is referred to later in this chapter again.

In order to understand phase diagrams it is important to realize that in a binary system there are two degrees of freedom: the volume and the mixing ratio of different subsystems. In thermodynamic equilibrium the subsystems' mixing ratios are defined by the coexistence lines in the phase diagram. This means that any global mixture of material A and material B can be obtained, but the subsystems

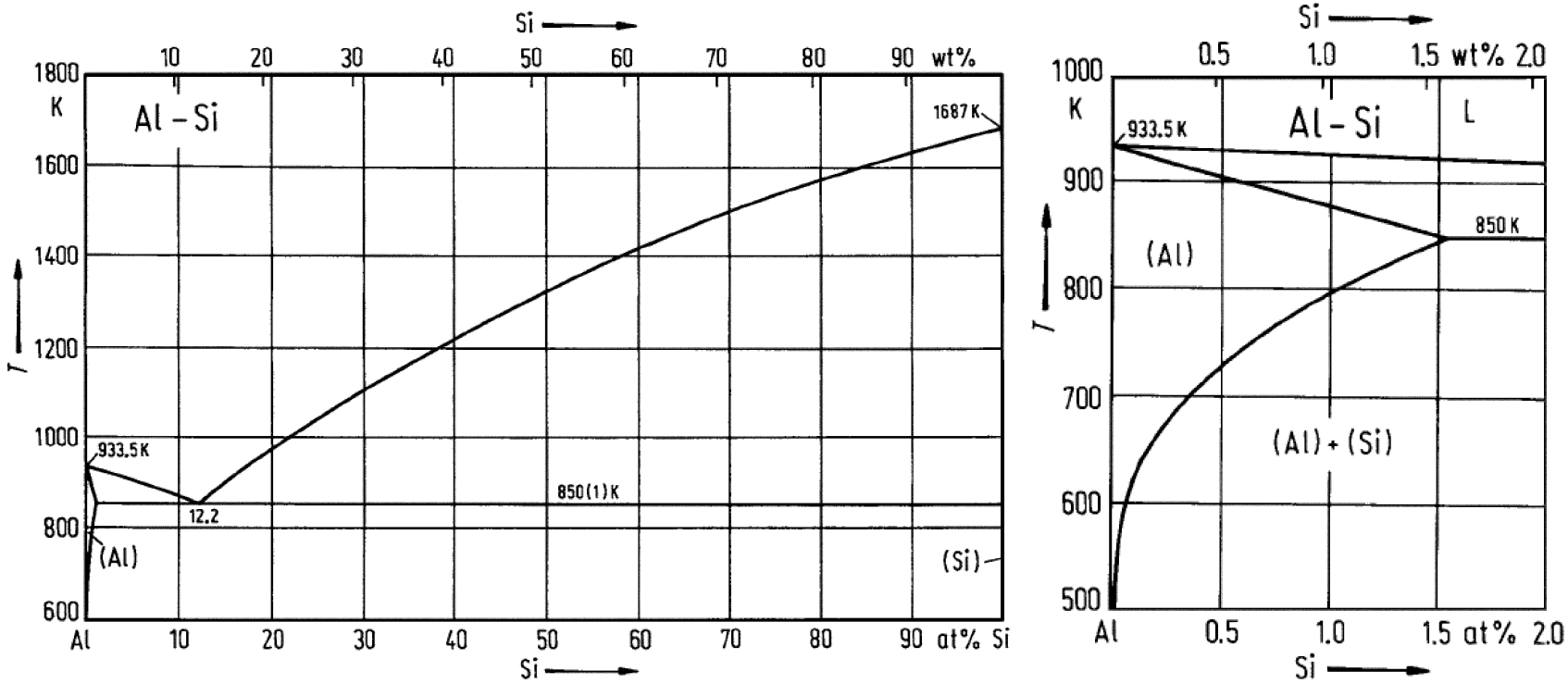


(a) (b)

**Figure 5.2:** Phase diagram of the Al/Si system [96]. (a) Entire phase diagram. At $12.2\,\%$ Si in the Al at a temperature of $850\,\mathrm{K}$ is the characteristic eutectic point. (b) Magnification of the Al rich part of the phase diagram. At the eutectic temperature ($T_{eu} = 850\,\mathrm{K}$) solid Al can dissolve up to $1.5\,\mathrm{at.\%}$ Si.

adjust their mixing ratio according to the phase diagram and their volume fraction according to the overall concentrations.

For example when cooling a liquid, eutectic mixture of Al ($87.8\,\mathrm{at.\%}$) and Si ($12.2\,\mathrm{at.\%}$) an Al and Si phase will solidify at the eutectic temperature. The solid Al parts contain about $1.5\,\mathrm{at.\%}$ silicon. The solid Si parts include below $0.01\,\mathrm{at.\%}$ of Al. In order to achieve this in a eutectic alloy the volume fractions of solid Si and solid Al adjust accordingly.

The coexistence lines in the phase diagram correspond to the thermodynamically most stable, crystalline phases of Al and Si. The coexistence line between the Al and the Al+Si phases in Fig. 5.2(b) is the coexistence line of Al and Si. Two phases are in an equilibrium when the chemical potentials are the same. The chemical potential $\mu_j$ is defined as:

$$\mu_j = \left(\frac{dG}{dN_j}\right)_{T,V,N_{i\neq j}}, \tag{5.1}$$

where $G$ is the Gibbs energy and $N_j$ is the number of particles. The chemical potential is the energy needed to add one particle to a system without a change in temperature $T$, volume $V$ or the number of any other particle $N_{i\neq j}$. In a solution the chemical potential of each species is a function of the concentration. In the case of Si dissolved in Al:

$$\mu_{Si}\left(C_{Si}\right) = \mu_{Si,0} + kT\ln\frac{C_{Si}}{C_S}, \tag{5.2}$$

where $C_{Si}$ is the silicon concentration, $\mu_{Si,0}$ is the chemical potential of Si at the saturation concentration $C_S$ and $k$ is Boltzmann's constant.

As mentioned above the coexistence line from the phase diagram (Fig. 5.2(b)) corresponds to the equilibrium of Si dissolved in Al with the crystalline Si phase. The corresponding concentration is referred to as the *solubility limit* or the *saturation concentration* $C_S$. If the concentration of Si $C_{Si}$ within Al in contact with Si is

below the saturation concentration Si atoms diffuse from the Si into the Al, and the silicon is dissolved. If the concentration of Si within Al is above the saturation concentration Si, atoms diffuse to the crystalline Si surface, and the silicon crystal grows. At $C_S$ the Si crystal neither grows nor is dissolved, the system is in equilibrium.

### 5.1.2 The maximum concentration

The driving force for the entire process is the transition of the amorphous to the crystalline silicon phase. From calorimetric studies the macroscopic enthalpy of the crystallization was determined in kJ/mole [27]. From this value an average change in Gibbs energy per atom can be derived in eV/atom. The energy is temperature dependent. At $750\,\mathrm{K}$ it is $8..10\,\mathrm{kJ/mol}$ which correspond to $0.083..0.104\,\mathrm{eV/atom}$ [12]. Thus about $0.1\,\mathrm{eV/atom}$ is available to drive the entire process.

The amorphous phase has a higher Gibbs energy than the crystalline phase, thus the energy per atom and the chemical potential per atom are higher in amorphous Si than in crystalline Si. This chemical potential difference drives the transition of atoms from an amorphous to a crystalline Si phase. If two phases at an interface are in equilibrium the chemical potentials in both phases must be equal. Thus the silicon in aluminum in equilibrium with the amorphous silicon must have a higher chemical potential than in equilibrium with crystalline Si. The chemical potential of Si in Al depends on the concentration of Si and thus the Si concentration in the Al in equilibrium with the amorphous Si phase must be higher as well. Assuming the Gibbs energy gain per atom at $750\,\mathrm{K}$ to be $0.1\,\mathrm{eV/atom}$, the resulting Si concentration within the Al in equilibrium with the amorphous Si phase can be determined from the change in chemical potential $\Delta\mu$ during the phase transition:

$$\begin{aligned} \Delta\mu &= \mu_{a-Si} - \mu_{c-Si} = 0.1\,\mathrm{eV/atom} && (5.3)\\ &= kT \ln\left(\frac{C_{a-Si}}{C_S}\right) && (5.4)\\ \Rightarrow C_{a-Si} &= C_S \exp\left(\frac{\Delta\mu}{kT}\right) && (5.5)\\ &= 3.8\,\%. && (5.6) \end{aligned}$$

This means that the silicon concentration in Al in equilibrium with the a-Si phase is $3.8\,\%$, which is about $4\times$ as high as the saturation concentration ($C_S\,(T = 750\,\mathrm{K}) = 0.8\,\%$ - from the phase diagram). $C_{a-Si}$ is the maximum Si concentration in the Al which can be achieved by diffusion from the a-Si into the Al. Thus, it will be referred to as $C_{max}$. $C_{max}$ is temperature dependent. A similar calculation was made by O. Nast [53].

### 5.1.3 The critical concentration

Si atoms diffusing into the Al layer either form a new nucleus or contribute to the growth of an existing grain (Fig. 5.1). Both processes, nucleation and growth, depend on the Si concentration within the Al layer.

In general two different growth mechanism are distinguished depending on the slowest, velocity-limiting process step. The two process steps are the incorporation of particles into the growing phase (reaction) and the transport of particles to the growing phase (diffusion). Thus, reaction- or surface-limited and diffusion-limited growth are the two borderline cases. When the growing phase is very small, its surface is small as well and only few particles are incorporated. Thus only a few particles need to be transported to the growing phase for the phase to expand. Usually growth starts to be reaction/surface-limited. While increasing its size, the diffusion of particles to the growing phase gains importance and the growth becomes diffusion-limited. In diffusion-limited growth it is assumed that all atoms supersaturating the Al right in front of the growth front are instantly incorporated

in the grain. As a result the Si concentration at the growth front of the grain is the saturation concentration. In the case of the ALILE process observed with the in-situ optical microscope the grains are already quite large and diffusion limited growth is assumed. In Fig. 5.3 the Si concentration profile in front of a growing crystalline Si grain is shown in case of diffusion-limited growth. The concentration within the grain is the density of Si. As mentioned above, the concentration in the Al cannot be below the saturation concentration $C_S$ because otherwise the Si crystal would dissolve rather than grow. Far away from the grain, the silicon concentration $C$ is higher than $C_S$ and thus a concentration gradient is formed. Silicon atoms diffuse following this concentration gradient. Since all atoms are diffusing to the growing grain the growth rate of the grain is equal to the Si flux density $j_G$ towards the grain. $j_G$ corresponds to the slope of the concentration profile right in front of the grain. Thus the growth rate is determined by Fick's first law:

$$
\begin{aligned}
j_G &= -D \left.\frac{\partial C_{Si}}{\partial x}\right|_{x=0} && (5.7)\\
&\approx -D\frac{C - C_S}{x_G} && (5.8)\\
&= -\frac{D}{x_G} C_S \left(S - 1\right), S = \frac{C}{C_S}, && (5.9)
\end{aligned}
$$

where $D$ is the temperature dependent diffusion coefficient, $C_{Si}$ is the silicon concentration, the growth length $x_G$ depends on the geometry of the crystal growth according to Zener's approximation [97] and $S = \frac{C}{C_S}$ is the supersaturation. Hence, the growth rate $j_G$ is proportional to the supersaturation.

The nucleation rate $j_N$ is a function of the supersaturation as well. In chapter 2 the activation energy for nucleation depending on the volume and the surface term was introduced. According to D.A. Porter and K.E. Easterling [11] an additional strain term has to be taken into account. This strain term is related to the stress induced by the formation of the cluster in its surrounding matrix. It is proportional to the volume of the cluster and can thus be subtracted from the energy gain due to the crystallization of the cluster. In the calculations made here

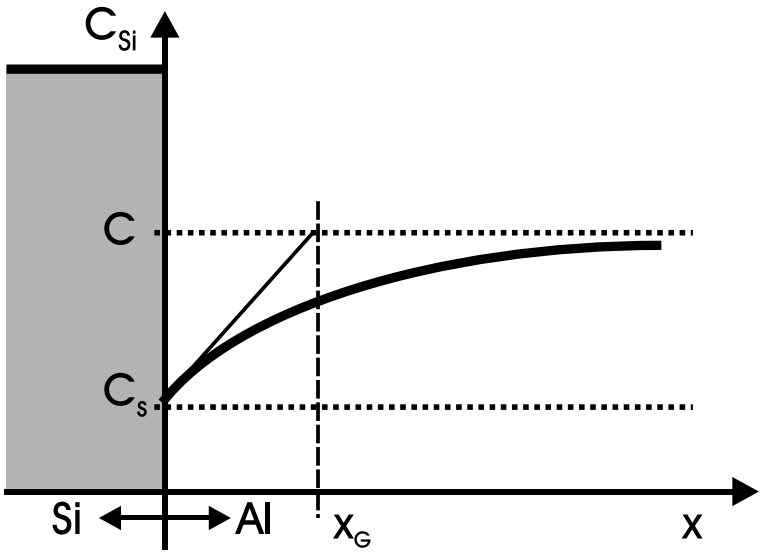


**Figure 5.3:** Si concentration in front of a growing Si grain in diffusion-limited growth. At the grain the $C_{Si}$ is the saturation concentration $C_S$. A concentration gradient is formed which reaches a maximum concentration $C$ far away from the grain. Si diffuses along this gradient towards the growing grain. The slope at the grain is determined by the growth length $x_G$.

homogeneous nucleation is assumed and the stress effect is neglected. For the presented, qualitative discussion this assumption is not of crucial importance.

The density of critical cluster $C^{**}$ is given by:

$$C^{**} \propto C \exp\left(-\frac{\Delta G^*}{kT}\right), \tag{5.10}$$

where $C$ is the concentration of the nucleating species and $\Delta G^*$ is the activation energy for the nucleation. The rate $f$ at which the nuclei stabilize, i.e. reach the supercritical size, depends on how frequently a critical nucleus can receive an atom. This depends on the surface area of the nucleus and the rate at which diffusion can occur. If the activation energy for atomic migration is $\Delta G_m$ per atom, $f$ can be written as:

$$f = \omega \exp\left(-\frac{\Delta G_m}{kT}\right), \tag{5.11}$$

where $\omega$ is a factor that includes the vibration frequency of the atoms and the area of the critical nucleus. The nucleation rate is the product of $f$ and $C^{**}$, therefore

$$j_N \propto \omega C \exp\left(-\frac{\Delta G_m}{kT}\right) \exp\left(-\frac{\Delta G^*}{kT}\right). \tag{5.12}$$

The Gibbs energy $\Delta G^*$ needed to form a critical cluster, i.e. the activation energy, is known to depend on the crystallization heat and the surface energy as shown in equation 2.4 [12]:

$$\Delta G^* = \frac{16}{3}\pi\frac{\sigma^3}{\Delta g_V^2}, \tag{5.13}$$

for spherical cluster, $\sigma$ is the specific surface energy and $\Delta g_V$ is the Gibbs energy reduction by transition of an atom. In the Al layer the Gibbs energy reduction by transition of an atom corresponds to the difference of the chemical potential of the atom in the Al to the chemical potential in the cluster. Thus $\Delta g_V$ can be substituted by $\Delta\mu_{Si}$ in case of the ALILE process. In eq. 5.2 the concentration dependence of the chemical potential of Si $\mu_{Si}$ in Al is shown. The chemical potential of the silicon in the cluster is $\mu_{Si,0}$. Thus the chemical potential difference $\Delta\mu_{Si}$ is:

$$\Delta\mu_{Si} = kT\ln\left(\frac{C}{C_S}\right) \tag{5.14}$$

$$= kT\ln S. \tag{5.15}$$

Combining equations 5.12, 2.4 and 5.15 and substituting $C = C_S S$ leads to a concentration dependent formula for the nucleation rate

$$j_N \propto \omega C_S S \exp\left(-\frac{\Delta G_m}{kT}\right) \exp\left(-\frac{16\pi\sigma^3}{3(kT)^3\ln^2 S}\right) \tag{5.16}$$

In Fig. 5.4 both nucleation and growth rate are plotted as a function of the supersaturation $S$. All values other than $S$ were set to $1$ in order to plot the functions.

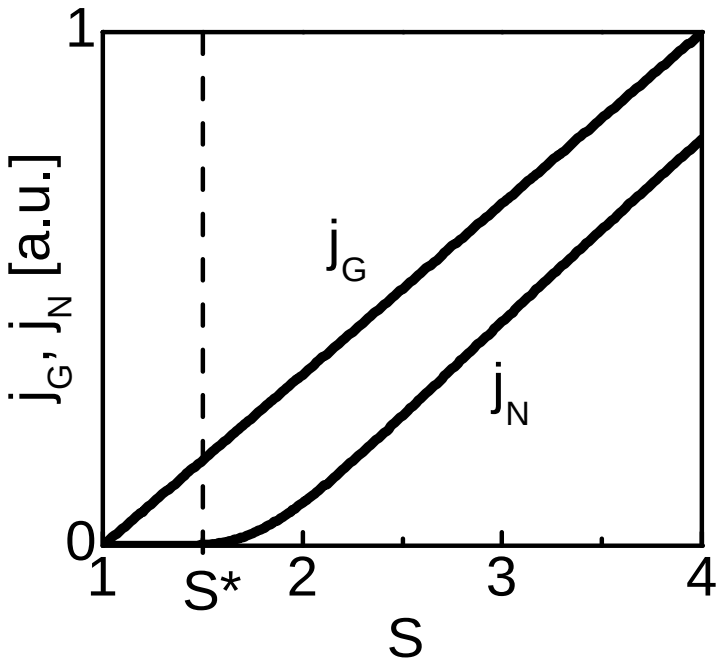


**Figure 5.4:** Nucleation rate $j_N$ and growth rate $j_G$ as a function of the supersaturation $S$. Up to the nucleation concentration $C^*$ the nucleation rate is about zero.

In contrast to the growth rate, the nucleation rate remains close to zero up to a supersaturation of about $S^* = C^*/C_S = 1.5$ (This value varies when the nucleation rate is calculated with real values in equation 5.16, but the tendency remains). This means that there is a regime where growth is possible, but no nucleation is observed indicated by a dashed line in Fig. 5.4. The Si concentration corresponding to this supersaturation is referred to as critical or nucleation concentration $C^*$. Upon exceeding $S^*$ the nucleation rate $j_N$ is dominated by the linear coefficient.

Now, three important Si concentrations have been defined. No growth or nucleation takes place at concentrations below the saturation concentration $C_S$. When $C_S$ is exceeded a regime without nucleation but crystal growth has been defined. Upon reaching the critical concentration $C^*$ the nucleation rate increases. The maximum concentration $C_{max}$ can not be exceeded in the process.

**I:** $0 \leq C < C_S$: no nucleation, no grain growth.

**II:** $C_S \leq C < C^*$: no nucleation, but grain growth.

**III:** $C^* \leq C < C_{max}$: both, nucleation and grain growth.

The three regimes and the the corresponding Si concentrations are very important for understanding the ALILE process and are used in the following sections.

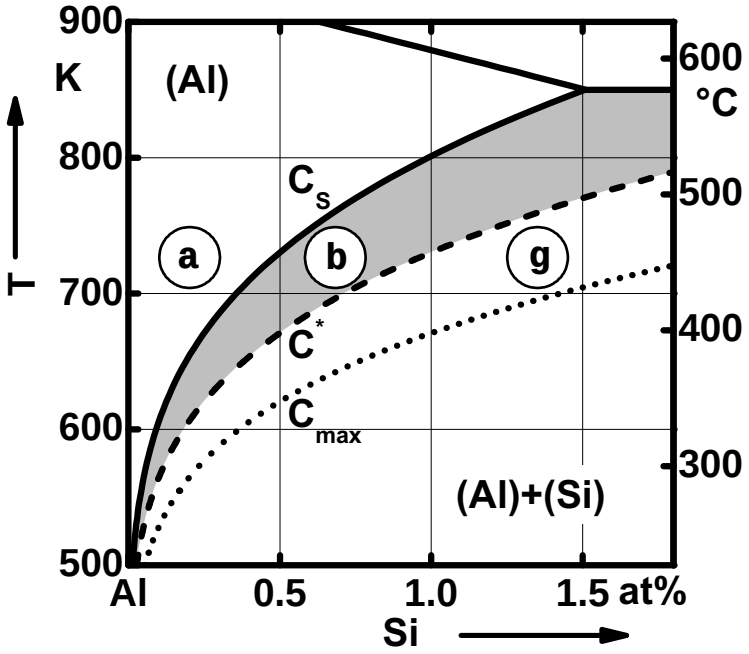


**Figure 5.5:** Al rich part of the modified Al/Si phase diagram including the three concentrations: saturation concentration $C_S$ (solid line), critical concentration $C^*$ (dashed line) and maximum concentration $C_{max}$ (dotted line).

## 5.2 The ALILE process in the phase diagram

The ALILE process takes place in the Al rich part of the Al/Si phase diagram. Using the above defined Si concentrations the phase diagram is modified.

In the 'normal' Al/Si phase diagram the saturation concentration is shown. The critical concentration and the maximum concentration are higher than the saturation concentration. Corresponding lines are added in the phase diagram (Fig. 5.5). The critical concentration $C^*$ (dashed line) was estimated to be around $1.5\times$ (Fig. 5.4) the saturation concentration $C_S$ (solid line) and the maximum concentration $C_{max}$ (dotted line) is about $4\times$ as high (eqn. 5.6). Consequently the three concentration regimes (I-III) explained above can be distinguished. The regime (II) without nucleation but grain growth is shaded in grey, because it is of special importance to the nucleation suppression.

Fig. 5.5 enables a discussion of the time evolution of the silicon concentration $C_{Si}$ in the Al layer far away of the growing grains. The importance of the Si

concentration close to the grain is discussed later. In Fig. 5.6(a) the modified phase diagram and in Fig. 5.6(b) the Si concentration $C_{Si}$ versus the annealing time $t_A$ are shown. At the beginning of the process there is no silicon within the aluminum layer. Provided that the heating is fast compared to the Si diffusion the Si concentration remains zero until the sample reaches the annealing temperature (1). The system tries to reach the thermodynamic equilibrium, i.e. the equilibrium line. Therefore silicon diffuses from the a-Si phase into the Al, increasing the Si concentration $C_{Si}$ from zero to the saturation concentration $C_S$ (2). Due to the higher chemical potential of the silicon within the a-Si phase the Al will be supersaturated, still no new nucleation is observed. Upon exceeding the critical concentration $C^*$ (3), nucleation starts and the grains begin to grow supplied by lateral diffusion of silicon atoms from the Al layer. The increasing number of silicon nuclei and their growth reduces the increase in silicon concentration within the Al layer and the silicon concentration reaches a maximum (4). When the Si concentration reaches a maximum the nucleation rate reaches a maximum, too. When the growth of the silicon grains and the formation of new nuclei consumes more silicon than the supply of silicon from the a-Si phase, $C_{Si}$ decreases until it drops below the critical concentration again and nucleation comes to an end (5). The growth rate of the silicon grains is proportional to the difference between $C_{Si}$ and $C_S$. Thus the growing grains are not able to decrease the Si concentration below the saturation concentration and thus $C_{Si}$ finally reaches a value between $C^*$ and $C_S$ (6).

The Si concentration $C_{Si}$ evolution in Fig. 5.6(b) shows that the process can be divided in three periods:

**I:** *saturation period*: No nucleation takes place until the critical concentration $C^*$ is reached at $t_1$.

**II:** *nucleation period*: Si nucleates and the nuclei grow.

**III:** *growth period*: When the Si concentration drops below the critical concentration again and nucleation comes to and end.

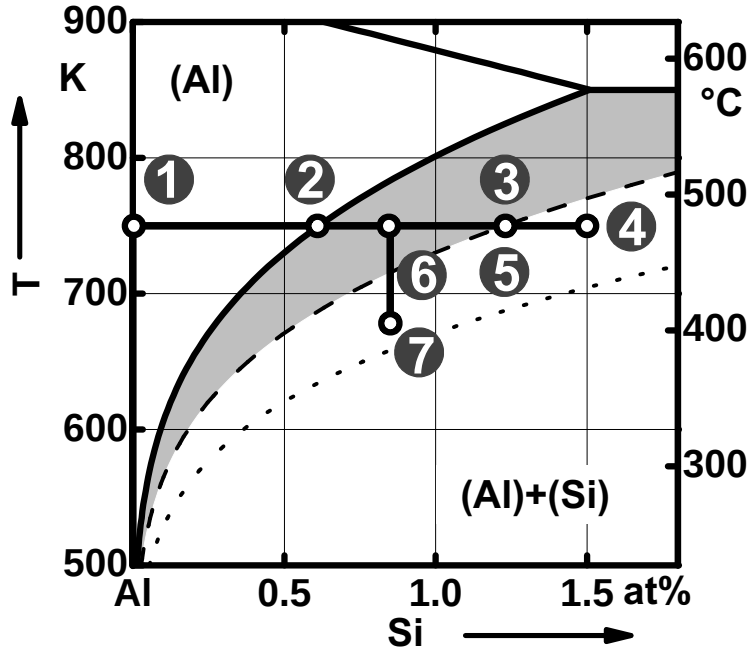


(a)

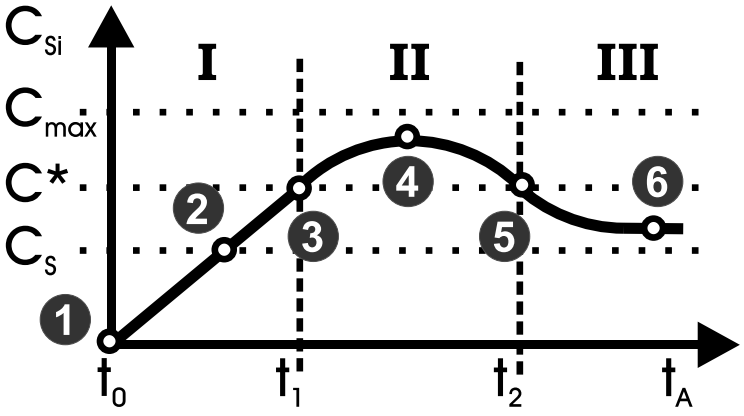


(b)

**Figure 5.6:** Model for the ALILE process. (a) Modified Al/Si phase diagram with process steps and correspondingly (b) the time evolution of the Si concentration during the ALILE process. The three concentrations: maximum concentration $C_{max}$, critical concentration $C^*$ and saturation concentration $C_S$ play a crucial role in the process and divide it in three regimes: I: no nucleation, II: nucleation and growth of the grains, III: grain growth without further nucleation.

These three periods correspond to the experimental results described in chapter 4 shown in Fig. 4.11. Thus the mechanism responsible for the suppression of nucleation can be understood.

With this model the cooling results discussed in chapter 4.2.2 can be explained as well. When the temperature is lowered the saturation concentration decreases and thus the supersaturation is increased strongly (7) (Fig. 5.6(a)). This leads to a strong increase in the nucleation rate. Upon reheating the sample the formed nuclei grow and become visible in the optical micrographs. The existence of the depletion regions will be addressed in the following section.

## 5.3 Depletion regions in the ALILE process

The nucleation suppression can be explained by the thermodynamic considerations and the phase diagram. The considerations were made involving the time evolution of the Si concentration somewhere in the Al or to be more precise somewhere far away of the grain in the bulk of the Al. The origin of the depletion regions found in the cooling step experiments (section 4.2.2) is elucidated in this section.

In Fig. 5.7 the Si concentration around an existing grain is shown schematically before (a) and after (b) cool down (compare to Fig. 5.7(a) and 5.7(b)) assuming ideal diffusion limited growth as mentioned above. Critical concentrations $C^*$ and saturation concentrations $C_S$ are marked with corresponding indices a (before cool down) and b (after cool down). In the shown cases the sample reached the *growth period* prior to cool down. Thus the silicon concentration $C_{Si}$ is above the saturation concentration $C_{S,a}$ and below the critical concentration $C_a^*$ within the entire Al layer allowing for growth of existing grains but suppressing new nucleation (regime I) (Fig. 5.7(a)). Assuming the cool down to be very fast in comparison to diffusion, the concentration profile does not change from Fig. 5.7(a) to Fig. 5.7(b). But upon cool down the saturation concentration is decreased from $C_{S,a}$ to $C_{S,b}$ according to the Al-Si phase diagram [98]. At the same time the critical concentration is decreased from $C_a^*$ to $C_b^*$ because the critical supersaturation remains the same ($S^* = C_a^*/C_{S,a} = C_b^*/C_{S,b}$). For comparison the saturation concentration $C_{S,a}$ and the critical concentration $C_a^*$ before the cool down are included in Fig. 5.7(b) (indicated by dotted lines). Due to the decrease of the critical concentration upon cool down the Si concentration within the Al layer far away from existing grains exceeds the critical concentration $C_b^*$ (regime II). Thus many new grains are formed as observed in the experiment (Fig. 5.7(b)). In the vicinity of existing grains $C_{Si}$ is still below $C_b^*$ and therefore no new nucleation occurs in these regions (regime I). These regions are the depletion regions. The width of the depletion region $L$ is indicated in Fig. 5.7(b) (compare regions without new

nuclei around preexisting grains in section. 4.2.2). Due to the steep increase in nucleation rate at the critical concentration $C_b^*$ the nucleation density rises abruptly from zero inside the depletion regions to a high value outside the depletion regions.

This model is compared with the experimental data obtained in chapter 4 in the next section in order to verify it.

## 5.4 Comparison of the qualitative model with experimental results

The results obtained in section 4.1.1 are elucidated in the context of the model described in the previous section in order to verify the model. The results presented in section 4.1.1 are normalized as described below to analyze them in context of the model presented above.

Fig. 5.8 shows the normalized grain growth velocity $v_{G,0}$ (open circles), nucleation density $N_G$ (crosses) and nucleation time $t_N$ (solid squares) for sample type C annealed at various temperatures. The values have been normalized to the results at the lowest annealing temperature. With increasing annealing temperature the grain growth velocity $v_{G,0}$ increases whereas nucleation time $t_N$ decreases and the nucleation density $N_G$ is only little affected.

Fig. 5.9 shows the result for the different samples annealed at $450\,$°C. Again the values have been normalized. This time to the corresponding values of sample type A. The nucleation time $t_N$ increases, the nucleation density $N_G$ decreases and the change in $v_{G,0}$ is relatively small when the oxide layer thickness is increased from sample A to C.

These results are interpreted using the basic model shown in Fig. 5.1 and the thermodynamic consideration made thereafter. The two main Si fluxes correspond to the process step (1) total Si diffusion from the a-Si across the interface into the Al

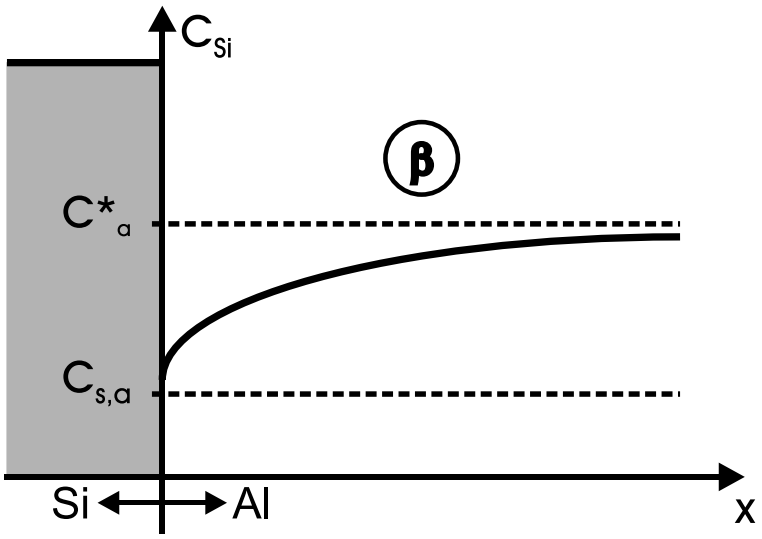


(a)

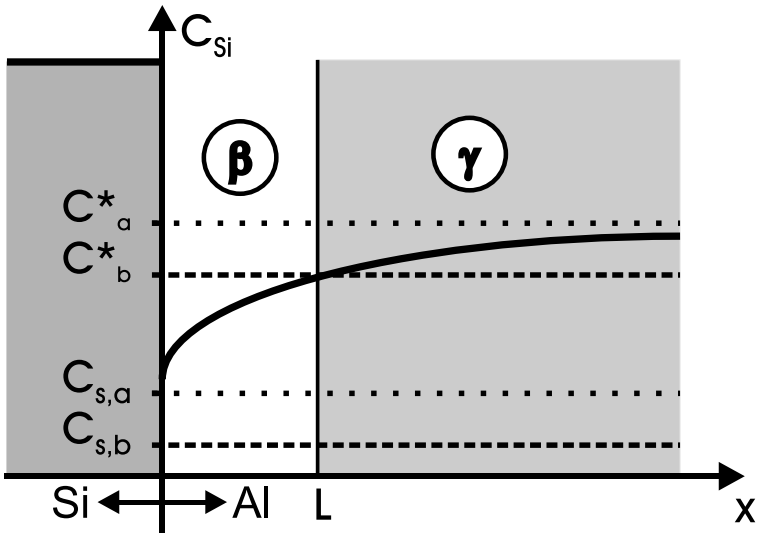


(b)

**Figure 5.7:** Schematic illustration of the silicon concentration $C_{Si}$ in front of a growing grain vs distance $x$ from the grain before (a) and after (b) cool down. Critical concentration $C^*$ and saturation concentration $C_S$ are shown with the corresponding indices. The transition from subcritical ($\beta$) to supercritical ($\gamma$) phase at the depletion region width $L$ is indicated in (b).

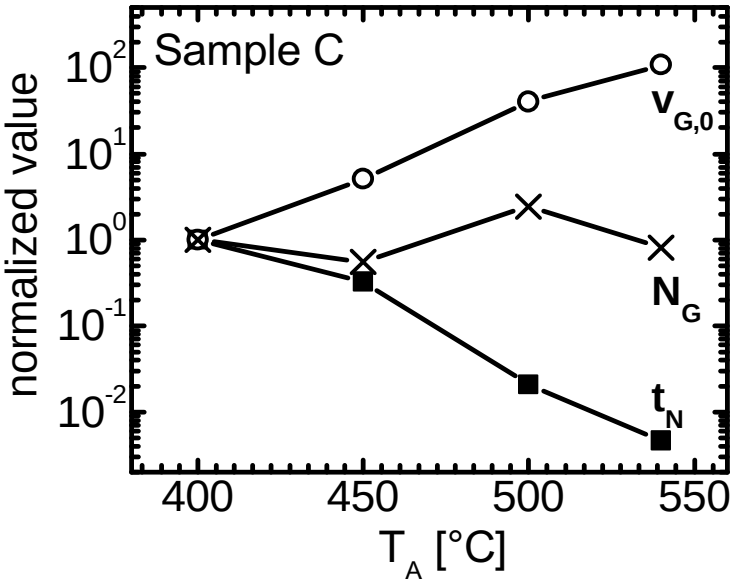


**Figure 5.8:** Values normalized to the value at $400\,°C$: average grain growth velocity $v_{G,0}$ (open circles), nucleation density $N_G$ (crosses) and nucleation time $t_N$ (solid squares) vs. annealing temperature $T_A$ for sample type C.

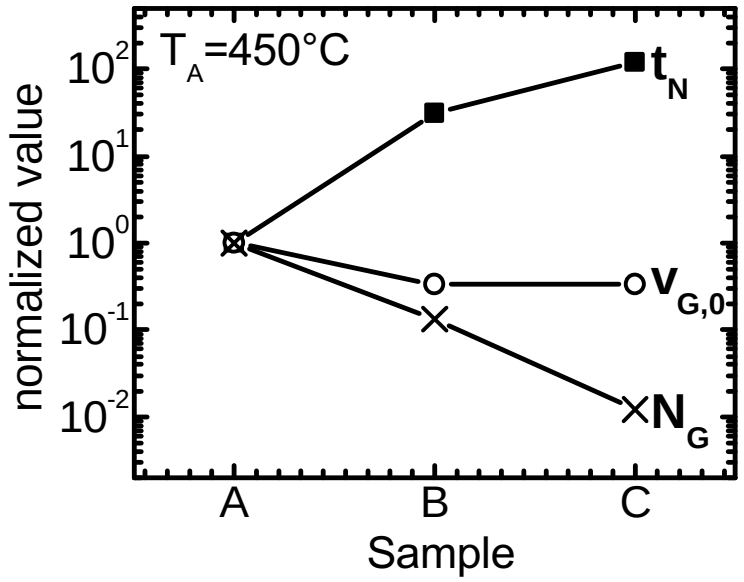


**Figure 5.9:** Values normalized to the value for sample type $A$: nucleation time $t_N$ (solid squares), average grain growth velocity $v_{G,0}$ (open circles) and number of grains $N_G$ (crosses) for all three sample types A, B and C annealed at $450\,°C$.

layer $J_1$ and (2) Si diffusion within the Al layer towards a single growing grains $J_2$.

The total flux $J_1$ across the interface determines the time needed to reach the critical concentration $C^*$ in the Al layer. The higher $J_1$ the lower the nucleation time $t_N$:

$$t_N \sim \frac{1}{J_1}. \tag{5.17}$$

The ALILE process is a diffusion limited process. This means that the amount of silicon aggregated at the grain and thus $v_{G,0}$ is mostly determined by the diffusion velocity, i.e. the flux $J_2$ of silicon within the aluminum layer towards a single grain (2). The higher the silicon diffusion velocity within the aluminum the faster the crystalline silicon grains grow:

$$v_G \sim J_2. \tag{5.18}$$

After the nucleation started the silicon diffuses across the interface and within the aluminum layer towards the grains. As long as the silicon flux across the interface is larger than the sum of silicon fluxes towards the growing grains the silicon concentration within the aluminum will rise. And thus new silicon nuclei are formed in the aluminum. In first approximation the nucleation stops when both diffusion processes are equal and the final nucleation density $N_G$ is reached[1].

$$J_1 = N_G J_2 \tag{5.19}$$

$$\Rightarrow N_G = \frac{J_1}{J_2} \tag{5.20}$$

[1]Actually the Si concentration only starts to decrease once the $N_G J_2$ is larger than $J_1$, but the nucleation stops only when the Si concentration $C_{Si}$ decreases below the critical concentration $C^*$. Still for the simple evaluations made here, the result is not affected.

This means that the number of grains is determined by the ratio of the two fluxes. At the beginning of the process the flux across the interface $J_1$ is larger than the flux to the growing grains $J_2$ ($J_1 > N_G J_2$) and the silicon concentration within the aluminum layer still increases. After reaching the point were both fluxes are equal the diffusion towards the grains is larger than the flux across the interface $J_1 < N_G J_2$ which leads to a lower concentration of silicon in the aluminum layer. Applying these considerations to the experiments described above the influence of the different parameters on the different process steps has to be taken into account. With increasing annealing temperature $T_A$ both $J_1$ and $J_2$ increase (eq. 5.21). An increase of $J_1$ leads to a decrease of the nucleation time $t_N$ (eq. 5.17). An increase of $J_2$ leads to an increase of the grain growth velocity $v_{G,0}$ (eq. 5.18). The nucleation density $N_G$ remains approximately constant (eq. 5.20).:

$$
\begin{aligned}
T_A \uparrow: & \qquad (5.21)\\
J_1 \uparrow \quad &\Rightarrow \quad t_N \downarrow \\
J_2 \uparrow \quad &\Rightarrow \quad v_{G,0} \uparrow \\
\frac{J_1}{J_2} \approx const. \quad &\Rightarrow \quad N_G \approx const.
\end{aligned}
$$

Both fluxes $J_1$ and $J_2$ are thermally activated processes. This means that the nucleation density $N_G$ is only affected by the difference in thermal activation energy of both processes (Fig. 5.8).

The oxide layer thickness will change the diffusion across the interface but will have little effect on the diffusion within the aluminum layer. This means that $t_N$ will increase with increasing oxide thickness (eq. 5.17) and $v_{G,0}$ will be little affected (eq. 5.18). The ratio of both processes is strongly changed by the oxide layer thickness. This means that the nucleation density $N_G$ decreases with increasing oxide layer thickness (eq. 5.20). This has been experimentally observed in Fig. 5.9:

$$
\begin{aligned}
d_{Ox} \uparrow: & \qquad (5.22)\\
J_1 \downarrow \quad &\Rightarrow \quad t_N \uparrow \\
J_2 \approx const. \quad &\Rightarrow \quad v_G \approx const. \\
\frac{J_1}{J_2} \downarrow \quad &\Rightarrow \quad N \downarrow
\end{aligned}
$$

This basic model is very restricted, because all parameters influence each other. All process steps are linked by the silicon concentration within the aluminum layer. With increasing silicon concentration within the aluminum layer the silicon diffusion into the aluminum will decrease and the grain growth velocity and nucleation rate will increase . However, the simple picture presented here allows a qualitative interpretation of the role of the various parameters in the ALILE process.

## 5.5 Preferential orientation model

The temperature dependence of the preferential orientation was reported first by Kim et al. [67]. In section 4.1.1 this temperature dependence is confirmed and an additional dependence on the interface layer is shown. The present section offers a possible explanation in particular of the following experimental observations:

- there are more grains close to $\{100\}$ than to $\{111\}$ and $\{110\}$-orientation,
- the orientation depends on the annealing temperature, lower annealing temperature increases the fraction of $\{100\}$ orientated grains.
- the orientation depends on the interlayer, native oxide increases the fraction of $\{100\}$ orientated grains compared to thermal oxide

Some general assumptions have to be made. No relation between grain size and orientation has been detected so far. In the experiments observed in the optical microscope the grain growth velocity for all grains in the same experiment were similar (see section 4.1). Thus it is concluded that the formation of the preferential orientation is not due to the faster growth of grains with a certain orientation. Instead it is assumed that the formation of the critical cluster determines the preferential orientation of the film.

In order to lead to a preferential orientation the critical cluster needs two properties:

**1:** the cluster itself must have a preferential orientation.

**2:** the cluster must be aligned to a feature with reference to the surface normal.

Recalling the section on critical cluster formation in chapter 2, the Gibbs energy change in the formation of a critical cluster is:

$$\Delta G_i = -\Delta g_V i + \sigma O_i, \tag{5.23}$$

the sum of a negative volume ($-\Delta g_V i$), product of the crystallization heat $g_V$ per atom and the number of atoms $i$ in the cluster, and a positive surface ($\sigma O_i$) dependent energy, product of the specific surface energy $\sigma$ per atom and the number of atoms at the surface $O_i$. The surface dependent term which acts against the formation of the critical cluster can be reduced by either heterogeneous nucleation or formation of preferential surfaces. In the diamond structure of crystalline silicon $\{111\}$ faces have the lowest specific surface energy $\sigma$ and thus are preferentially formed [99]. The result is an octahedral or double-pyramid structure of the critical clusters as shown in Fig. 2.6. The double pyramid has $\{111\}$ faces, $\langle 110\rangle$ ledges and $\langle 100\rangle$ tips. Thus the clusters are preferentially orientated and fulfill the first requirement for the preferential orientation formed through nucleation. From this point all clusters are assumed to form $\{111\}$ faces only.

The specific surface energy $\sigma$ can also be reduced by nucleation at a preferential site. If the nucleation takes place at a pre-existing interface, $\sigma$ is strongly reduced. This is referred to as heterogeneous nucleation. In the Al layer the grain boundaries and the interfaces to the glass and the oxide layer are suitable structures for heterogeneous nucleation. All of these are aligned to the surface normal. It seems reasonable that the most likely nucleation sites are the points where three Al grains meet the interlayer. Here the density of interfaces is the highest. These sites are aligned and thus fulfill the second requirement. With both requirements achieved the preferentially orientated clusters have to be stuck to the interface at preferential sites in a defined and favorable manner in order to result in a preferential orientation.

In Fig. 5.10 two TEM cross sections are shown of a specimen which has been annealed very briefly and then cooled down rapidly. In Fig. 5.10(a) the TEM image shows the glass at the bottom with the bright Al layer and the a-Si layer on top. In the Al layer a quadrangle can be anticipated. A schematic drawing is placed on top to illustrate the double pyramid cluster shape. In Fig. 5.10(b) a diffraction contrast of the cluster is shown. The corresponding diffraction analysis of this quadrangle reveals that it is a silicon crystallite aligned with its $[21\bar{1}]$ direction

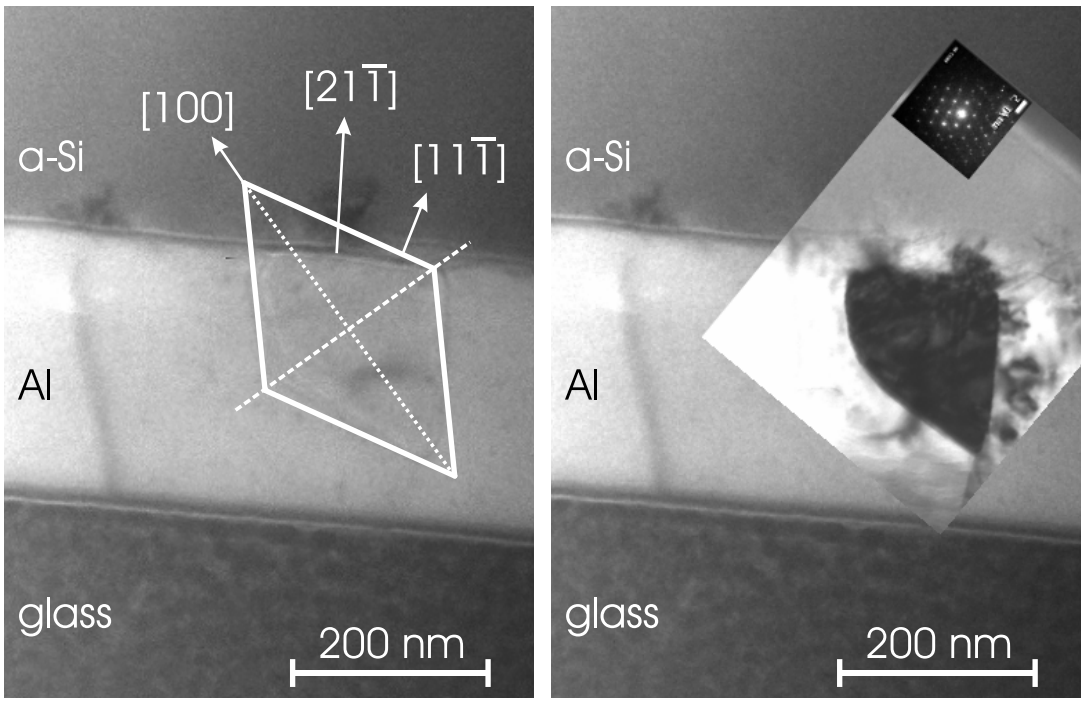


(a) (b)

**Figure 5.10:** TEM cross section of a glass/Al/a-Si layer stack after a very short annealing step. (a) Preferentially shaped cluster at interface. The schematic structure is placed on top of the actual grain which can be seen in (b) the corresponding z-contrast micrograph with a diffraction pattern identifying silicon grain with $[21\bar{1}]$ orientation normal to layer surface.

normal to the oxide layer. A double pyramid cluster is inserted in the Fig. 5.10(a) to elucidate the idea of 'sticking' an orientated cluster to the interface. The $[21\bar{1}]$ direction is in between the $[11\bar{1}]$ face and the $[100]$ tip of the pyramid. The cluster is not perfectly aligned but tilted with respect to the $[100]$ orientation and already much larger than the critical cluster size, which is expected to be of the size of about 45 atoms as determined by Spinella et al. in the case of solid phase crystallization of amorphous silicon [12]. Still the formation of a double pyramid can be anticipated.

The shape of the critical cluster is assumed to only exhibit $\{111\}$ orientated surfaces and to be intersected by the oxide layer. These requirements can not only be fulfilled by a double pyramid, but much rather by a single pyramid. The tip of this

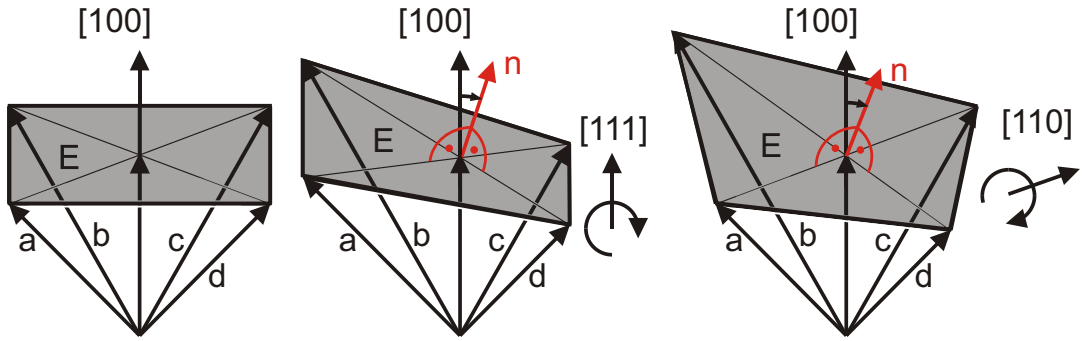


(a) (b) (c)

**Figure 5.11:** Sketch of a tilted single pyramid. The normal vector $n$ of the intersecting plane $E$ as well as the four edge vectors of the pyramid $a, b, c, d$ used in the calculations below are indicated. (a) Initial position with $(100)$ tip normal to the interface. (b) Tilted towards $(111)$ direction by $\alpha_{111}$. (c) Tilted towards $(110)$ direction by $\alpha_{110}$.

single pyramid can be tilted relative to the interface. If the pyramid is pointing straight down, the resulting grain is $\{100\}$ orientated. If the tip is tilted one way or the other the resulting grain orientation changes accordingly.

With these assumptions an analytic solution for the angular and size dependant Gibbs energy is derived in the following. A coordinate system is introduced with the pyramid shape being unchange and only the interlayer plane being altered in its distance from the origin and its tilting angle with respect to the $[100]$ axis/orientation. The tip of the pyramid is the origin of the coordinated system. The tip of the single pyramid $[100]$ direction always points in the $[100]$ direction of the coordinate system. And the ledges of the pyramid are vectors from the origin in the four directions $[110]$, $[101]$, $\left[1\bar{1}0\right]$ and $\left[10\bar{1}\right]$ (see Fig. 5.11(a)). The interface plane intersects the pyramid at a height $h$, i.e. at $(h00)$ and its normal vector is tilted relative to the $[100]$ direction by the angle $\alpha_{111}$ towards $[111]$ direction (see Fig. 5.11(b)), or by the angle $\alpha_{110}$ towards the $[110]$ direction (see Fig. 5.11(c)). The intersections of the four ledges vectors with the interface plane together with the origin are the five corners of the tilted pyramid.

As a result the *volume* of the cluster, the *surface* area formed with the surrounding Al and the *base* area formed with the interlayer are calculated (for detailed calcu-

lations see Appendix A). The resulting size $i$ in atoms and angular $\alpha_{110}$ and $\alpha_{111}$ dependent Gibbs energy for the two tilt angles are:

$$\begin{aligned}\Delta G\left(i,\alpha_{110}\right) &= -\Delta g_V\, i \\ &\quad + \Bigg( \sigma_{Al,Si}\, 2^{\frac{1}{3}}\, 3^{\frac{7}{6}} \frac{\left(\cos\alpha_{110}\right)^{\frac{2}{3}}}{\cos^{\frac{1}{3}}\left(2\,\alpha_{110}\right)} \\ &\quad + \sigma_{AlO_X,Si}\, 2^{\frac{1}{3}}\, 3^{\frac{2}{3}} \frac{1}{\cos\alpha_{110}\cos\left(2\,\alpha_{110}\right)} \Bigg) i^{\frac{2}{3}} \end{aligned} \tag{5.24}$$

and

$$\begin{aligned}\Delta G\left(i,\alpha_{111}\right) &= -\Delta g_V\, i \\ &\quad + \Bigg( \sigma_{Al,Si}\, 2^{\frac{5}{3}}\, 3^{\frac{7}{6}} \frac{\cos^{\frac{4}{3}}\alpha_{111}}{\left(1+3\cos\left(2\,\alpha_{111}\right)\right)^{\frac{2}{3}}} \\ &\quad + \sigma_{AlO_X,Si}\, 2^{\frac{5}{3}}\, 3^{\frac{2}{3}} \frac{\cos^{\frac{1}{3}}\alpha_{111}}{\left(1+3\cos\left(2\,\alpha_{111}\right)\right)^{\frac{2}{3}}} \Bigg) i^{\frac{2}{3}}, \end{aligned} \tag{5.25}$$

respectively.

The critical cluster size $i^*$ and the activation energy $\Delta G^*$ can be calculated as shown in chapter 2. It is clear that both critical cluster size $i^*$ and the activation energy $\Delta G^*$ not only depend on the tilt angles but also on the Gibbs energy per nucleated cluster $\Delta g_V$ and the surface energies between Al and Si $\sigma_{Al,Si}$ and between Si and $AlO_X$ aluminum oxide $\sigma_{AlO_X,Si}$. From Spinella et al. [12] the corresponding energies in solid phase crystallization are known. The crystallization energy $\Delta g_V$ and the a-Si/c-Si interface energy $\sigma_{ca}$ are in the order of 0.1 eV/ atom. Even though the values for the aluminum-induced crystallization of amorphous silicon are expected to be different from these values, they are used as first approximation. At the oxide/cluster interface one half of the interface- namely the oxide- already exists. Thus the $\sigma_{AlO_X,Si}$ is assumed to be only half of $\sigma_{Al,Si}$. The resulting Gibbs energy $\Delta G$ is plotted as a function of the tilt angles $\alpha$ and the cluster size $i$ in Fig. 5.12. Clearly a saddle point is formed at $\alpha = 0°$. Especially tilt angles far away from the $(100)$ direction have much higher activation energies compared to $(100)$.

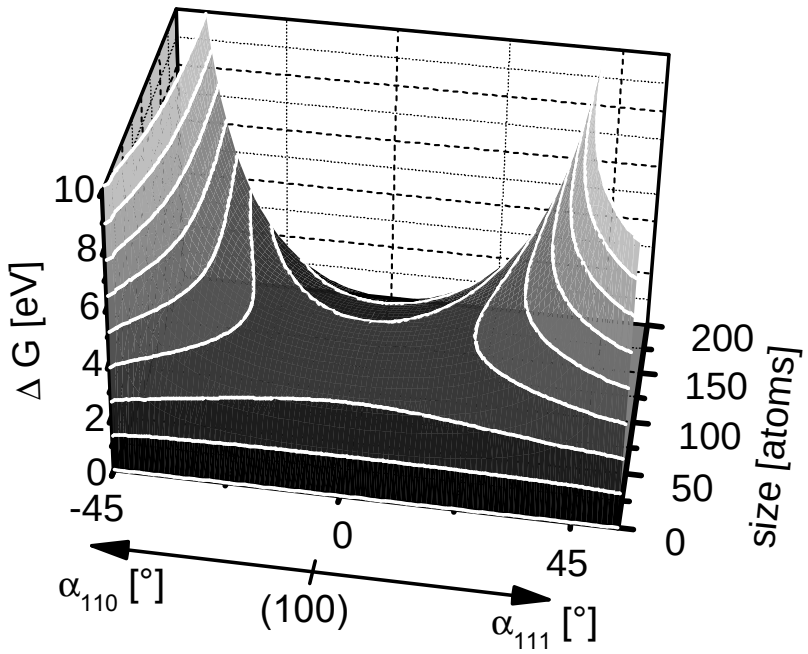


**Figure 5.12:** Gibbs energy $\Delta G$ for different tilt angles $\alpha$ from $(100)$ to (110) and $(111)$ as a function of the cluster size.

The resulting, angular dependent, nucleation activation energy $\Delta G^*$ is the maximum for the different angles at the critical cluster size $i^*$ and can be easily calculated by setting the derivative with respect to the cluster size $i$ to zero. Substituting the parenthesis in equations 5.24 and 5.25 by $X\left(\alpha\right)$ the results for both tilt angles are:

$$\frac{\partial \Delta G}{\partial i} = -\Delta g_V + \frac{2}{3} X\left(\alpha\right) i^{-\frac{1}{3}} = 0 \tag{5.26}$$

$$\Rightarrow i^* = \left(\frac{2}{3}\frac{X\left(\alpha\right)}{\Delta g_V}\right)^3 \tag{5.27}$$

$$\Rightarrow \Delta G^* = -\Delta g_V \left(\frac{2}{3}\frac{X\left(\alpha\right)}{\Delta g_V}\right)^3 + X\left(\alpha\right)\left(\frac{2}{3}\frac{X\left(\alpha\right)}{\Delta g_V}\right)^2 \tag{5.28}$$

$$= \frac{4}{27}\frac{X\left(\alpha\right)^3}{\Delta g_V^2} \tag{5.29}$$

The result is shown in Fig. 5.13. Not only the activation energy $\Delta G^*$ increases for larger tilt angles $\alpha$ but also the critical cluster size $i^*$. This leads to an even lower nucleation rate, because more atoms have to jump onto the cluster before a critical cluster can be formed.

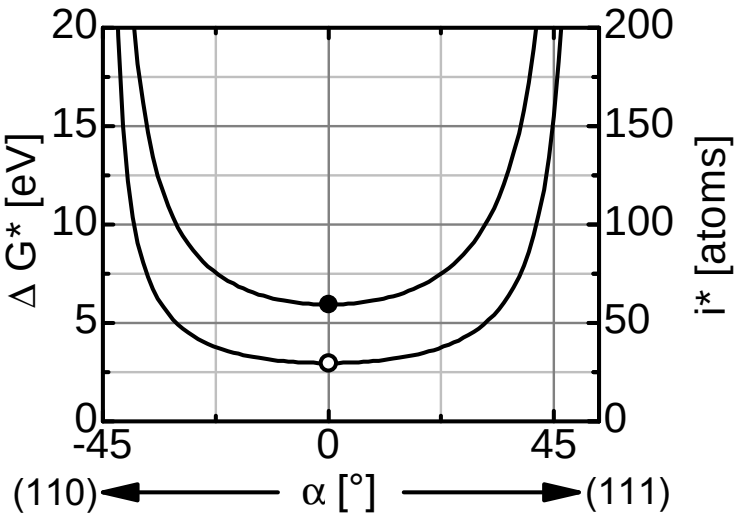


**Figure 5.13:** Calculated nucleation Gibbs energy $\Delta G^*$ (open circle) and critical cluster size $i^*$ (solid circle) as a function of the tilt angle $\alpha$ from $(100)$ towards $(110)$ and $(111)$ orientation.

With this model the temperature dependence of the preferential orientation can be understood. The rates of thermally activated processes are higher for lower than for higher activation energies at lower temperatures. Thus at low annealing temperatures mainly $(100)$ oriented clusters are formed. At higher annealing temperatures the nucleation rates for clusters with tilted orientations increases and cluster with other orientations stabilize as well.

An alternative way to visualize this is referred to as *nucleation attempt* model. The critical clusters are formed from statistical agglomerations of atoms. When the initial, subcritical cluster is formed the tilt angle is already determined. Thus in Fig. 5.12 the position at the angle dependant axis is already determined and will not change throughout the attempt of the cluster to reach the critical size. The subcritical cluster agglomerates atoms and attempts to overcome the energy barrier at the maximum of $\Delta G$. Especially if the (thermal) energy of the system is low it is much more likely for the subcritical cluster to overcome the energy barrier close to the $(100)$ orientation.

Using this model an idea for the interlayer dependance of the orientation of the resulting layer can be given with a little more information on aluminum oxide.

Native oxide is amorphous but at temperatures above $450\,°C$ a so called $\gamma - Al_2O_3$ phase is formed which is crystalline [100]. This structural change of the oxide layer much rather than the change in thickness is suggested to be the origin of the shift in preferential orientation with thermal oxide interlayers. Keeping the *nucleation attempt* model in mind, the amorphous oxide does probably not influence the number of attempts of any tilt angle. But the crystalline interface can offer defined bonds for the initial, subcritical cluster. And even though it is still a statistical process the number of nucleation attempts of a certain cluster orientation can be increased. The temperature dependance is not changed, but especially at high temperatures when the clusters of all types of orientations reach the critical cluster size the number of attempts can determine the final orientation of the film. This suggests that the thermal oxide ($\gamma Al_2O_3$) increases the number of nucleation attempts close to the $(111)$ orientation.

In this chapter the layer exchange process is discussed. It is shown that the Si concentration within the Al is crucial for nucleation and growth. Below the saturation concentration $C_S$ neither nucleation nor growth of existing grains is possible. At concentrations larger than $C_S$ but below the critical concentration $C^*$ grains grow but no new nuclei are formed. Only when $C^*$ is exceeded nucleation is observed. The higher the concentration the higher the growth and nucleation rate. But the concentration is shown to be limited to a maximum concentration $C_{max}$. The self-limited suppression of nucleation is elucidated for the ALILE process by showing the time dependence of the Si concentration within an Al/Si phase diagram including the above defined concentrations. Evaluation of the experimental results against the background of the model demonstrates the validity of the presented considerations in very simple qualitative terms. Furthermore a model for the origin of the preferential orientation elucidating both the temperature and interlayer dependence of the resulting poly-Si film is suggested. The formation of preferentially shaped clusters aligned at preferential nucleation sites is suggested to result in the observed preferential orientation.

# 6 Conclusions

In the aluminum-induced layer exchange process a glass/Al/a-Si layer stack is transformed into a glass/poly-Si/Al(+Si) layer stack in a simple thermal annealing step. The poly-Si layer is characterized by

- large grains, promising good electronic properties and
- preferential (100) orientation, desirable for subsequent low-temperature epitaxy.

Both attributes were known prior to this work, but their origin was not fully understood. A model was suggested for the origin of the large grains earlier. Within this thesis its validity is proofed experimentally. The origin of the preferential orientation was not discussed before and a possible explanation is given within this thesis for the first time.

By designing special experiments it is possible to elucidate the origin of both phenomena. The results are discussed on a thermodynamic basis using the Al/Si phase diagram. Nucleation and growth rates depend on the supersaturation of Si in the Al. Through supercooling additional nucleation is enforced proofing the suggested model. Self-limiting suppression of nucleation leads to very large grain sizes.

The selective formation of critical clusters leads to a preferential nucleation of Si. The initial preferential nucleation causes a final preferential orientation of the films. This model is consistent with experimental findings.

The discussion of the results makes the aluminum-induced layer exchange process very enlightening, revealing the physics of phase transformation. The comparison of nucleation caused by supersaturation and supercooling is of interest for the growing community of researchers working in the field of thin film crystalline silicon devices but is also very impressive and memorable for everybody dealing with nucleation processes in general.

The results presented in this thesis provide a strategy to form optimized poly-Si layers. The best seed layers are obtained by:

- using thin, native oxide interlayers which enhances the preferential $(100)$ orientation.
- starting at low annealing temperature, which increases the grain size and enhances the preferential $(100)$ orientation.
- increasing the annealing temperature after nucleation suppression to decrease the process time without additional nucleation and perpetuation of the preferential $(100)$ orientation.

With this strategy templates made by the aluminum-induced layer exchange process are optimized as seed layers for low-temperature epitaxy. Poly-crystalline silicon thin-film solar cells based on the seed layer concept have the potential to achieve high efficiencies at very low costs which makes them promising candidates for the medium-term future solar cell technology.

# A Preferential orientation calculated as pyramid cluster rotation

The tip of the pyramid is located in the origin of the coordinate system and the edges of the pyramid stay fixed in direction. The edge vectors and the height of the pyramid are defined as

$$\vec{a}: \quad \vec{x} - a \begin{pmatrix} 1 \\ 1 \\ 0 \end{pmatrix} = 0, \tag{A.1}$$

$$\vec{b}: \quad \vec{x} - b \begin{pmatrix} 1 \\ 0 \\ 1 \end{pmatrix} = 0, \tag{A.2}$$

$$\vec{c}: \quad \vec{x} - c \begin{pmatrix} 1 \\ -1 \\ 0 \end{pmatrix} = 0, \tag{A.3}$$

$$\vec{d}: \quad \vec{x} - d \begin{pmatrix} 1 \\ 0 \\ -1 \end{pmatrix} = 0, \tag{A.4}$$

$$\vec{h}: \quad \vec{x} - h \begin{pmatrix} 1 \\ 0 \\ 0 \end{pmatrix} = 0. \tag{A.5}$$

The base of the pyramid is allowed to turn by the two angles $\theta$ and $\phi$ as in spherical coordinates notation. The base is defined along the height in distance $h$. Rotating the base normal by $\theta$ and $\phi$ leads to the base definition in Hessian normal plane form

$$E: \quad \left( \vec{x} - h \begin{pmatrix} 1 \\ 0 \\ 0 \end{pmatrix} \right) \cdot \begin{pmatrix} \cos\theta \\ \sin\theta\cos\phi \\ \sin\theta\sin\phi \end{pmatrix} = 0. \tag{A.6}$$

To find the corners of the pyramid the intersections of the edges with the plane have to be determined. This is done exemplarily for the intersection of the plane $E$ with the vector $\vec{a}$ ($E \bigcap \vec{a}$):

$$\left( a \begin{pmatrix} 1 \\ 1 \\ 0 \end{pmatrix} - h \begin{pmatrix} 1 \\ 0 \\ 0 \end{pmatrix} \right) \cdot \begin{pmatrix} \cos\theta \\ \sin\theta\cos\phi \\ \sin\theta\sin\phi \end{pmatrix} = 0, \tag{A.7}$$

$$\begin{pmatrix} a-h \\ a \\ 0 \end{pmatrix} \cdot \begin{pmatrix} \cos\theta \\ \sin\theta\cos\phi \\ \sin\theta\sin\phi \end{pmatrix} = 0, \tag{A.8}$$

$$(a-h)\cos\theta + a\sin\theta\cos\phi = 0, \tag{A.9}$$

$$a = \frac{h\cos\theta}{\cos\theta + \sin\theta\cos\phi}. \tag{A.10}$$

The other intersection results are calculated correspondingly:

$$b = \frac{h\cos\theta}{\cos\theta + \sin\theta\sin\phi}, \tag{A.11}$$

$$c = \frac{h\cos\theta}{\cos\theta - \sin\theta\cos\phi}, \tag{A.12}$$

$$d = \frac{h\cos\theta}{\cos\theta - \sin\theta\sin\phi}. \tag{A.13}$$

The volume of the pyramid can be determined by using the triple product. The pyramid consists of the four edge vectors. A parallelepiped consist of three vectors. This means that the pyramid is calculated in two parts. One set of vectors consists of the edge vector $\vec{a}$, $\vec{b}$ and $\vec{c}$, the other of $\vec{c}$, $\vec{d}$ and $\vec{a}$. The volume of the half pyramids is a sixth of the parallelepiped mounted by the three edge vectors:

$$V = \frac{1}{6}\vec{a}\cdot\left(\vec{b}\times\vec{c}\right) + \frac{1}{6}\vec{c}\cdot\left(\vec{d}\times\vec{a}\right). \tag{A.14}$$

The four triangular faces of the pyramid have a total area of:

$$S = \frac{1}{2}\left|\vec{a}\times\vec{b}\right| + \frac{1}{2}\left|\vec{b}\times\vec{c}\right| + \frac{1}{2}\left|\vec{c}\times\vec{d}\right| + \frac{1}{2}\left|\vec{d}\times\vec{a}\right|. \tag{A.15}$$

The area of the base of the pyramid is:

$$B = \frac{1}{2}\left|\left(\vec{b}-\vec{a}\right)\times\left(\vec{d}-\vec{a}\right)\right| + \frac{1}{2}\left|\left(\vec{d}-\vec{c}\right)\times\left(\vec{b}-\vec{c}\right)\right|. \tag{A.16}$$

The volume of the pyramid- as for any pointed three dimensional shape- is also the third of the normal height times the base area:

$$V = \frac{h\cos\theta}{3}B. \tag{A.17}$$

This is used to control the obtained results.

For all angles $\theta$ and $\phi$ the following calculations lead to very extensive terms. In order to simplify the calculations the two cases for tilting the pyramid in $[110]$ and $[111]$ direction are regarded only. Turning in $[110]$ direction corresponds to $\phi = 0°$, whereas $\phi = 45°$ corresponds to tilting the pyramid into $[111]$ direction. In order to distinguish the general angle $\theta$ from these two special cases they are renamed to $\alpha_{110}$ and $\alpha_{111}$, respectively. The tilting of the base area is shown in Fig 5.11.

The resulting volume, surface and base for the tilt by $\alpha_{110}$ are:

$$V_{110} = \frac{2}{3}h^3\frac{\cos^2\alpha_{110}}{\cos\left(2\alpha_{110}\right)}, \tag{A.18}$$

$$S_{110} = 2\sqrt{3}h^2\frac{\cos^2\alpha_{110}}{\cos\left(2\alpha_{110}\right)}, \tag{A.19}$$

$$B_{110} = 2h^2\frac{\cos^2\alpha_{110}}{\cos\left(2\alpha_{110}\right)}, \tag{A.20}$$

and by $\alpha_{111}$:

$$V_{111} = \frac{32h^3\cos^4\alpha_{111}}{3\left(1+3\cos\left(2\alpha_{111}\right)\right)^2}, \tag{A.21}$$

$$S_{111} = \frac{32\sqrt{3}h^2\cos^4\alpha_{111}}{\left(1+3\cos\left(2\alpha_{111}\right)\right)^2}, \tag{A.22}$$

$$B_{111} = \frac{32h^2\cos^3\alpha_{111}}{\left(1+3\cos\left(2\alpha_{111}\right)\right)^2}. \tag{A.23}$$

Comparison with equation A.17 confirms the result. The volume $V$ is also related to the surface $S$ in an angular independent way:

$$V = \frac{h}{3\sqrt{3}}S. \tag{A.24}$$

In order to be able to interpret the results in terms of Gibbs energy the volume and the areas have to be transformed into units of atoms. Thus the volume is set to be $i$ atoms, the corresponding height is calculated and substituted into the area terms. The height in units of atoms for tilting in $(110)$ direction is:

$$h_{110} = \frac{\left(\frac{3}{2} i \cos\left(2\alpha_{110}\right)\right)^{\frac{1}{3}}}{\left(\cos\alpha_{110}\right)^{\frac{2}{3}}}, \tag{A.25}$$

and correspondingly for tilting the pyramid into $(111)$ direction:

$$h_{111} = \frac{(3i)^{\frac{1}{3}}\left(1+3\cos\left(2\alpha_{111}\right)\right)^{\frac{2}{3}}}{\left(2\cos\alpha_{111}\right)^{\frac{4}{3}}}. \tag{A.26}$$

The resulting size and angular dependent Gibbs energy for the two tilt angles are:

$$\begin{aligned}\Delta G\left(i,\alpha_{110}\right) = & -\Delta g_V i \\ & + \left(\sigma_{Al,Si} 2^{\frac{1}{3}} 3^{\frac{7}{6}} \frac{\left(\cos\alpha_{110}\right)^{\frac{2}{3}}}{\cos^{\frac{1}{3}}\left(2\alpha_{110}\right)}\right. \\ & \left. + \sigma_{AlO_X,Si} 2^{\frac{1}{3}} 3^{\frac{2}{3}} \frac{1}{\cos\alpha_{110}\cos\left(2\alpha_{110}\right)}\right) i^{\frac{2}{3}},\end{aligned} \tag{A.27}$$

and

$$\begin{aligned}\Delta G\left(i,\alpha_{111}\right) = & -\Delta g_V i \\ & + \left(\sigma_{Al,Si} 2^{\frac{5}{3}} 3^{\frac{7}{6}} \frac{\cos^{\frac{4}{3}}\alpha_{111}}{\left(1+3\cos\left(2\alpha_{111}\right)\right)^{\frac{2}{3}}}\right. \\ & \left. + \sigma_{AlO_X,Si} 2^{\frac{5}{3}} 3^{\frac{2}{3}} \frac{\cos^{\frac{1}{3}}\alpha_{111}}{\left(1+3\cos\left(2\alpha_{111}\right)\right)^{\frac{2}{3}}}\right) i^{\frac{2}{3}}\end{aligned} \tag{A.28}$$

.

# B Abbreviations, symbols and units

| abbreviation | meaning |
|---|---|
| ALILE | aluminum-induced layer exchange process |
| APCVD | atmospheric pressure chemical vapor deposition |
| a-Si:H | hydrogenated amorphous silicon |
| CIS | Copper-Indium (Gallium)-Selenide (Sulfite) |
| CSG | Crystalline Silicon on Glass |
| EELS | electron energy loss spectrospocy |
| EBSD | electron back scatter diffraction |
| ECRCVD | electron cyclotron resonance chemical vapor deposition |
| FESMC | field enhanced silicide mediated crystallization |
| FIB | focussed ion beam |
| FOx | flowable oxide |
| HMI | Hahn-Meitner-Institut Berlin |
| HR-TEM | high resolution transmission electron microscope |
| IAD | ion assisted deposition |
| IMEC | interuniversity microelectronics center |
| KUL | Catholic University Leuven |
| METEOR | European-project 'Metal-induced Crystallisation and Epitaxial Deposition for Thin, Efficient and Low-cost Crystalline Si Solar Cells' |
| MIC | metal-induced crystallization |
| MILC | metal-induced lateral crystallization |
| PECVD | plasma enhanced chemical vapor deposition |
| PV | photovoltaic |
| ROI | region of interest |
| RTA | rapid thermal annealing |
| SAD | selective area diffraction |

| abbreviation | meaning |
|---|---|
| SPE | solid phase epitaxy |
| SPC | solid phase crystallization |
| TEM | transmission electron microscope |
| TUW | Technical University Wien |
| TCO | transparent conductive oxide |
| TFT | thin-film transistor |
| UNSW | University of New South Wales |
| $\mu$c-Si:H | hydorgenated microcrystalline silicon |
| $W_p$ | Watt peak |

| symbol | unit | meaning |
|---|---|---|
| $A$ | | nucleation and growth dependent constant in KJMA equation |
| $\alpha_{110}$ | $^\circ$ | tilt angle from $(100)$ to $(110)$ direction |
| $\alpha_{111}$ | $^\circ$ | tilt angle from $(100)$ to $(111)$ direction |
| $C$ | $\mathrm{cm}^{-3}$ | concentration |
| $C^*$ | $\mathrm{cm}^{-3}$ | critical concentration |
| $C^{**}$ | $\mathrm{cm}^{-3}$ | concentration of critical clusters |
| $C_{a-Si}$ | $\mathrm{cm}^{-3}$ | Si concentration in Al in equilibrium with amorphous Si |
| $C_{max}$ | $\mathrm{cm}^{-3}$ | maximum Si concentration in Al |
| $C_S$ | $\mathrm{cm}^{-3}$ | saturation concentration, solubility limit |
| $C_{Si}$ | $\mathrm{cm}^{-3}$ | Si concentration (in Al) |
| $D$ | $\mathrm{cm}^2\,\mathrm{s}^{-1}$ | diffusion coefficient |
| $d$ | $\mu\mathrm{m}$ | depletion region width |
| $d_{Ox}$ | $\mathrm{nm}$ | thickness of the Al oxide interlayer |
| $f$ | $\mathrm{s}^{-1}$ | stabilization rate of a critical cluster |
| $G$ | $\mathrm{eV}$ | Gibbs energy |
| $\Delta G$ | $\mathrm{eV}$ | driving force |

| symbol | unit | meaning |
|---|---|---|
| $\Delta G^a$ | $\mathrm{eV}$ | activation energy |
| $\Delta G_m$ | $\mathrm{eV}$ | activation energy for atomic migration |
| $\Delta G_V$ | $\mathrm{eV}$ | Gibbs energy reduction by phase transition of a unit volume |
| $\Delta g_V$ | $\mathrm{eV/atom}$ | Gibbs energy reduction by phase transition of one atom |
| $\Delta G^*$ | $\mathrm{eV}$ | Gibbs energy needed to form a critical cluster |
| $i$ | atom | number of atoms |
| $j$ | $\mathrm{s}^{-1}$ | rate |
| $J_1$ | $\mathrm{atom\,s}^{-1}$ | Si flux from a-Si to c-Si across the interlayer |
| $J_2$ | $\mathrm{atom\,s}^{-1}$ | Si flux within the Al layer |
| $j_G$ | $\mathrm{s}^{-1}$ | growth rate |
| $j_N$ | $\mathrm{s}^{-1}$ | nucleation rate |
| $k$ | $\mathrm{eV/K}$ | Boltzmann constant ($8.6215 \cdot 10^{-5}\,\mathrm{eV/K}$) |
| $L$ | $\mu\mathrm{m}$ | depletion region width |
| $m$ | | constant in KJMA equation determined by experimental conditions and dimensions |
| $N_G$ | $10^3\,\mathrm{mm}^{-2}$ | nucleation density |
| $N$ | $\mathrm{atoms}$ | number of particles |
| $p$ | $\mathrm{Pa}$ | pressure |
| $R$ | | ratio |
| $R_C$ | $\%$ | crystallized fraction |
| $r$ | $\mu\mathrm{m}$ | radius |
| $r^*$ | $\mathrm{nm}$ | critical radius |
| $S$ | | supersaturation |
| $\sigma$ | $\mathrm{eV/atom}$ | specific surface energy |
| $\sigma_{Al,Si}$ | $\mathrm{eV/atom}$ | specific surface energy at the Al-Si interface |
| $\sigma_{AlO_X,Si}$ | $\mathrm{eV/atom}$ | specific surface energy at the $AlO_X$-Si interface |
| $T$ | °C | temperature |

| symbol | unit | meaning |
|---|---|---|
| $T_1$ | °C | temperature before cooling step |
| $T_2$ | °C | temperature during cooling step |
| $T_3$ | °C | temperature after cooliung step |
| $T_A$ | °C | annealing temperature |
| $t$ | $\mathrm{min}$ | time |
| $t_1$ | $\mathrm{min}$ | time until cooling step |
| $t_2$ | $\mathrm{min}$ | time at the end of the cooling step |
| $t_N$ | $\mathrm{min}$ | nucleation time |
| $t_P$ | $\mathrm{min}$ | process time |
| $T_S$ | $\mathrm{K}$ | heating step temperature change |
| $t_S$ | $\mathrm{min}$ | heating step time |
| $V$ | $\mathrm{nm}^3$ | volume |
| $v_2$ | $\mathrm{K min}^{-1}$ | cooling rate |
| $v_G$ | $\mu\mathrm{m}/\,\mathrm{min}$ | grain growth velocity |
| $v_{G,0}$ | $\mu\mathrm{m}/\,\mathrm{min}$ | final constant, grain growth velocity |
| $\mu$ | $\mathrm{eV/atom}$ | chemical potential |
| $\Delta\mu$ | $\mathrm{eV/atom}$ | chemical potential difference |
| $\mu_{a-Si}$ | $\mathrm{eV/atom}$ | chemical potential of amorphous Si |
| $\mu_{c-Si}$ | $\mathrm{eV/atom}$ | chemical potential of crystalline Si |
| $\mu_j$ | $\mathrm{eV/atom}$ | chemical potential of particle $j$ |
| $\mu_{Si}$ | $\mathrm{eV/atom}$ | chemical potential of silicon |
| $\mu_{Si,0}$ | $\mathrm{eV/atom}$ | chemical potential of silicon at the saturation concentration |
| $X$ | $\mathrm{eV}/\,\mathrm{atom}$ | angular dependant coefficient in preferential orientation model |
| $x$ | $\mathrm{m}$ | distance variable |
| $\omega$ | $\mathrm{s}^{-1}$ | coefficient of the stabilization rate of a critical cluster $f$ |

# Bibliography


[1] M. Rogol, S. Doi, and A. Wilkinson. Sun screen - investment opportunities in solar power, 2004.

[2] M. Schmela and Siemer. J. Wachstum um die wette. *Photon*, 0405:28, 2005.

[3] W. Shockley and H.J. Queisser. Detailed balance limit of efficiency of p-n junction solar cells. *J. Appl. Phys.*, 32(3):510–519, 1961.

[4] M. A. Green. Third generation photovoltaics: solar cells for 2020 and beyond. *Physica E*, 14:65–70, 2002.

[5] M. A. Green. Photovoltaics: technology overview. *Energy Policy*, 28:989–998, 2000.

[6] D.L. Staebler and C.R. Wronski. Reversible conductivity changes in discharge-produced amorphous si. *Appl. Phys. Lett.*, 31(4):292–294, 1977.

[7] K. Yamamoto, A. Nakajima, M. Yoshimi, T. Sawada, S. Fukuda, T. Suezaki, M. Ichikawa, Y. Koi, M. Goto, T. Meguro, T. Matsuda, M. Kondo, T. Sasaki, and Y. Tawada. A high efficiency thin film silicon solar cell and module. *Solar Energy*, 77:939–949, 2004.

[8] T. Matsuyama, N. Terada, T. Baba, T. Sawada, S. Tsuge, K. Wakisaka, and S. Tsuda. High-quality polycrystalline silicon thin film prepared by a solid phase crystallization method. *J. Non-Cryst. Solids*, 198-200(2):940–944, 1996.

[9] O. Nast, T. Puzzer, L. M. Koschier, A. B. Sproul, and S. R. Wenham. Aluminum-induced crystallization of amorphous silicon on glass substrates above and below the eutectic temperature. *Appl. Phys. Lett.*, 73(22):3214–3216, 1998.

[10] M. Volmer. *Kinetik der Phasenbildung*, volume 4 of *Die Chemische Reaktion*. Verlag von Theodor Steinkopff, Leipzig, 1939.

[11] D.A. Porter and K.E. Easterling. *Phase Transformations in Metals and Alloys*. Chapman & Hall, London, UK, 2nd edition, 1992.

[12] C. Spinella, S. Lombardo, and F. Priolo. Crystal grain nucleation in amorphous silicon. *J. Appl. Phys.*, 84(10):5383–5414, 1998.

[13] A.E. Kolmogorov. On statistic theory of crystallization of metals. *Izv. Akad. Nauk SSR Ser. Fiz. Mat. Nauk*, 1:355, 1937. original title translated from russian.

[14] W.A. Johnson and R.F. Mehl. Reaction kinetics in processes of nucleation and growth. *Trans. Am. Inst. Min. Metall. Pet. Eng.*, 135:416–442, 1939.

[15] M. Avrami. Kinetics of phase change. i. *J. Chem. Phys.*, 7:1103–1112, 1939.

[16] M. Avrami. Kinetics of phase change. ii. *J. Chem. Phys.*, 8:212–224, 1940.

[17] M. Avrami. Granulation, phase change, and microstructure. *J. Chem. Phys.*, 9:177–184, 1941.

[18] M. Castro, F. Dominguer-Adame, A. Sanchez, and T. Rodriguez. Model for crystallization kinetics: Deviations from kolmogorov-johnson-mehl-avrami kinetics. *Appl. Phys. Lett.*, 75(15):2205–2207, 1999.

[19] C. Sagui and M. Grant. Theory of nucleation and growth during phase separation. *Phys. Rev. E.*, 59(4):4175–4187, 1999.

[20] R.W. Bower, R. Baron, J.W. Mayer, and O.J. Marsh. Deep (1-10 $\mu$) penetration of ion-implanted donors in silicon. *Appl. Phys. Lett.*, 9(5):203–205, 1966.

[21] L. Csepregi, E.F. Kennedy, and J.W. Mayer. Substrate-orientation dependence of the epitacial regrowth rate from si-implanted amorphous si. *J. Appl. Phys.*, 49(7):3906–3911, 1978.

[22] L. Csepregi, E.F. Kennedy, T.J. Gallagher, and J.W. Mayer. Reordering of amorphous layers of si implated with 31p, 75as, and 11b ions. *J. Appl. Phys.*, 48(10):4234–4240, 1977.

[23] E.F. Kennedy, L. Csepregi, and J.W. Mayer. Influence of 16o, 12o, 14n, and noble gases on the crystallization of amorphous si layers. *J. Appl. Phys.*, 48(10):4241–4246, 1977.

[24] C.S. Pai and S.S. Lau. Comparison of electronic effects and stress effects in enhancing regrowth rate of ion-implanted amorphous si. *Appl. Phys. Lett.*, 47(11):1214–1216, 1985.

[25] U. Köster. Crystallization and decompostion of amorphous semiconductors. *Adv. Colloid Interface Sci.*, 10:129–172, 1979.

[26] R.B. Iverson and R. Reif. Recrystallization of amorphized polycrystalline silicon films of $sio_2$: Temperature dependence of crystallization parameters. *J. Appl. Phys.*, 62(5):1675–1681, 1987.

[27] E.P. Donovan, F. Spaepen, D. Turnbull, J.M. Poate, and D.C. Jacobson. Calorimetric studies of crystallization relaxation of amorphous si and ge prepared by ion implantation. *J. Appl. Phys.*, 57(6):1795–1784, 1985.

[28] M. A. Green, P. A. Basore, N. Chang, D. Clugston, R. Egan, R. Evans, D. Hogg, S. Jarnason, M. Keevers, P. Lasswell, J. O'Sullivan, U. Schubert, A. Turner, S. R. Wenham, and T. Young. Crystalline silicon on glass (csg) thin-film solar cell modules. *Solar Energy*, 77:857–863, 2004.

[29] J.O. McCaldin and H. Sankur. Diffusivity and solubility of si in the al metallization of intergrated circuits. *Appl. Phys. Lett.*, 19(12):524–527, 1971.

[30] A. Hiraki. A model on the mechanism of room temperature interface intermixing reaction in various metal-semiconductor coupels: What triggers the reaction? *J. Electrochem. Soc.*, 127:2662, 1980.

[31] A. Hiraki. Recent developments on metal-silicon interfaces. *Appl. Surf. Sci.*, 56-58:370–381, 1992.

[32] K.N. Tu. Selective growth of metal-rich silicide of near-noble metals. *Appl. Phys. Lett.*, 27(4):221–224, 1975.

[33] S. R. Herd, P. Chaudhari, and M. H. Brodsky. Metal contact induced crystallization in films of amorphous silicon and germanium. *J. Non-Cryst. Solids*, 7:309–327, 1972.

[34] K.H. Kim, J.H. Oh, E.H. Kim, and J. Jang. Formation and analysis of disk-shaped grains by ni-mediated crystallization of amorphous silicon. *J. Vac. Sci. Technol. A*, 22(6):2469–2472, 2004.

[35] P. Joubert, L. Henry, and D. Riviere. Solid phase growth of disk-shaped ptsi clusters on lightly nitridized si substrates. *J. Appl. Phys.*, 56(10):2734–2739, 1984.

[36] Jong-Hyun Choi, Seung-Soo Kim, Jun-Hyuk Cheon, Seong-Jin Park, Yong-Duck Son, and Jin Jang. Kinetics of ni-mediated crystallization of a-si through a $\mathrm{sin}_x$ cap layer. *J. Electrochem. Soc.*, 151(7):G448–G451, 2004.

[37] W.S. Sohn, J.H. Choi, K.H. Kim, J.H. Oh, and S.S Kim. Crystalline orientation of polycrystalline silicon with disklike grains produced by silicide-mediated crystallization of amorphous silicon. *J. Appl. Phys.*, 94(7):4326–4331, 2003.

[38] J. Jang, J.Y. Oh, S.K. Kim, Y.J. Choi, S.Y. Yoon, and C.O. Kim. Electric-field-enhanced crystallization of amorphous silicon. *nature*, 395:481–483, 1998.

[39] C. Hayzelden, J. L. Batstone, and R. C. Cammarata. In situ transmission electron microscopy studies of silicide-mediated crystallization of amorphous silicon. *Appl. Phys. Lett.*, 60(2):225–227, 1992.

[40] G. Ottaviani, D. Sigurd, V. Marrello, J.W. Mayer, and J.O. McCaldin. Crystallization of ge and si in metal films. *J. Appl. Phys.*, 45(4):1730–1739, 1974.

[41] T.J. Konno and R. Sinclair. Crystallization of silicon in aluminum/amorphous-silicon multilayers. *Philosophical Magazine B*, 66(6):749–765, 1992.

[42] T.J. Konno and R. Sinclair. Metal-contact-induced crystallization of semiconductors. *Mat. Sci. Eng. A*, 179-180(1):426–432, 1994.

[43] S.M. Sze. *Physics of Semiconductor Devices*. Wiley, Singapore, 2nd edition, 1981.

[44] R.L. Boatright and J.O. McCaldin. Solid-state growth of si to produce planar surfaces. *J. Appl. Phys.*, 47(6):2260–2262, 1976.

[45] J.S. Best and J.O. McCaldin. Interfacial impurities and the reaction between si and evaporated al. *J. Appl. Phys.*, 46(9):4071–4072, 1975.

[46] G. Majni and G. Ottaviani. Large-area unifomr growth of <100> si through al film by solid phase epitaxy. *Appl. Phys. Lett.*, 31(2):125–126, 1977.

[47] G. Majni and G. Ottaviani. Substrate effects in si-al solid phase epitaxial growth. *Thin Solid Films*, 55:235–242, 1978.

[48] G. Majni and G. Ottaviani. Growth kinetics of <111> si through an al layer by solid phase epitaxy. *J. Cryst. Growth*, 46:119–124, 1979.

[49] G. Majni and G. Ottaviani. Solid phase epitaxial growth of si through al film. *J. Cryst. Growth*, 45:132–137, 1978.

[50] B-Y. Tsaur, G.W. Turner, and J.C.C Fan. Efficient si solar cell by low-temperature solid-phase epitaxy. *Appl. Phys. Lett.*, 39(9):749–751, 1981.

[51] L. M. Koschier, S. R. Wenham, M. Gross, T. Puzzer, and A. B. Sproul. Low temperature junction and back surface field formation for photovoltaic devices. In *Proc. of the 2nd World Conference and Exhibition on Photovoltaic Energy Conversion*, pages 1539–1542, Vienna, Austria, 1998.

[52] O. Nast and S. R. Wenham. Elucidation of the layer exchange mechanism in the formation of polycrystalline silicon by aluminum-induced crystallization. *J. Appl. Phys.*, 88(1):124–132, 2000.

[53] O. Nast. *The aluminium-induced layer exchange forming polycrystalline silicon on glass for thin-film solar cells*. PhD thesis, Philipps-Universität Marburg, 2000.

[54] O. Nast and A. J. Hartmann. Influence of interface and al structure on layer exchange during aluminum-induced crystallization of amorphous silicon. *J. Appl. Phys.*, 88(2):716–724, 2000.

[55] P. Widenborg and A. G. Aberle. Surface morphology of poly-si films made by aluminium-induced crystallisation on glass substrates. *J. Cryst. Growth*, 242:270–282, 2002.

[56] J. Schneider. *Oberflächenpräparation von ALILE-Saatschichten für polykristalline Silizium-Dünnschichtsolarzellen*. Diplomarbeit, Technische Universität Berlin, 2002.

[57] W. Fuhs, S. Gall, B. Rau, M. Schmidt, and J. Schneider. A novel route to a polycrystalline silicon thin-film solar cell. *Solar Energy*, 77:961–968, 2004. in press.

[58] N.-P. Harder, T. Puzzer, P. Widenborg, S. Oelting, and A. G. Aberle. Ion-assisted low-temperature silicon epitaxy on randomly textured seed layers on glass. *Cryst. Growth Des.*, 3(5):767–771, 2003.

[59] A.G. Aberle, P.I. Widenborg, D. Song, A. Straub, M.L. Terry, T. Walhs, A. Sproul, P. Campbell, D. Inns, and B. Beilby. Recent advances in polycrystalline silicon thin-film solar cells on glass at unsw. In *Proc. of the 31st IEEE PV Conference*, Orlando, USE, 2005. in press.

[60] S. Gall, J. Schneider, J. Klein, M. Muske, B. Rau, E. Conrad, I. Sieber, W. Fuhs, C. Ornaghi, D. Van Gestel, I. Gordon, K. Van Nieuwenhuysen, G. Beaucarne, J. Poortmans, M. Stöger-Pollach, J. Bernardi, P. Schattschneider, Y. Wang, and O. Van der Biest. Crystalline silicon thin-film solar cells on foreign substrates: The european project meteor. In *Proc. of the 19th European Photovoltaic Solar Energy Conference*, pages 475–478, Paris, France, 2004.

[61] I. Gordon, D. Van Gestel, K. Van Nieuwenhuysen, L. Carnel, G. Beaucarne, and J. Poortmans. Thin-film polycrystalline silicon solar cells on ceramic substrates by aluminium-induced crystallization. *Thin Solid Films*, 2005. in press.

[62] L. Carnel, I. Gordon, K. Van Nieuwenhuysen, D. Van Gestel, G. Beaucarne, and J. Poortmans. Defect passivation in chemical vapour deposited fine grained polycrystalline silicon by plasma hydrogenation. *Thin Solid Films*, 2005. in press.

[63] J. Klein, J. Schneider, M. Muske, R. Heimburger, S. Gall, and W. Fuhs. Aluminium-induced crystallisation of amorphous silicon: parameter variation for optimisation of the process. In *Proc. of the 31st Photovoltaic Specialits Conference*, Orlando, USA, 2005. in press.

[64] B. Rau, I. Sieber, J. Schneider, M. Muske, M. Stöger-Pollach, P. Schattschneider, S. Gall, and W. Fuhs. Low-temperature si epitaxy on large-grained

polycrystalline seed layers by electron-cyclotron resonance chemical vapor deposition. *J. Cryst. Growth*, 270(3-4):396–401, 2004.

[65] K. Petter, I. Sieber, B. Rau, S. Brehme, K. Lips, and W. Fuhs. Structural defect and photoluminescence of epitaxial si films grown at low temperatures. *Thin Solid Films*, 2005. in press.

[66] M. Stöger-Pollach. *Advanced methods in electron enery loss spectrometry and energy filtered transmission electron microscopy: Application to the Aluminum Induced Layer Exchange in Si thin film solar cells*. PhD thesis, Technische Universität Wien, 2004.

[67] H. Kim, D. Kim, G. Lee, D. Kim, and S. H. Lee. Polycrystalline si films formed by al-induced crystallization (aic) with and without al oxides at al/a-si interface. *Sol. Energy Mater. Sol. Cells*, 74:323–329, 2002.

[68] T. Ito, H. Fukushima, and M. Yamaguchi. Fabrication of thin-film polycrystalline silicon solar cells by silane-gas-free process using aluminium-induced crystallization. *Jpn. J. Appl. Phys.*, 42(Part 1, No. 4A):1526–1532, 2003.

[69] T. Ito, H. Fukushima, and M. Yamaguchi. Efficiency potential of thin film polycrystalline silicon solar cells by silane-gas-free process using aluminium indced crystallization. *Sol. Energy Mater. Sol. Cells*, 83:91–99, 2004.

[70] E. Pihan, A. Slaoui, P. Roca i Carbarrocas, and A. Focsa. Polycrystalline silicon films by aluminium-induced crystallisation: growth proces vs. silicon deposition method. *Thin Solid Films*, 451-452:328–333, 2004.

[71] A. Slaoui, A. Focsa, E. Pihan, G. Beaucarne, and J. Poortmans. Formation of thin film polycrystalline silicon on ceramic substrates for photovoltaics. In *Proc. of the 31st Photovoltaic Specialists Conference*, Orlando, USA, 2005. in press.

[72] G. Ekanayake, S. Summers, and H. S. Reehal. Influence of argon on crystalline silicon film growth by ecr plasma cvd for solar cells. In Kosuke Kurokawa, editor, *Proc. of the 3rd WCPEC*, volume B, pages 1867–1870, Osaka, Japan, 2003. WCPEC-3 Organising Commitee. latest news paper 5LN-C-02.

[73] G. Ekanayake, Z. Lu, and H. S. Reehal. Polycrystalline si film formation by aluminium-induced crystallisation. In *Proc. of the EPVSEC 19th*, Paris, 2004. JS.

[74] D. Dimova-Malinovska, O. Angelov, M. Sendova-Vassileva, M. Kamenova, and J.-C. Pivin. Polycrystalline silicon thin films on glass substrate. *Thin Solid Films*, 451-452:303–307, 2004.

[75] D. Dimova-Malinovska, O. Angelov, M. Sendova-Vassileva, V. Grigorov, and M. Kamenova. Structural properties of poly-si films obtained by aluminium induced crystallisation in different atmospheres. In *Proc. of the 19th European Photovoltaic Solar Energy Conference*, pages 371–373, Paris, France, 2004.

[76] M. Gjukic, M. Buschbeck, R. Lechner, and M. Stutzmann. Aluminum-induced crystallization of amorphous silicon-germanium thin films. *Appl. Phys. Lett.*, 85(11):2134–2136, 2004.

[77] M. Gjukic, R. Lechner, M. Buschbeck, and M. Stutzmann. Optical and electrical properties of polycrystalline silicon-germanium thin films prepared by aluminum-induced layer exchange. *Appl. Phys. Lett.*, 86(062115):3 pages, 2005.

[78] D.L. Young, P. Stradins, E. Iwaniczko, B. To, R. Reedy, Y. Yan, H. M. Branz, J. Lohr, M. Alvarez, J. Booske, A. Marconnet, and Q. Wang. Solid phase crystallization of hot-wire cvd amorphous silicon films. In *Proc. of the MRS Spring meeting*, San Francisco, USA, 2005. in press.

[79] P. Stradins, D.L. Young, H. M. Branz, M. Page, and Q. Wang. Real time monitoring of the crystallization of hydrogenated amorphous silicon. In *Proc. of the MRS Spring Meeting*, San Francisco, USA, 2005. in press.

[80] C.E. Richardson, B.M. Kayes, M.J. Dicken, and H. A. Atwater. A phase diagram of low temperature epitaxial silicon grown by hot-wire chemical vapor deposition for photovoltaic devices. In *Proc. of the MRS Spring Meeting*, San Francisco, USA, 2005. in press.

[81] O. Nast, T. Puzzer, C. T. Chou, and M. Birkholz. Grain size and structure analysis of polycrystalline silicon on glass formed by aluminum-induced crystallization for thin-film solar cells. In *Proc. of the 16th European Photovoltaic Solar Energy Conference*, pages 292–297, Glasgow, UK, 2000.

[82] O. Nast, S. Brehme, S. Pritchard, A. G. Aberle, and S. R. Wenham. Aluminium-induced crystallisation of silicon on glass for thin-film solar cells. *Sol. Energy Mater. Sol. Cells*, 65:385–392, 2001.

[83] J. Schwarzkopf, B. Selle, W. Bohne, J. Röhrich, I. Sieber, and W. Fuhs. Disorder in silicon films grown epitaxially at low temperature. *J. Appl. Phys.*, 93(9):5215, 2003.

[84] P. Reinig, F. Fenske, W. Fuhs, and B. Selle. Crystalline silicon films grown by pulsed dc magnetron sputtering. *J. Non-Cryst. Solids*, 299-302:128–132, 2002.

[85] A. Straub, P. Widenborg, A. B. Sproul, Y. Huang, N.-P. Harder, and A. G. Aberle. Fast and non-destructive assessement of epitaxial quality of polycrystalline silicon films on glass by optical measurements. *J. Cryst. Growth*, 265:168–173, 2004.

[86] S.I. Raider, R. Flitsch, and M.J. Palmer. Oxide growth on etched silicon in air at room temperature. *J. Electrochem. Soc.*, 122(3):413–418, 1975.

[87] H.R. Philipp and E.A. Taft. An optical characterization of native oxides and thin thermal oxides on silicon. *J. Appl. Phys.*, 53(7):5224–5229, 1982.

[88] D.J. Prior, A.P. Boyle, F. Brenker, M.C. Cheadle, A. Day, G. Lopez, L. Peruzo, G.J. Potts, S. Reddy, R. Spiess, N.E. Timms, P. Trimby, J. Wheeler, and L. Zetterström. The application of electron backscatter diffraction and orientation contrast imaging in the sem to textural problems in rocks. *American Mineralogist*, 84:1741–1759, 1999.

[89] S. Gall, J. Schneider, M. Muske, I. Sieber, O. Nast, and W. Fuhs. Poly-si seeding layers by aluminium-induced crystallisation. In *Proc. of the PV in Europe*, pages 87–90, Rome, Italy, 2002.

[90] R. B. Bergmann, C. Zaczek, N. Jensen, S. Oelting, and J. H. Werner. Low-temperature si epitaxy with high deposition rate using ion-assisted deposition. *Appl. Phys. Lett.*, 72(23):2996–2998, 1998.

[91] J. Platen, B. Selle, S. Brehme, U. Zeimer, and W. Fuhs. Low-temperature epitaxial growth of si by electron cyclotron resonance chemical vapor deposition. *Thin Solid Films*, 381:22–30, 2001.

[92] J.M.E. Harper, S.E. Hörnström, O. Thomas, A. Charai, and L. Krusin-Elbaum. Mechanism for success or failure of diffusion barriers between aluminum and silicon. *J. Vac. Sci. Technol. A*, 7(3):875–881, 1989.

[93] J.S. Reid, E. Kolawa, C.M. Garland, M.-A. Nicolet, F. Cardone, D. Gupta, and R.P. Ruiz. Amorphous (mo, ta, or w)-si-n diffusion barriers for al metallizations. *J. Appl. Phys.*, 79(2):1109–1115, 1996.

[94] S. Gall, M. Muske, I. Sieber, O. Nast, and W. Fuhs. Aluminum-induced crystallization of amorphous silicon. *J. Non-Cryst. Solids*, 299-302:741, 2002.

[95] A. Aberle, P. Widenborg, A. Straub, D.-H. Neuhaus, O. Hartley, and N.-P. Harder. Fabrication method for crystalline semiconductor films on foreign substrates. patent application published in WO 2004/033769 A1.

[96] Al-si (aluminium - silicon). In B. Predel, editor, *Group IV Physical Chemistry*, volume 5. Landoldt-Börnstein, 1991.

[97] C. Zener. Theory of growth of spherical precipitates from solid solution. *J. Appl. Phys.*, 40:950–953, 1949.

[98] G. J. van Gurp. Diffusion-limited si precipitation in evaporated al/si films. *J. Appl. Phys.*, 44(5):2040–2050, 1973.

[99] D.J. Eaglesham, A.E. White, L.C. Feldman, N. Mriya, and D.C. Jacobson. Equlibrium shape of si. *Phys. Rev. Lett.*, 70(11):1643–1646, 1993.

[100] L.P.H. Jeurgens, W.G. Sloof, F.D. Tichelar, and E.J. Mittemeijer. Structure and morphology of aluminium-oxide films formed by thermal oxidation of aluminium. *Thin solid films*, 418:89–101, 2002.

**list of publications**

**journal papers**

J. Schneider, J. Klein, M. Muske, S. Gall, and W. Fuhs, *'Depletion regions in the aluminum-induced layer exchange process crystallizing amorphous Si'*, Applied Physics Letters, accepted.

J. Schneider, R. Heimburger, J. Klein, M. Muske, S. Gall, and W. Fuhs, *'Aluminum-induced crystallization of amorphous silicon: influence of temperature profiles'*, Thin Solid Films, article in press.

J. Schneider, J. Klein, M. Muske, S. Gall, and W. Fuhs, *'Aluminum-induced crystallization of amorphous silicon: Preparation effect on growth kinetics'*, J. Non-Cryst. Solids 338-340, (2004), 127.

B. Rau, I. Sieber, J. Schneider, M. Muske, M. Stöger-Pollach, P. Schattschneider, S. Gall, and W. Fuhs, *'Low-temperature Si epitaxy on large-grained polycrystalline seed layers by electron-cyclotron resonance chemical vapor deposition'*, J. Cryst. Growth 270, (2004), 396.

J. Klein, J. Schneider, M. Muske, S. Gall, and W. Fuhs, *'Aluminium-induced crystallisation of amorphous silicon: influence of the aluminium layer on the process'*, Thin Solid Films 451-452, (2004), 481.

W. Fuhs, S. Gall, B. Rau, M. Schmidt, and J. Schneider, *'A novel route to a polycrystalline silicon thin-film solar cell'*, Solar Energy 77, (2004), 961.

F. Brunner, A. Braun, P. Kurpas, J. Schneider, J. Würfl, and M. Weyers, *'Investigation of short-term current gain stability of GaInP/GaAs-HBTs grown by MOVPE'*, Microelectronics Reliability 43, (2003), 839.

**conference contributions**

J. Schneider, A. Schneider, A. Sarikov, J. Klein, M. Muske, S. Gall, W. Fuhs, *'Aluminium-induced crystallisation: nucleation and growth process'*, ICANS 21, Lisbon, Portugal, (2005), to be published in Journal of Non-Crystalline Solids.

J. Schneider, I. Sieber, A. Sarikov, J. Klein, M. Muske, S. Gall, W. Fuhs, *'Crystal orientation of silicon thin films made by aluminum-induced layer exchange'*, ACCGE 16th, Big Sky, Montana, USA, (2005), Abstract #145, to be published in Journal of Crystal Growth.

Andrey Sarikov, Jens Schneider, Juliane Klein, Martin Muske, Stefan Gall, *'Theoretical study of initial stages of the aluminium-induced layer-exchange process'*, ACCGE 16th, Big Sky, Montana, USA, (2005), Abstract #201, to be published in Journal of Crystal Growth.

S. Gall, J. Schneider, J. Klein, M. Muske, B. Rau, E. Conrad, I. Sieber, W. Fuhs, D. Van Gestel, I. Gordon, K. Van Nieuwenhuysen, L. Carnel, J. Irigoyen, G. Beaucarne, J. Poortmans, M. Stöger-Pollach, P. Schattschneider, Y. Wang, O. Van Der Biest, *'Development of polycrystalline silicon thin-film solar cells within the european project METEOR'*, 20th European Photovoltaic Solar Energy Conference, Barcelona, Spain, (2005), 2CV.3.18.

B. Rau, J. Klein, J. Schneider, E. Conrad, I. Sieber, S. Gall, W. Fuhs, M. Stöger-Pollach, P. Schattschneider, *'Polycrystalline Si Thin-Film Solar Cells on Glass by Epitaxial Thickening of Seed Layers Using ECRCVD'*, 20th European Photovoltaic Solar Energy Conference, Barcelona, Spain, (2005), 2CV.4.36.

S. Gall, J. Schneider, J. Klein, K. Hübener, M. Muske, B. Rau, E. Conrad, I. Sieber, K. Petter, K. Lips, M. Stöger-Pollach, P. Schattschneider, W. Fuhs, *'Large-grained polycrystalline silicon on glass for thin-film solar cells'*, EMRS, Strassbourg, France, (2005), F-II.01, invited talk, to be published in Thin Solid Films. conference contributions.

J. Schneider, J. Klein, A. Sarikov, M. Muske, S. Gall, and W. Fuhs, *'Suppression of nucleation during the aluminum-induced layer exchange process'*, Proc. of the 2005 MRS Spring Meeting, San Francisco, USA, (2005), in press.

S. Gall, J. Schneider, J. Klein, M. Muske, B. Rau, E. Conrad, I. Sieber, W. Fuhs, D. Van Gestel, I. Gordon, G. Beaucarne, J. Poortmans, M. Stöger-Pollach, P. Schattschneider, *'Large-grained polycrystalline silicon thin-film solar cells using AIC seed layers'*, Proc. of the 31st IEEE Photovoltaic Specialists Conference, Orlando, USA, (2005), in press.

J. Klein, J. Schneider, M. Muske, R. Heimburger, S. Gall, W. Fuhs, *'Aluminium-induced crystallisation of amorphous silicon: parameter variation for optimisation of the process'*, Proc. of the 31st IEEE Photovoltaic Specialists Conference, Orlando, USA, (2005), in press.

J. Schneider, J. Klein, M. Muske, K. Hübener, S. Gall, and W. Fuhs, *'Aluminium-*

*induced crystallisation of amorphous silicon: interface influence on grain growth'*, Proc. of the 19th European Photovoltaic Solar Energy Conference, Paris, France, (2004), 1145.

B. Rau, J. Schneider, M. Muske, I. Sieber, S. Gall, M. Stöger-Pollach, P. Schattschneider, and W. Fuhs, *'Epitaxial Si growth on polycrystalline Si seed layers at low temperature'*, Proc. of the 19th European Photovoltaic Solar Energy Conference, Paris, France, (2004), 1131.

J. Klein, J. Schneider, M. Muske, S. Gall, and W. Fuhs, *'Aluminium-Induced Crystallisation of amorphous Silicon: The influence of the aluminium layer on the process'*, Proc. of the 19th European Photovoltaic Solar Energy Conference, Paris, France, (2004), 1135.

S. Gall, J. Schneider, J. Klein, M. Muske, B. Rau, E. Conrad, I. Sieber, W. Fuhs, C. Ornaghi, D. Van Gestel, I. Gordon, K. Van Nieuwenhuysen, G. Beaucarne, J. Poortmans, M. Stöger-Pollach, J. Bernardi, P. Schattschneider, Y. Wang, and O. Van der Biest, *'Crystalline Silicon thin-film solar cells on foreign substrates: The european project METEOR'*, Proc. of the 19th European Photovoltaic Solar Energy Conference, Paris, France, (2004), 475.

J. Schneider, J. Klein, M. Muske, A. Schöpke, S. Gall, and W. Fuhs, *'Aluminium-induced crystallisation of amorphous silicon: Influence of oxidation conditions'*, Proc. of the 3rd World Conference on Photovoltaic Energy Conversion, Osaka, Japan, (2003), 106.

S. Gall, J. Schneider, M. Muske, I. Sieber, O. Nast, and W. Fuhs, *'Poly-Si seeding layers by aluminium-induced crystallisation'*, Proc. of the PV in Europe, Rome, Italy,

(2002), 87.

S. Gall, M. Muske, I. Sieber, J. Schneider, O. Nast, and W. Fuhs, *'Polycrystalline silicon on glass by aluminium-induced crystallization'*, Proc. of the 29th IEEE Photovoltaic Specialists Conference, New Orleans, USA, (2002), 1202.

# Acknowledgement

I want to thank Prof. Dr. Christian Boit for accepting my proposal as Ph.D. student on an almost blind date; furthermore for being friendly, critical, supportive, constructive and at al times interested in the progress of my work.

I want to thank Prof. Dr. Walther Fuhs for all the scientific, political and personal discussions; for all the support throughout my four years at SE1; for many times proof reading this initially exhausting thesis and for many rides home.

Most and for all I thank Dr. Stefan Gall for supervising my work and for being a friend; for being honest and true all times; for being both severe and fun; for being supportive and giving me all these opportunities to present my results to the scientific community; for all I was able to learn on science and the scientific world; and of course for the cool time together in Japan.

I want to thank my colleagues and room mates Dr. Juliane Klein and Martin Muske for all the hilarious times, especially on Friday afternoons. I want to thank Juliane especially for all the on and off topic discussions. I want to thank Martin especially for being the best aluminum-induced layer exchange processer in the world.

I want to thank all students who directly contributed results to my work: Desmond Low for programming the heating stage controller; Michela DeVincentis for doing Hall measurements; Robert Heimburger for the heating step experiments; Andreas Schneider for the cooling step experiments.

I want to thank Dr. Björn Rau for doing all the work. No really, it seems to me that Björn did all the work on making and measuring solar cells, helping in report writing, proof reading of papers, revising posters and talks... I want to thank Björn for remaining calm, friendly and in a good mood during all this stress.

I want to thank Dr. Andrey Sarikov for theoretical discussions of the ALILE process.

I want to thank Kati Hübener for caring and the interesting discussions on the ALILE process.

I want to thank all members of the METEOR project for the interesting coopera-

tion. Special thank's go to Dr. Michael Stöger-Pollach for many TEM images and discussions on diffusion paths.

I want to thank Prof. Dr. Hari Reehal and Thomas Quinn for EBSD measurements and discussions.

I want to thank Ina Sieber for the SEM and EBSD measurements.

I want to thank Gisela Keiler, Kerstin Jacob and Sabrina Kreutzmann for tons of sample and substrate treatments.

I want to thank Dr. Eveline Rudigier for being the first proof reader of this thesis. I admire your calm tenacity on working your way through this horrible mess (I hope the figure captions are satisfactory, now).

I want to thank the staff of SE1 for the nice and friendly atmosphere at HMI in Adlershof. Special thanks to the other Ph.D. students at SE1 for regularly attending the 'Doktorandentreffen'. You know that without you, this would not have been possible.

Particularly, I want to thank my family and friends for supporting and encouraging me and also for reminding me, that there are more important things in life than work, science and solar power. I am a very lucky person knowing all of you.

**curriculum vitae:** Jens Schneider, born in Calw 09/06/1975

| | |
|---|---|
| since 09/02 | PhD student,<br>Technische Universität Berlin, Hahn-Meitner-Insitut Berlin,<br>'Aluminum-induced crystallization of amorphous silicon for seed layers in polycrystalline silicon thin film solar cells' |
| 09/02 | participant,<br>Dresdner Sommerschule Mikroelektronik |
| 01/02-08/02 | Diplom,<br>Technische Universität Berlin, Hahn-Meitner-Institut Berlin,<br>'Surface preparation of ALILE seed layers for polycrystalline silicon thin film solar cells' |
| 10/01-12/01 | student assistant,<br>Hahn-Meitner-Institut Berlin<br>'Preparation for setup of spectral response measurement' |
| 05/01-09/01 | internship,<br>Ferdinand-Braun-Institut für Höchstfrequenztechnik Berlin,<br>'Device stability measurements on hetero bipolar transistors' |
| 02/99-03/01 | student assistant,<br>Hahn-Meitner-Institut Berlin,<br>'Scanning probe microscopy induced structuring of silicon' |
| 10/98-08/02 | student electrical engineering,<br>Technische Universität Berlin |
| 10/97-12/97 | internship,<br>Ecosolar, Ratingen,<br>'Preparation and installation of photovoltaic home systems' |

| | |
|---|---|
| 10/95-09/98 | student electrical engineering, (Vordiplom)<br>Gerhard Mercator Universität Duisburg |
| 06/95 | Abitur,<br>Albertus-Magnus-Gymnasium Ettlingen |
| 08/92-06/93 | exchange student,<br>Meadowdale Highschool, Lynnwood, WA, USA |